RICE UNIVERSITY

Surface Functionalization of Graphene-based Materials

by

Akshay Mathkar

A THESIS SUBMITTED

IN PARTIAL FULFILLMENT OF THE

REQUIREMENTS FOR THE DEGREE

Doctor of Philosophy

APPROVED, THESIS COMMITTEE

Pulickel M. Ajayan, Chair
Benjamin M. and Mary Greenwood
Anderson Professor of Engineering

Enrique V. Barrera
Professor of Mechanical Engineering and
Materials Science

Angel Marti
Assistant Professor of Chemistry and
Bioengineering

HOUSTON, TEXAS

April 2013

ABSTRACT

Surface Functionalization of Graphene-based Materials

by

Akshay Mathkar

Graphene-based materials have generated tremendous interest in the past decade. Manipulating their characteristics using wet-chemistry methods holds distinctive value, as it provides a means towards scaling up, while not being limited by yield. The majority of this thesis focuses on the surface functionalization of graphene oxide (GO), which has drawn tremendous attention as a tunable precursor due to its readily chemically manipulable surface and richly functionalized basal plane. Firstly, a room-temperature based method is presented to reduce GO stepwise, with each organic moiety being removed sequentially. Characterization confirms the carbonyl group to be reduced first, while the tertiary alcohol is reduced last, as the optical gap decrease from 3.5 eV down to 1 eV. This provides greater control over GO, which is an inhomogeneous system, and is the first study to elucidate the order of removal of each functional group. In addition to organically manipulating GO, this thesis also reports a chemical methodology to inorganically functionalize GO and tune its wetting characteristics. A chemical method to covalently attach fluorine atoms in the form of tertiary alkyl fluorides is reported, and confirmed by MAS ^{13}C NMR, as two forms of fluorinated graphene oxide (FGO) with varying C/F and C/O ratios are synthesized. Introducing C-F bonds decreases the overall surface free energy, which drastically reduces GO's wetting behavior, especially in its highly fluorinated form. Ease of solution processing leads to

development of sprayable inks that are deposited on a range of porous and non-porous surfaces to impart amphiphobicity. This is the first report that tunes the wetting characteristics of GO. Lastly as a part of a collaboration with ConocoPhillips, another class of carbon nanomaterials - carbon nanotubes (CNTs), have been inorganically functionalized to repel 30 wt% MEA, a critical solvent in CO_2 recovery. In addition to improving the solution processability of CNTs, composite, homogeneous solutions are created with polysulfones and polyimides to fabricate CNT-polymer nanocomposites that display contact angles greater than 150^o with 30 wt% MEA. This yields materials that are inherently supersolvophobic, instead of simply surface treating polymeric films, while the low density of fluorinated CNTs makes them a better alternative to superhydrophobic polymer materials.

Acknowledgments

While it is my name that appears on the front page of this thesis, there are a number of people who have greatly contributed to getting it to where it is. I can confidently say that the last 5 years have been the best of my life, and the people I've interacted with, on both a professional and personal level, have had a tremendously positive impact on me.

I would like to express my sincere gratitude towards my advisor, Dr. P.M. Ajayan. Working under his guidance and being around his refreshing approach towards research has been eye-opening for me. From my very first days as a graduate student, he has been a great mentor and every day I look forward to emulating his actions as a leader. I am also grateful to the NSF-Eager Fund (Award# CMMI-1153648) and ConocoPhillips for their financial support.

I would also like to thank Dr. Robert Vajtai. The impromptu coffee breaks and conversations in his office have been greatly enriching, and will be dearly missed. I also appreciate Dr. Angel Marti and Dr. Enrique V. Barrera, who agreed to serve on my defense committee at such short notice, and provided me with due guidance. I would like to thank Dr. Lawrence Alemany for his expertise in dealing with fluorine-based ^{13}C-NMR as well as giving the work done in Chapter 3 a much clearer direction and focus. Every member of the Ajayan group at Rice University has been a contributor to this thesis in one form or another, and I am honored to acknowledge them. Amongst those, Dr. T.N. Narayanan, Dr. Kaushik Balakrishnan, Charudatta Galande, Neelam Singh, Sanketh Gowda, Hemtej Gullapalli and Daniel

Paul Hashim have been peers that I have approached in moments of confusion, and at times desperation! My experience with ConocoPhillips was another turning point during my Ph. D., and the time spent specifically with Dr. Clint Aichele and Dr. Imona Omole gave me a look at research in industry, which is something that not a lot of graduate students have the opportunity to do, and for that, I am thankful. I would also like to thank Carl Deppisch at Intel Corporation, who I worked with during the summer of 2012.

Over the past 5 years, I have also been an active member of Rice Club Tennis, which has been a fantastic way to remain in touch with my one of my long-standing hobbies and also provided a continuous influx of talented and hard-working undergraduate interns. Dylan Tozier, Patricia Chang and Patrick Nguyen were instrumental in each of the three first-author papers I published, and for the long weekends and late weeknights, I am extremely grateful. It wouldn't be fair for me to not mention Dr. Raul Caretta, at the University of Minnesota, who has been a great mentor, and teachers from Gandhi Memorial International School in Jakarta, Indonesia who have stressed on the value of continuing to pursue learning in me from the get go.

Lastly, it would be safe to say that I would not have gotten through this degree without the support of my family members. My parents, Uday and Savita Mathkar and my sister Ankita, have both been a great source of emotional stability, always reminding me that life is more about going through the journey, rather than getting to the final destination.

Contents

List of Figures

List of Tables

List of Equations

Nomenclature

GO	Graphene Oxide
CNT	Carbon Nanotube
SWNT	Single-Walled Carbon Nanotube
MWNT	Multi-Walled Carbon Nanotube
FGO	Fluorinated Graphene Oxide
HFGO	Highly Fluorinated Graphene Oxide
PSF	Polysulfone
RGO	Reduced Graphene Oxide
CCG	Chemically Converted Graphene
CARGO	Chemically Active RGO
FTIR	Fourier-Transform Infrared Spectroscopy
ATR	Attenuated Total Reflectance
SEM	Scanning Electron Microscope
TGA	Thermogravimetric Analysis
MAS	Magic Angle Spinning
NMR	Nuclear Magnetic Resonance

Chapter 1

Introduction

1.1. Introduction to Carbon Materials

The study of carbon can be dated back to 3750 BC, the first reported use of it being to reduce copper and zinc ores. While it was not until the late 18th century that carbon was actually identified as an element by the famous French chemist Antoine Lavoisier[1], scientific progress with respect to carbon has been consistently recorded from all over the world, such as using charcoal for medicinal purposes, as retrieved from Egyptian papyri in about 1500 BC. Hippocrates and Pliny also used charcoal to 'treat' diseases such as epilepsy and anthrax during 400BC. Around the same time, the first records of charcoal as water filters are obtained from both Phoenician and Hindu cultures. Records of further advances have been abruptly stopped, when Roman Emperor Diocletian called for destruction of scientific books in 297 AD[2].

The recognition of the allotropes of carbon also follows a similar timeline, with diamond being the first to be discovered approximately 3000 years ago in India. While graphite was also 'discovered' around 4000BC, it was then known as 'blacklead' and used for pottery decorations particularly during Neolithic times. It wasn't until 1789 that German geologist Abraham Gottlob Werner actually named it graphite, also meaning 'writing stone'. The third allotrope to be synthesized was Buckminsterfullerene, in 1985 by Kroto and coworkers at Rice University[3],[4]. This important discovery turned the attention of researchers towards chemically fabricating individual sheets of graphitic carbon and eventually led to the discovery of finite, carbonaceous tubular structures [5] in 1991 by Iijima *et al.*, also known as carbon nanotubes (CNTs). A revolution in the field of nanotechnology was initiated, which lived up to the initial hype when few-layer 'graphene' was isolated in 2004 using numerous experimental techniques[3],[4] by Geim and Novoselov, and reached its apex with graphene winning the Nobel Prize for Physics in 2010.

Ever since the unexpected discovery of free-standing graphene films in 2004, a vast number of studies have followed up with experimental and theoretical evidence of exceptional optical[6], chemical and electronic properties[7]. Structurally, graphene can be thought of as a basic building block for other derivative nanomaterials: it can be rolled into carbon nanotubes (CNTs), stacked into graphite, or wrapped into fullerenes (Figure 1.1). High-quality graphene is obtained by either chemical vapor deposition (CVD) techniques[8] or micromechanical exfoliation of graphite [7], but both techniques are limited by the quantity of graphene synthesized. Thus, its insulating, heterogeneous, counterpart,

graphene oxide (GO)[9][10], has gained prominence in recent times as a *chemical* means to obtain larger quantities (i.e. tons) of graphene by conventional reduction chemistry. As the attention turned to focusing on the chemistry of GO, a number of reports followed that explored the properties of GO itself [11]–[14], which has led to additional research being conducted on this material, a major part of which involves both its organic and inorganic functionalization.

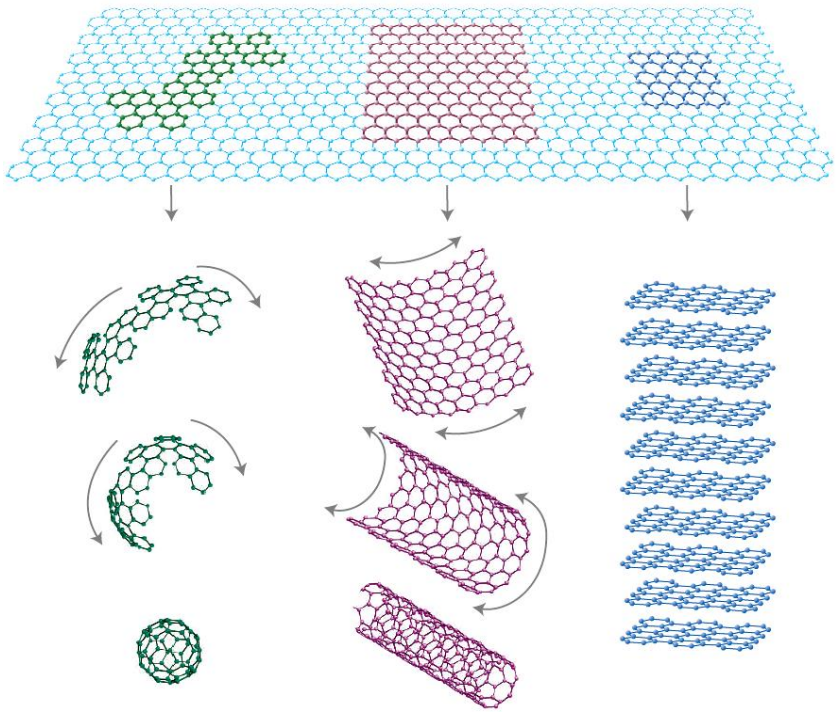

Figure 1.1 –An overview of graphene-based nanomaterials. Graphene can be wrapped into OD fullerenes (leftmost, green), rolled up into 1D nanotubes(middle, purple) or stacked into 3D graphite (far right, dark blue)[7].

This chapter serves as an introduction to graphene oxide (GO). It starts with the history of GO, particularly in the form of various synthetic schemes that have been proposed over the past 150 years since its discovery. Consequently, with the

advent of breakthrough characterization techniques, and progress in research amongst the community, the structure of GO has also evolved, specifics of which are discussed. A convenient way to look at the history of graphene-based materials is presented in Figure 1.2, from the first preparation of GO in 1840, to 2004, where graphene gained major prominence. Techniques to chemically reduce GO and 'synthesize' graphene have then been presented, with a comparison of chemically converted graphene (CCG) from different schemes to CVD graphene, and how these differ, not only in terms of electronic properties, but also structural integrity and surface morphology. The significance of surface functionalization in terms of organic manipulation of the C/O ratio, and inorganic, covalent functionalization is then discussed in detail. The effect of nanoscale manipulations to the richly functionalized organic basal plane of GO is evident in its macroscopic properties. Lastly, the objective of this thesis and its scope is discussed.

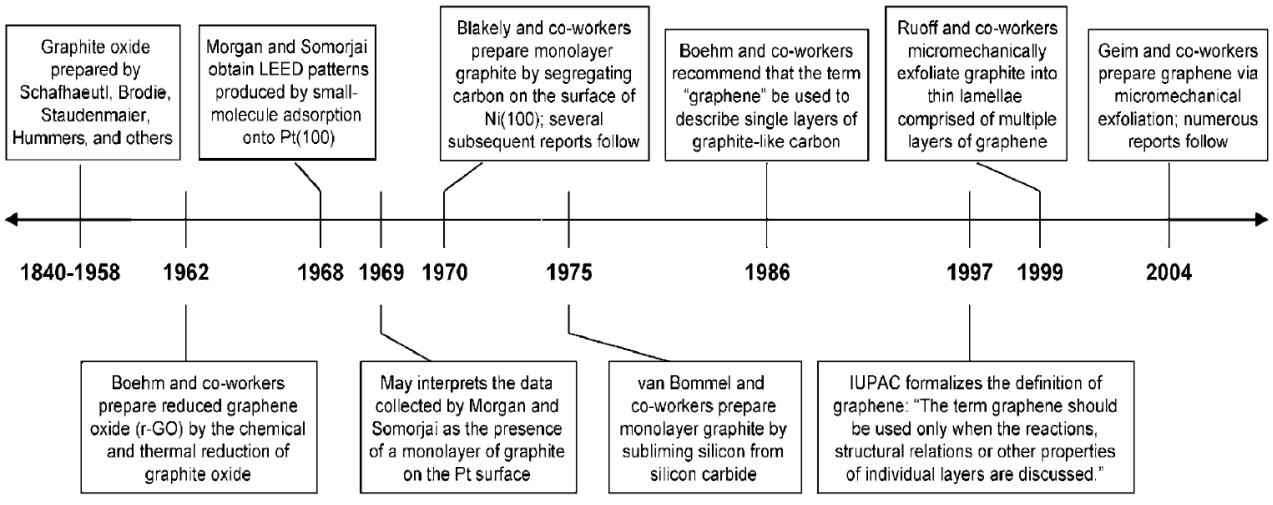

Figure 1.2- A brief history of graphene-based materials[15].

1.2. A Brief Introduction to Graphene Oxide

By definition, GO can be described as an atomically thin sheet of graphite with various organic functional groups covalently bonded to its basal plane and edges[13][16]. These include epoxy (C-O-C) and hydroxyl (C-OH) moieties bonded to the basal plane and carbonyl (C=O), carboxylic acid (COOH) and lactol groups on the edges[9], [16]. The presence of these functionalities in random abundance[1] makes GO a chemically complex, inhomogeneous system consisting of a hybrid sp^2/sp^3 domain. This defective structure greatly reduces the number of conductive pathways for electron transport, giving GO its well-known insulating characteristics as is confirmed by reported electrical conductivity values of 0.4 S m^{-1} and an optical band gap of 3.5 eV[9], [13], [16]. In stark contrast, its conductive counterpart graphene consists of a well-defined network of sp^2 carbon atoms arranged in a 2D lattice. When compared to graphite, the interlayer spacing of GO is more than twice due to organic functional groups covalently bonded to its basal plane. While graphite shows an interlayer spacing of 0.336 nm, XRD analysis has reported values of 0.88 nm for GO[9]. In polar solvents, however, these organic functional groups are responsible for a stabilizing electrostatic repulsion effect that yields stable, hydrophilic colloidal solutions (Figure 1.3). Unlike graphene, which is 'grown' using CVD at high temperatures, GO is chemically synthesized by reacting graphite with

[1] The relative abundance of functional groups depends on the method of synthesis and the reaction conditions .

harsh oxidizing agents [9], [13] (i.e. potassium chlorate, potassium permanganate, hydrogen peroxide etc.) at relatively mild temperatures and was first discovered over 150 years ago. In recent times, the focus has heavily shifted towards identifying a chemical reduction scheme to efficiently reduce GO to graphene, while minimizing defects in its surface morphology[17]. Proposed reaction schemes that have demonstrated success include reaction with $NaBH_4$, hydrazine hydrate and thermal annealing[18], [19]. Each method is however, accompanied by a set of disadvantages in the form of either compromised structural integrity or remnant isolated regions of un-reduced oxygen. The resulting disparities in the macroscopic properties are vast, and have been discussed in detail in sections that follow.

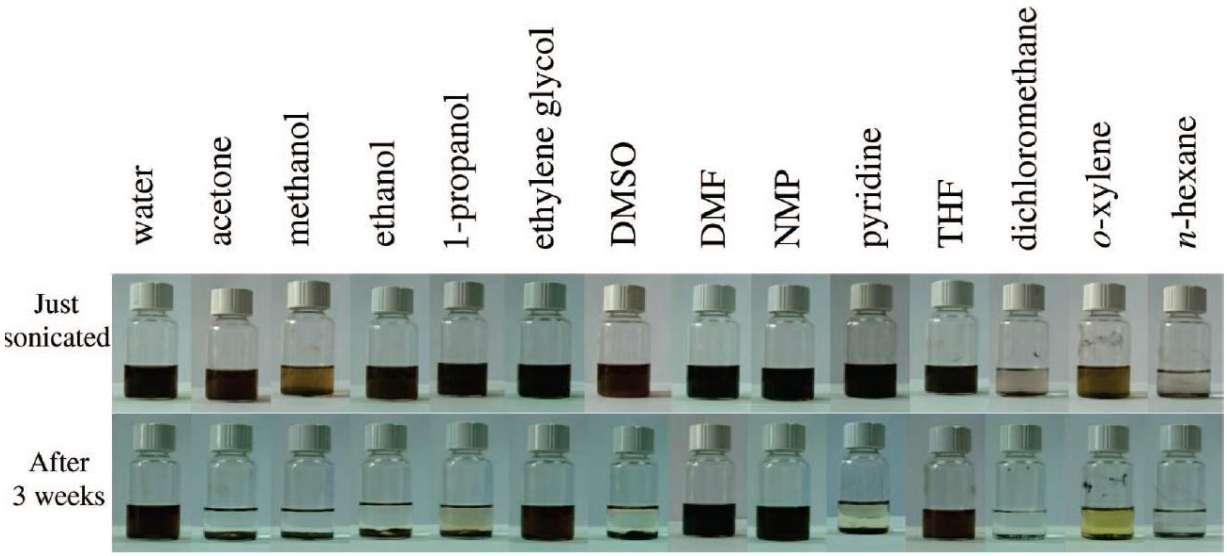

Figure 1.3- Stability of GO in various solvents. Typical solvents of choice are NMP, DMF, THF and DI water. The yellow color of *o*-xylene is due to the solvent, and not GO itself [20]

1.3. Proposed Synthetic Schemes

1.3.1. **First Studies on Graphite & the Brodie Method**

While graphite has prehistoric origins, with its first uses being reported in as early as the 4th century, relevant advances in its oxidation chemistry weren't made till *much* later, in the 19th century. The first person to investigate the exfoliation of graphite in solution was a German scientist by the name of C. Schafhaeutl[21] who described an experiment in which he attempted to decompose pieces of kish[2] by combining it with a mixture of nitric and sulfuric acid and boiling off the acid. What he observed was a 'swollen' form of graphite with a spongy texture and a much darker color, similar to that of coal. These fascinating observations, made a little over 175 years ago, are the first reports of graphite exfoliation. C. Schafhaeutl also mentioned the graphite turning a shiny blue color during reaction with HNO_3 and H_2SO_4. Interestingly enough, the very same observation is reported by British physiologist Sir Benjamin Brodie in 1859 in his paper entitled "On the atomic weight of graphite", wherein he first synthesizes a compound which he names 'graphitic acid'[6]. Structural characteristics of this "blue graphite" were finally explained using XRD in 1934 by Frenzel and coworkers, attributing it to sulfuric acid intercalation between the graphite lattice[15].

[2] The material is mentioned as 'kish by the iron-smelters, that had been separated from iron bulk' in a follow up report by H-P Boehm

Looking back at Brodie's findings, however, a number of interesting observations have been recorded. To study the oxidation of graphite, Brodie proposed reacting graphite with three times as much potassium chlorate ($KClO_3$; chlorate of 'potash') in HNO_3 for 72-96 hours at 60°C, till yellow vapors were evolved from the mixture. This process was then repeated 3-4 times to ensure complete oxidation after which the product was dried in vacuo and then at 100°C. Three macroscopic observations made in this report are quite intriguing. The first is concerned with the "unevenness" of the graphitic structures as Brodie concludes them to be too thin to be measured. The second observation goes on to add that the crystals are "extremely thin" in the direction perpendicular to the ground, due to which no reflection can be obtained to measure the thickness. Lastly, Brodie observes these crystals to decompose into a black residue upon ignition[22]. In other words, what Brodie has synthesized in this case, are actually nanoflakes of oxidized graphene, which are being chemically reduced upon heating to reduced graphene oxide (RGO). Brodie reported an empirical formula of $C_{11}H_4O_5$, but more importantly, the significance of the deductions made in this study fueled a race towards optimizing a synthetic scheme for GO.

1.3.2. **Origins of the Hummer's Method**

Approximately 40 years after Brodie's paper, Staudenmaier optimized Brodie's method by adding chlorate in multiple aliquots as a safer alternative to adding it in a single step[23]. He also increased the acidity of solution by increasing the volume of sulfuric acid. While this method was a slight improvement from Brodie's procedure,

it wasn't until 1957 when Hummer's Jr. published a paper[24] in the *Journal of American Chemical Society* entitled "Preparation of graphitic oxide", that the next significant threshold in GO synthesis was crossed . The motivation behind the study was to eliminate the hazards associated with potassium chlorate, and reduce the time required for oxidation. Up to that point, synthesis of graphite oxide resulted in the evolution of chlorine dioxide which is harmful. The method proposed by Hummers treated graphite with H_2SO_4, $NaNO_3$ and $KMnO_4$ for a little under 2 hours below 45°C. The active species in the reaction, however, is *not* the permanganate, but rather, manganese heptoxide, as shown in the scheme below[25]:

$$KMnO_4 + 3H_2SO_4 \longrightarrow K^+ + MnO_3^+ + H_3O^+ + 3HSO_4^-$$

Equation 1.1 – Ionic dissociation of potassium permanganate ($KMnO_4$) upon reaction with sulfuric acid

The reactive, bimetallic heptoxide then forms as follows:

$$MnO_3^+ + MnO_4^- \longrightarrow Mn_2O_7$$

Equation 1.2 – The formation of the highly reactive bimetallic heptoxide in the presence of a strong acid[25]

In addition to being a safer alternative to existing methods at the time, the slightly sophisticated procedure of the Hummer's method also had reactionary benefits. The bimetallic heptoxide is far more reactive than its monometallic tetraoxide counterpart and is shown to selectively oxidize aliphatic over aromatic double bonds. The procedure was slightly improved by Kovtyukhova and

coworkers[26] in 1999, where they proposed a step to pre-treat graphite with H_2SO_4 $K_2S_2O_8$ and P_2O_5 at 80^0C to increase the extent of oxidation. This "modified" version of the Hummer's method is used to this day.

1.3.3. **An Improved Method to synthesize GO**

In recent times, Marcano *et al.* reported a less toxic method[27] with a greater efficiency of oxidation, aptly calling it the 'Improved Method' to synthesize GO. The procedure excludes $NaNO_3$, increases the quantity of $KMnO_4$ and conducts the reaction in a 9:1 mixture of H_2SO_4/H_3PO_4. Advantages of the improved method over the Hummer's method are that the temperature in the former can be controlled a lot easier, since it does not involve a large exotherm. Secondly, no toxic gases are released during the process, and lastly, a greater amount of oxidized, hydrophilic carbon is recovered in the improved method (shown at the bottom of Figure 1.4). Kosnykin and coworkers reported a method to unzip GO nanoribbons (GONRs) from MWNTs, in which they use H_3PO_4 to keep the aromatic domain in place[28]. The same logic was applied by Marcano *et al.* in their synthetic procedure, which for the first time, introduces H_3PO_4 into the oxidation reaction.

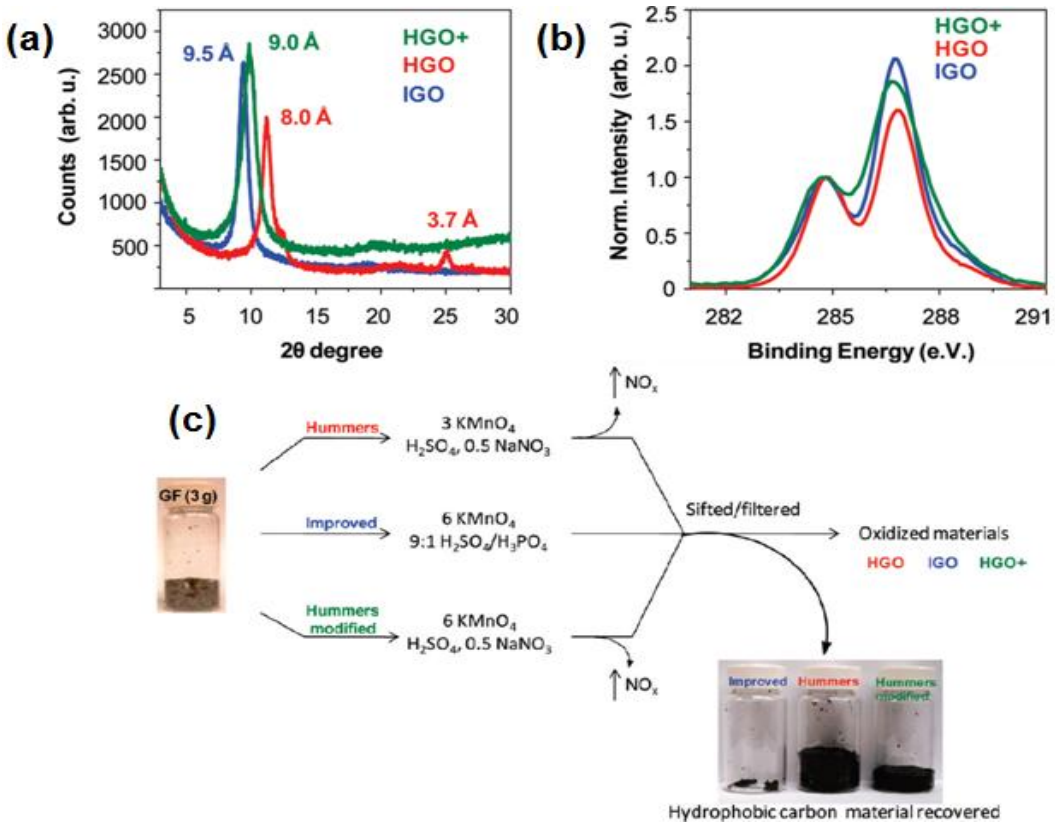

Figure 1.4 – A comparative figure of GO synthesized by the Improved Method (IGO), Hummer's Method (HGO) and Hummer's Method with excess $KMnO_4$ (HGO+) [27].

Figure 1.4 (c) presents the chemical routes of two variations of the Hummer's method in comparison to the improved method. At the bottom right, there is a drastic difference in the amount of hydrophobic carbon material that is recovered at the end of the three experiments, indicating a much higher efficiency of oxidation. While the actual paper by Marcano *et al.* extensively characterizes all three products, the UV-Vis spectra and XRD peaks are two examples of differences in the quality of the three GOs. Figure 1.4 (a) shows the interlayer spacing of each sample, which in turn is directly proportional to the extent of oxidation of the graphitic plane. These spacings are 9.5 Å (IGO), 9 Å (HGO+) and 8 Å (HGO). Secondly, the peak

at 3.7 Å seen in the HGO spectrum represents unoxidized graphite in the sample and is not detected in the IGO spectrum. The UV-Vis absorption spectra shown in Figure 1.4 (b) point out differences in the degree of *conjugation* within the three GO samples. While the λ_{max} is almost identical for all 3 samples, the extinction coefficients of the three, especially that of IGO, is much greater, indicating that qualitatively IGO should have a greater number of aromatic rings for a given samples size compared to HGO+ and HGO. A detailed look at the absorbance behavior of chemically dissimilar GO is presented in Chapter 2. The improved method almost 'fine-tunes' previous methods that report GO synthesis. This is absolutely imperative, as it greatly affects one's understanding of GO's structure, which is inter-connected with the ability to perform surface functionalization reactions. This becomes evident over the course of the chapter.

1.4. Proposed Structures of GO

Similar to synthetic methods, the structure of GO has also greatly evolved over time. The complexity associated with preferential oxidation of aromatic domains, and the defects that accompany it is what makes predicting the oxidation mechanism of GO a challenging problem. In addition to this, the sample-to-sample variability and its highly amorphous structure are what make predicting a structural formula for GO a difficult question to answer. With the advent of novel characterization techniques, however, researchers are getting closer.

1.4.1. **Initial Models**

The first structure of GO was proposed by Hoffman & Holst (1939), shown in Figure 1.5. In this, it was assumed that only epoxy groups were covalently bonded to carbons on a homogeneous, sp^2 graphitic basal plane, and the molecular formula was determined to be C_2O. In 1946, Ruess devised the first model to present GO as a hybrid sp^2/sp^3 network, rather than just a sp^2 network similar to graphite (shown in Figure 1.5). He also accounted for the hydrogens by suggesting that hydroxyl groups were covalently bonded to the graphitic plane in addition to epoxides. A glaring misconception in the Reuss model was that it assumed a lattice structure with a definitive repeat unit[3] which led to numerous other structures (i.e. Scholz-Boehm,

[3] $1/4^{th}$ of the cyclohexanes were bonded to –OH at C4 and contained epoxides in C1 and C3.

Nakajima-Matsuo) to build on this idea, albeit with slight variations in the chemical composition. None of these structures, however, focused on the inhomogeneity of GO. The Lerf-Klinowski model, proposed in 1998 (Figure 1.5), was the first to do so.

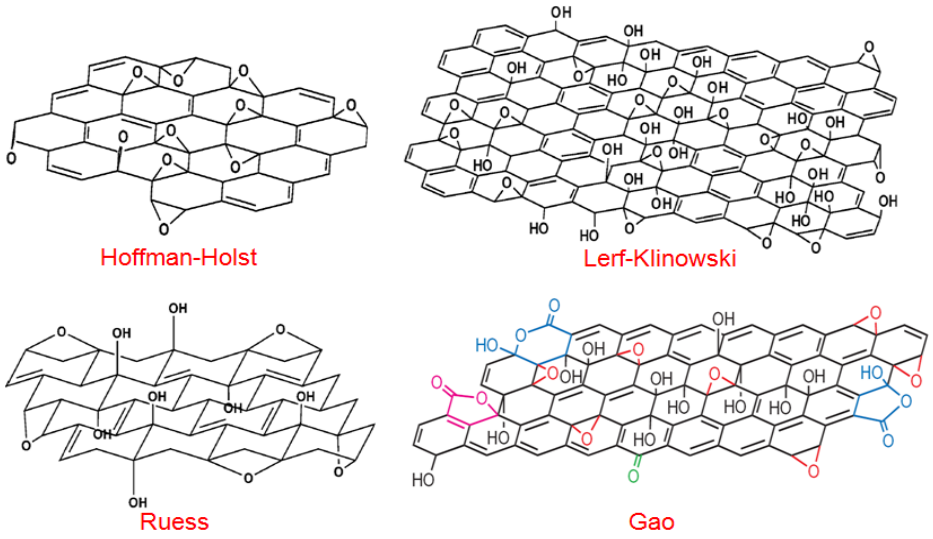

Figure 1.5 – The structural evolution of GO over the years [13].

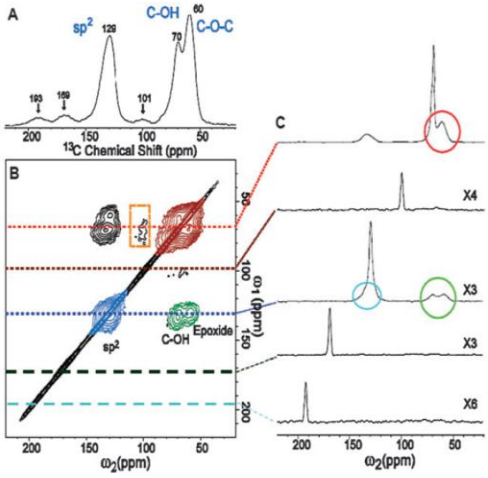

Figure 1.6 – 1D ^{13}C MAS (A) and (B) 2D $^{13}C/^{13}C$ solid-state NMR spectra of ^{13}C-labelled GO, while slices from the 2D spectrum are magnified in (C). Each functionality is color-coded, while circles in (C) represent cross-peaks between *sp²* and the particular functional group represented by the color[29].

1.4.2. **Lerf-Klinowski Model & Recent Advances**

The Lerf-Klinowski model was also the first to utilize 1D & 2D ^{13}C MAS Solid-state (SS) NMR to reveal structural insights into GO. Figure 1.6 (A) shows 3 broad resonances: the first, at 60 ppm, is attributed to 1,2 ethers (epoxy) while tertiary alcohols are responsible for the peak at 70 ppm. Lastly, the ~130 ppm peak was attributed to a mixture of alkenes on the graphitic plane[30]. GO has always formed stable, colloidal particles in deionized water, and Lerf-Klinowski attribute this to the interlayer hydrogen bonding between the epoxide and hydroxyl moieties. Quantitatively, this can be explained by examining the full-width-at-half-maximum height of the water peak, which remains almost constant from 123 – 473 K, indicating favorable interactions between GO and water in the form of H bonding. The presence of an aromatic domain instead of isolated double bonds was justified by the harsh oxidation reaction conditions of the Hummer's method. The strong reaction kinetics associated with this mode of reaction would break down isolated double bonds, and only an aromatic graphitic domain would be strong enough to withstand it and display peaks in the NMR spectra. Lastly, by combining IR spectra with ^{13}C NMR deductions, this approach determined carboxylic acid groups to be present on the edges of GO. The resulting model has been shown in Figure 1.5. In 2009, Gao and coworkers published another paper[9] with slight modifications to the structure of GO: using a number of SS ^{13}C NMR experiments, their paper reports the presence of a signal near 100 pm, which is attributed to 5- and 6-membererred-ring lactols along the edges of GO. This structure of GO is widely accepted today, although a few reports have been contradictory[31], [32].

1.5. Reduction of GO

The origin of GO's popularity, at least initially, was as a synthetic means towards graphene. The underlying principle behind this approach was that while high quality graphene (i.e. with a defined sp^2 domain) had remarkable electronic and optical properties, its yield was greatly limited by CVD growth. Realizing a chemical means towards large scale sheets of graphene would provide a tremendous boost towards making graphene more accessible to be implemented in the applications that it was being tested for on the bench-scale, and was thus the motivation for researchers developing the following strategies for reducing GO[14]. The popular ones have been described in this section.

1.5.1. **Chemical Reduction of GO**

Two strategies to chemically reduce GO are reported here. The first was reported by Stankovich *et al.* in 2007[33], wherein individual GO sheets are exfoliated in solution, followed by their *in-situ* reduction using hydrazine to generate individual graphene sheets. The reported procedure utilizes bath sonication to exfoliate GO sheets in deionized water (DI water) followed by addition of hydrazine hydrate (1 mL, 32.1 mmol) at 100^{o}C for 24 hours. Visually, GO, which is a yellowish-brown powder that forms a stable colloidal dispersion in solution, precipitates out upon reduction and changes its color to a fluffy, black powder which can simply be filtered out and appropriately washed. This is presumably due to the reduction of oxygen on the surface of GO, which reduces its overall hydrophilicity. The authors also note the black color to be an indicator of restoration of the

graphitic domain. As reduction progresses, the solvation of individual reduced graphene oxide (RGO) sheets *decreases,* leading to them aggregating in solution.

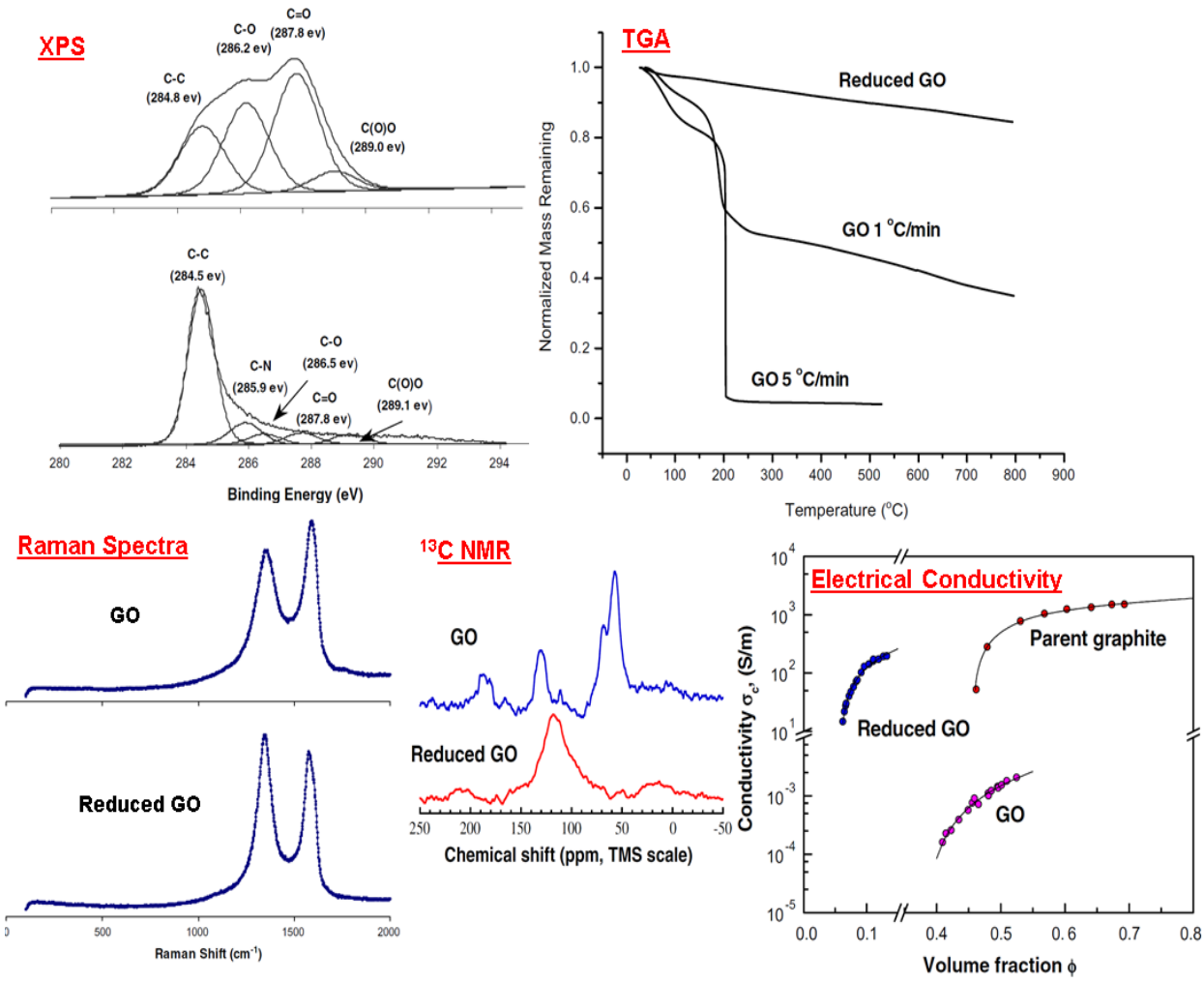

Figure 1.7 - Characterization of graphene oxide before and after reduction by hydrazine hydrate [33].

A significant increase in the C/O ratio was recorded in RGO, while the relative amount of intercalated water decreased from 25 wt% down to 2.8 wt%. The deconvoluted XPS spectra of both GO and RGO in Fig. 1.7 provide specific details about the degree of oxidation. Initially, GO is well-oxidized, showing carboxyl (C-O),

carbonyl (C=O) and carboxylate (O-C=O) peaks in addition to the customary C-C peak. Upon reduction, most of the oxygen-bearing peaks are completely reduced, with minimal remaining oxygen (likely contributing to the presence of 2.8 wt% intercalated water). Interestingly, the authors report the presence of a C-N peak (285.9) eV, which they hypothesize due to the reaction of hydrazine with the carbonyl group. In recent times this observation has kick-started a number of other studies that focused on GO functionalization and doping, some of which are presented in Section 1.3. MAS ^{13}C NMR spectra show typical peaks at ~60 ppm and 70 ppm (epoxide and tertiary alcohols) while the signal at 130 ppm is due to the sp^2 graphitic domain. Upon reduction, the oxygen-bearing peaks are barely detected, indicating almost complete removal of specific functionalities. The authors also report a peak at 117 ppm, which they attribute to varying C atom environments.

Raman spectra presented by Stankovich *et al.* (Figure 1.7) gives insight into structural alterations. Characteristically, natural flake graphite only shows a G peak at 1581 cm^{-1}. The authors report this peak to broaden and shift to 1594 cm^{-1} after oxidation, as well as the rise of a sharp D peak at ~1360 cm^{-1} which is an indicator of a reduction in the size of the sp^2 domain, indicating deterioration in surface conjugation. RGO shows D and G bands in almost the same positions, but the D/G intensity is much greater than that of GO indicating a further decrease in the size of the sp^2 domains upon reduction due to the creation of new graphitic domains, albeit smaller in size, but greater in number to the ones that were present in GO after oxidation. Thermogravimetric analysis (TGA) provides a measure of the thermal stability of GO and RGO. GO has been reported to experience pyrolysis at higher

temperatures, making it a thermally 'unstable' material, which is seen in a majority of mass loss being recorded after 200^{o}C. RGO, on the other hand, remains largely stable showing no drastic decrease in mass with temperature. The faster rate (5^{o}/min) illustrates this much more vividly in the case of GO (Figure 1.7).

Lastly, the authors compare the electrical conductivity of the parent graphite with GO and RGO to serve as an indicator of the extent of reduction. With graphene having tremendous potential in electronics, especially as a flexible electrode material in solar cells, having RGO with the electrical conductivity on the same order of magnitude as graphene is a significant target. *Celzard* and coworkers[34] describe a method to measure conductivity of carbonaceous powders, which involves compressing a precisely weighed amount of powder in a tube at a choice of various loads, followed by a two probe method to measure the dc electrical resistance. With the current through the sample being a constant, the voltage drop can be measured. Stankovich *et al.* use the following equation to measure the electrical conductivity[33],[35],[36]:

$$\sigma_c = \sigma_h \left[\frac{\varphi - \varphi_c}{1 - \varphi_c}\right]^k$$

Equation 1.3 – Equation derived from general effective media (GEM) equation for measuring the conductivity of CCG

The above equation has been derived from the general effective media (GEM) equation, with σ_c being the conductivity of the composite medium, σ_h is the conductivity of the highly conductive phase while φ is its volume fraction. Φ_c is the

percolation threshold and k is an exponent directly dependant on the particle shape and φ_c. The comparative graph in Figure 1.7 is a reflection of the degree of restoration of electrical properties upon reduction, with flake graphite being a benchmark. The conductivity of RGO is measured at approximately 10^2 S/m, which only an order of magnitude lesser than graphite, and 5 orders of magnitude greater than GO.

Thus, the advantages of using hydrazine hydrate are evident, from the results presented above. However, the method is accompanied by a handful number of limitations, which is why it is not the first choice for reducing GO. Firstly, hydrazine hydrate is an extremely toxic reagent that requires handling with care. Secondly, the increase in the C/N ratio, which is noted by Stankovich *et al*[33]., but not explored further, is in fact detrimental to the overall structure of RGO. Park *et al.* recently published a paper[19] investigating this very behavior of hydrazine-based reduction of GO and found nitrogen to be present in the form of pyrazole groups at the edges of these "chemically modified graphenes (CMGs)". Thus rather than being a reduction method towards graphene, hydrazine treatment was in fact more of a substitution/doping method through which nitrogen was being incorporated into the graphene lattice. While this has its advantages on its own (Section 1.6), it defeats the purpose of formulating a strategy towards obtaining pure graphene.

The challenge, then, is to devise a method that (i) doesn't lead to substitution/functionalization of the graphene basal plane and (ii) does not involve toxic reagents, while still reducing GO completely to graphene. Gao and coworkers

proposed a scheme[9] involving reaction with sodium borohydride ($NaBH_4$) followed by a wash in sulfuric acid (H_2SO_4) and thermal annealing. This "two- step" reduction scheme relies on $NaBH_4$ for deoxygenation of the graphitic plane, followed by dehydration using the sulfuric acid wash. Figure 1.8 shows a majority of reduction occurring after $NaBH_4$ treatment in the first step (CCG1 stands for chemically converted graphene after the first reaction), with only lactols remaining on the edges and minimal oxygen on the basal plane in the form of hydroxyl groups.

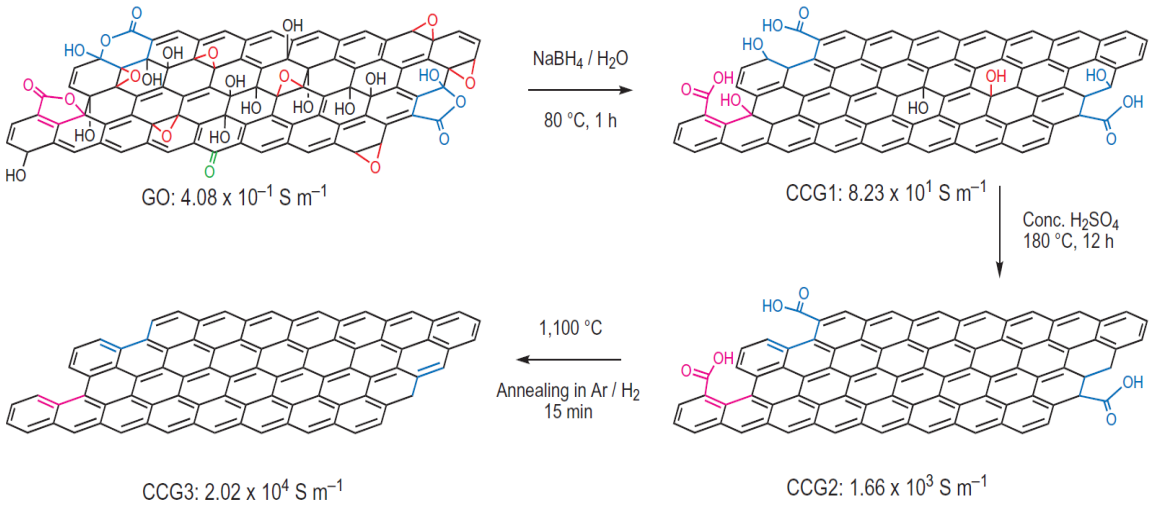

Figure 1.8 – Progression in reduction according to the $NaBH_4$ scheme, proposed by Gao *et al*[9].

Comparing the cross polarization (CP) and direct ^{13}C pulse spectra of the reduced products justifies this (Figure 1.9); CCG1 shows complete reduction of the epoxide signal (~60 ppm) and a considerable decrease in the alcohol signal (~70 ppm). Ketones (~190 ppm) and esters (~167 ppm) are also absent from both spectra. After acid treatment (i.e. dehydration), the alcohol signal is seen to completely disappear from the spectrum. The authors hypothesize this dehydration

reaction to lead to the restoration of the sp^2 network in the form of alkenes. Carboxylic acids, which remain on the structure of CCG2, are known to resist reduction by $NaBH_4$, and their signal persists even after the sulfuric acid wash. The last step, which involves annealing at 1100°C, is hypothesized to restore the π conjugation on the edges.

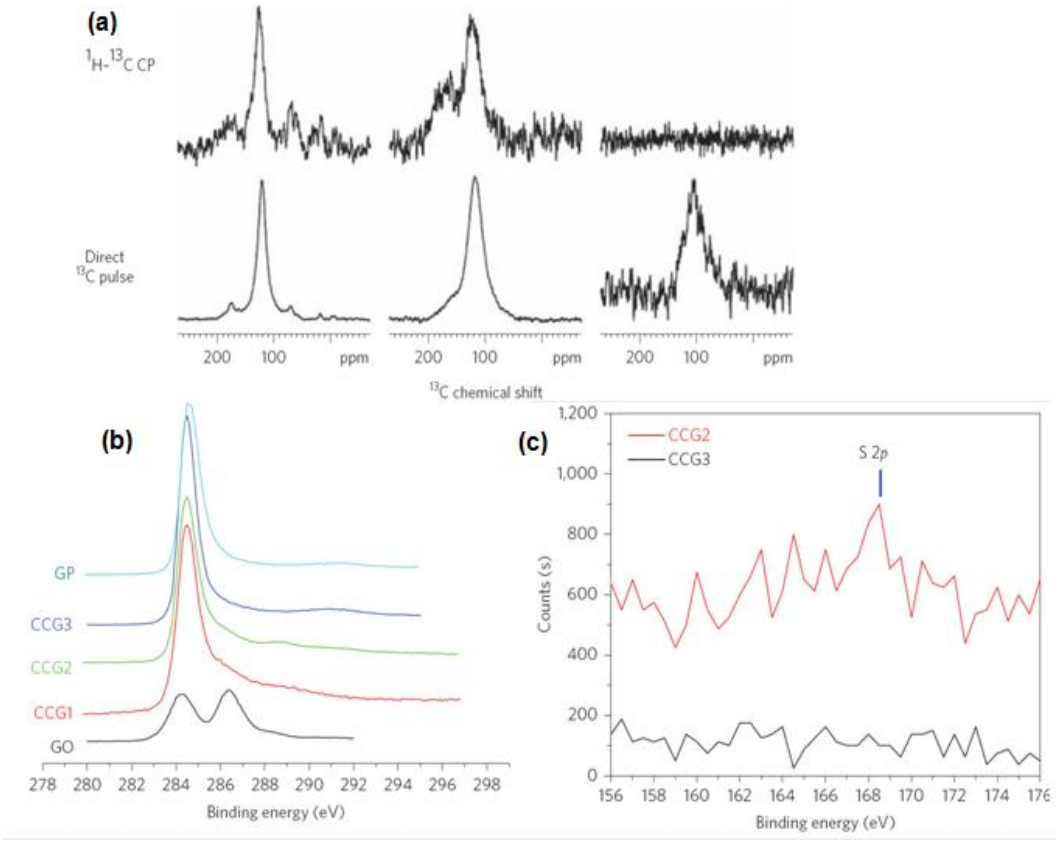

Figure 1.9 – Characterization of chemically converted graphenes (CCGs) in comparison to starting graphite powder (GP) and GO to show the extent of reduction.

To measure the electrical conductivity of GO and subsequently reduced RGO, Gao *et al.* implement a four-probe method[9]. GO shows a conductivity of around 0.5 S/m which increases only a little over 2 orders of magnitude in CCG1 (~ 8 X 10^1

S/m). However after the dehydration and annealing step, CCG3 shows a conductivity of 2 X 10^4 S m^{-1} which is 5 orders of magnitude higher than GO, and is a good indicator of the restoration of the π conjugated system. XPS results complement ^{13}C NMR spectra; the two distinct peaks which are initially seen in the GO spectrum corresponding to a high degree of oxidation (as deconvoluted in the work by Stankovich *et al.*) are not present in the CCG1 spectrum, again confirming deoxygenation. Instead, the authors report the presence of a single peak at 291 eV indicating almost complete restoration of the aromatic domain by the time CCG3 is formed. Unlike the hydrazine hydrate method, there is no doping or functionalization due to reaction with the reducing agent. Elemental analysis of the final product confirms this, as there is negligible sulfur and nitrogen (<0.5 wt% each), making it a superior alternative over the former.

1.5.2. **Thermal Reduction of GO**

Thermal exfoliation of graphite oxide is one of the alternatives to chemical reduction of GO. A number of works have been published on synthesizing functionalized graphene by thermal treatment of graphite and/or graphite oxide at elevated temperatures. Schniepp[37] and coworkers report a procedure where graphite is heavily oxidized similar to the Staudenmaeir method. Oxidation is confirmed by an increase in the interlayer spacing via XRD (from 0.34 nm to 0.65-0.75 nm) as well as other characterization techniques. After being dehydrated, the graphite oxide is heated rapidly (>2000^{o}C/min) to 1050^{o}C in argon atmosphere, due to which graphite oxide splits into individual sheets and CO_2 is evolved. Upon

characterization, the authors observe a 500-1000-fold volume expansion of GO, no diffraction peaks, and extremely high BET surface area (750-1500 m^2/g), all of which are indicators of successful exfoliation.

Understandably, one of the disadvantages of heating graphite oxide to such high temperatures at accelerated rates is the formation of vacancies and topological defects. This directly affects the electronic properties of the functionalized graphene sheets (FGSs) as the presence of these "scattering sites" decreases the ballistic transport path length[16]. Raman spectra give a qualitative insight into the degree of disorder, and a comparative figure is shown below:

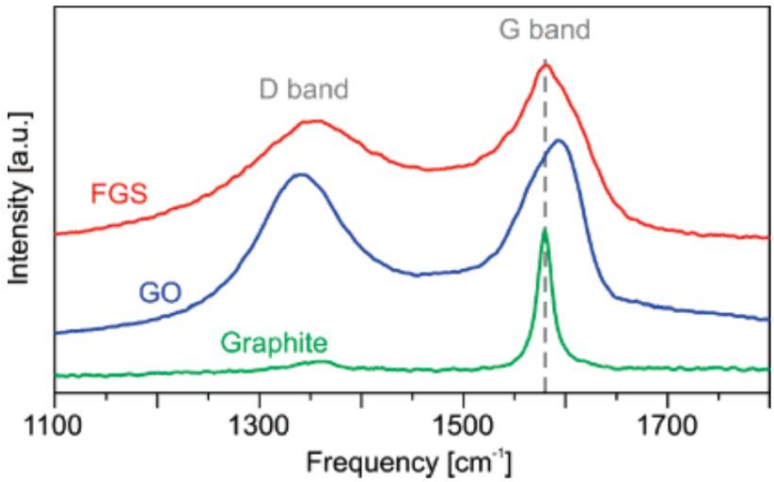

Figure 1.10 – Raman spectra upon oxidation and exfoliation of graphite, graphite oxide and FGS obtained at an excitation wavelength of 514.5 nm [38].

Highly ordered graphite shows only two bands: a sharp peak at 1575 cm^{-1} due to in-phase vibrations of the graphite lattice and a weak hump at ~1355 cm^{-1} indicating a low degree of disorder. It is understood that a greater disorder in the graphitic plane leads to a (i) broader G band and (ii) a broader D band with a higher

relative intensity than the G band. This broadening of both bands is seen as one compares the graphite spectrum to GO and FGS. Interestingly, Kudin *et al.* report the formation of additional defects and vacancies as GO is transformed to FGS, which include the 5-8-5 and the 5-7-7-5 defect[4] (i.e. Stone-Wales defects)[38]. This reduces the overall impact of the reduction scheme, as the structural integrity of the FGSs is clearly compromised. Figure 1.11 color-codes typical defects that are found on a single-layer RGO membrane. Contaminated regions are represented by grey, while disordered single-layer carbon networks are shown in blue. The patches of red are individual adatoms, or substitutions and isolate topological defects are represented in green. Lastly, the holes are in yellow. The atomic model presented by Bagri *et al.* is after thermal annealing at 1500K and remnant oxygen and carbon groups have been characterized by molecular dynamics simulations (Figure 1.11, c-k).

[4] This is a stable, double vacancy, consisting of two pentagonal rings (5) around an octagonal ring

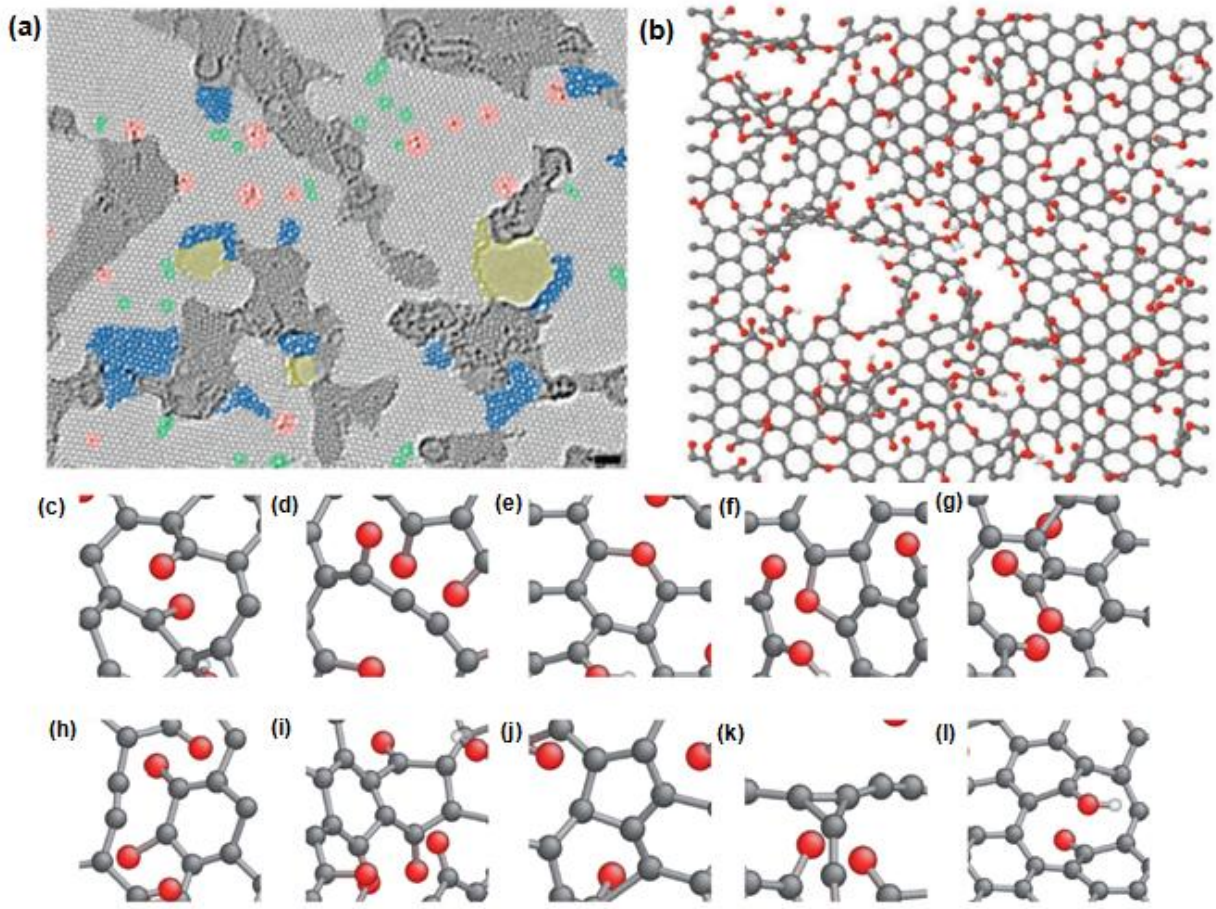

Figure 1.11 – Alterations in the surface morphology of GO upon reduction. Aberration-corrected HRTEM (a) of a single-layer RGO membrane [17], with colors indicating specific defects. An atomic model (b) illustrate the topological defects and remnant oxygens after reduction[39]. Post-annealing, remnant oxygens and isolated carbons are present in the form of (c) carbon chains, (d) pyran, (e) furan (f) pyrone (g) 1,2-quinone, (h)1,4-quinone, (i) five-carbon ring, (j) three-carbon ring and (k) phenols. Carbon, oxygen and hydrogen are grey, red and white respectively[39]

1.6. Surface Manipulation of GO

While GO gained enormous popularity initially as a precursor to large-scale synthesis of graphene, in recent years, focus has gradually shifted from firstly trying to understand its structure, to now manipulating its surface chemically[10], [40]–[43]. Surface manipulation of GO can broadly be categorized into organic (1.6.1) and inorganic (1.6.2) tuning of its chemical composition. This section summarizes prominent works in both areas, and is critical in realizing the motivation for this thesis.

1.6.1. **Organic Manipulation of GO**

Because of its excessively inhomogeneous structure, attaining chemical control over GO is a *major* challenge. A recent paper by Compton *et al.* focuses on utilizing GO as an active chemical platform susceptible to further functionalization reactions, without compromising its electrical properties[44]. They report a means to synthesize chemically active reduced graphene oxide (CARGO) with higher C/O ratios than conventional chemically reduced graphenes (CRGs) while retaining its electrical conductivity. Current methods to reduce GO result in CRGs with good electrical conductivity, but extremely high C/O ratios, making them chemically inactive for further reactions (i.e. biocompatible graphene and as a template for DNA attachment)[45], [46]. CARGOs are stable in organic solvents, presumably due to the electrostatic stabilization provided by remnant functionalities on the surface, which permits further solution processing.

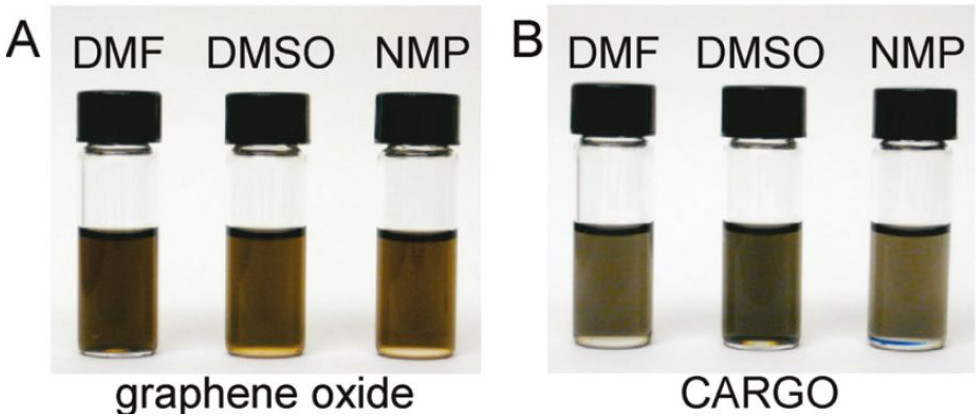

Figure 1.12 – Stable solutions of GO and CARGO in various organic solvents[44] .

As seen in Figure 1.12, the authors specifically focus on dimethylformamide (DMF), dimethyl sulfoxide (DMSO) and N-Methyl-2-pyrrolidone (NMP) as solvents. The reason why these are chosen over THF, in which GO also forms stable solutions (see Figure 1.3) is their high boiling points (>150 ^{o}C). TGA curves show significant mass loss of GO at approximately 150^{o}C after thermal treatment, which can be attributed to loss of oxygen functionalities. The thermal treatment, which takes place in solution, makes the aforementioned organic solvents ideal candidates. The C/O ratios are further tailored by varying reaction parameters such as reflux time and reaction temperature to the extent that the C/O ratio of CARGO can be tuned in solvent from 2 to 10. An instance where such functionalized graphene is superior alternative to graphene itself is in the areas of electrochemical sensing and charge storage [47].

1.6.2. **Inorganic Manipulation of GO**

Manipulating the surface of GO inorganically can be further sub-categorized into two distinct categories. The first is termed surface 'functionalization', which relies on reactions of external inorganic compounds with specific functional groups on the basal plane or edges of GO. The second category involves 'doping' elements into the graphitic lattice itself. Both approaches have led to breakthrough works, and have reaffirmed the significance of continuing research in external reactions on the surface of GO. Some relevant advances are presented in the following sub-sections.

1.6.2.1. **N-Doping of Graphene Oxide**

A popular means to dope the graphitic lattice with nitrogen while simultaneously reducing GO was developed by Li *et al.*[48] By thermally annealing GO in ammonia (NH_3), the authors observed reduction of oxygen functionalities and subsequent doping of nitrogen, starting at temperatures as low as 300^{o}C. Over the course of the developed procedure, a maximum of ~5% N was doped (at 500^{o}C), while the oxygen content decreased from ~28% in GO to 2% after annealing at 1100^{o}C. This is in agreement with findings from Bagri *et al.* [48]. The carboxylic acid, carbonyl and lactone groups were hypothesized to be initiation centers for reaction with NH_3 and formation of the C-N bond. The electronic properties of N-doped graphene were dramatically altered due to this, as it exhibited n-type electron doping behavior, thus providing a chemical route to n-type graphene which has direct applications in a number of fields.

1.6.2.2. **Covalent Bulk Functionalization of graphene**

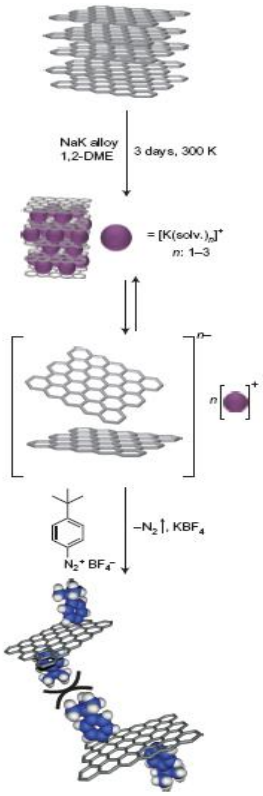

Figure 1.13 – Intercalation of NaK alloy within GO sheets followed by subseqent covalent functionalization using, in this case, 4-*tert*-butylphenyldiazonium tetrafluoroborate (BPD) [49].

In this study by Englert *et al.*, the answers to two critical problems are addressed by means of covalent bulk functionalization[49]. While graphene has shown a lot of promise as a substitute to silicon in next-generation microelectronics, it has very low solution processability and a zero bandgap[6][7][16]. Covalently altering the π-conjugation by introducing chemical bonds resolves both queries. Interestingly, the authors start by bulk functionalization of pristine graphite, as seen in Figure 1.13. The first step of the reaction is the intercalation of graphite with a

liquid, sodium-potassium (NaK) ally and 1,2-dimethoxyethane (DME), an inert solvent. The point of the intercalation step is to *reduce* graphite by solvated electrons using NaK alloy as a source. This process, known as 'reductive activation' of graphite, prepares it for the functionalization step (i.e. reaction with diazonium salts) in desired proportion. The negatively charged graphene is essentially oxidized by diazonium cations ($Ar\text{-}N_2^+$) leading to the formation of highly reactive aryl radicals which are engulfed into the aromatic domain of graphene. As seen in the bottom part of Figure 1.13, this leads to intermolecular stacking into graphitic sheets with a sterically hindering functional group sticking out from the surface. Covalent functionalization also prevents re-aggregation of graphene in solution, while the sheets themselves are in the micrometer range, making them applicable as lithographic contacts. Altering the nanoscale composition of graphene in such a way is seen to have direct, improved effects on its electron mobility and solubility, increasing its potential in graphene-based microelectronics.

1.7. Motivation for Existing Work

Over the course of this chapter, graphene, which is an essential building block for a range of nanomaterials, has firstly been introduced. The fame it gained especially after receiving the Nobel Prize for Physics in 2010, was tremendous, intuitively resulting in a widespread research towards its large-scale synthesis. It was due to this upsurge that GO, an insulating, disordered and chemically inhomogeneous counterpart of graphene first garnered traction. The roots of GO, however, go a lot farther back in time: it was first "discovered" by British physiologist Sir Benjamin Brodie in 1859 since which its structure and synthesis have undergone various transformations, both of which have been discussed. Methods proposed for chemically reducing GO are then presented, with the following goals: (i) remove all oxygen from the surface of GO and (ii) restore the aromatic sp^2 domain to mimic characteristics of graphene as closely as possible. As elegant as each of the methods presented in literature are, they have distinct limitations, such as either containing remnant oxygen, causing morphological alterations or doping the graphitic domain with external atoms.

Consequently as the attention slowly shifted on GO itself, to tailoring its chemical characteristics by attaining *control* over the organic moieties on its surface. Over the past few years, a number of reports have surfaced that address the impact of both organic and inorganic functionalization on the macroscopic properties of GO, RGO, and in some cases, how it is a superior alternative to graphene itself. Examples

of each case have then been presented to elucidate the impact of such works[19], [48], [49].

The focus of this thesis, entitled “Surface functionalization of Carbon Materials”, is along the same direction. The second chapter deals with my first work, which presents a facile method to controllably, partially and *selectively* reduce GO, and in the process alter its chemical and optical properties. Obtaining ‘control’ over the surface of GO has always been thought as one’s ability to tune the C/O ratio, but experimentally, no one had proven evidence of selective reduction till the release of this work. The third chapter then looks at inorganic manipulation of GO, in the form of fluorinating the basal plane, and how this causes a drastic change in the wetting characteristics of GO. The ability of GO to form stable solutions in organic solvents enabled us to deposit it onto any desired substrate by an innovative method (See Chapter 3). Lastly, surface functionalization in this thesis has not been limited to graphene oxide itself; carbon nanotubes (CNTs), which are part of the graphene family, have been introduced in Chapter 4. The surface of CNTs has been functionalized with a fluoropolymer to tailor their affinity towards organic solvents. CNT-polymer composites were then synthesized, that have direct applications in CO_2 recovery.

This thesis reports critical advances in chemical control of graphene oxide and inorganic functionalization of both graphene and carbon nanotubes. These results have led to additional projects that have been initiated in these areas, and improvements in each of the works, both of which are briefly discussed in Chapter 5.

Chapter 2

Organic Manipulation of GO: Stepwise Reduction

I consider this chapter to be extremely critical in my thesis, and shaping the direction my PhD took. While a number of studies had looked at different methods for reducing GO and manipulating its C/O ratio, none had experimentally observed the effects of partial reduction and the chemical behavior of functional groups upon reduction. I approached this problem with the motivation to tune the chemical structure of GO with a lot more specificity than what had been published in literature, with the expectation of learning more about the random abundance of functionalities present on its surface. In terms of broad groupings of surface manipulation outlined in Chapter 1, this comes under the 'organic manipulation sub-category.

2.1. General Introduction & Motivation

Due to its exceptional electronic, mechanical and optical properties, and potential for applications, graphene, and methods for its synthesis have garnered a lot of attention[6], [7], [49]. A widely adopted approach that has shown great promise is the chemical reduction of graphite oxide, due to which in recent times, gaining insights into the heterogeneous structure of graphene oxide (GO) has been the focus of numerous studies. GO is a complex chemical system consisting of a graphene sheet covalently bonded to oxygen-bearing groups, with epoxy and hydroxyl functional groups occupying the basal plane, and carbonyl, carboxylic acid and lactol functionalities attached to the edges[9]. The presence of these moieties results in a disruptive sp^3/sp^2 hybridized network and a reduced number of conductive pathways, giving GO its insulating characteristics.

As mentioned previously (Section 1.5), 'conventional' methods that are employed to efficiently reduce GO include, but are not restricted to reaction with $NaBH_4$, hydrazine and thermal annealing. Recently however, the focus has shifted to GO itself particularly in terms of the alterations in its sp^2/sp^3 fraction and achieving control over its chemical characteristics as it is reduced. For instance, *Bagri et al*.[39] report significant insights into the reduction of GO upon thermal annealing based on molecular dynamics simulations (Figure 1.11, (c) - (f)). Other studies that attempt to manipulate the C/O ratios of chemical modified graphenes (CMGs), involve annealing at temperatures greater than 150^oC or the use of specific polar organic solvents. More importantly, there is no evidence of *chemical selectivity* or

control over the organic functionalities the GO surface [44]. Heating at higher temperatures results in pyrolysis of organic moieties making it tedious to extract explicit information about individual organic groups[33]. A combination of these limitations calls for a facile method at less harsh reaction conditions.

To circumvent these issues, this chapter presents a protocol for reduction of GO using a gas-based hydrazine method, exhibiting specific control over each organic moiety. *Stepwise* removal of functional groups is demonstrated, thus for the first time elucidating the *order* of reduction of each functional group from the surface of GO. Free standing graphite oxide membranes are reduced by exposure to hydrazine vapors at times ranging from 30 minutes to one week (168 hours). ATR-FTIR measurements on each of the partially-reduced graphene oxide (pRGO) films show sequential removal of functional groups from GO, with a direct correlation to the time of exposure to hydrazine vapor i.e. the extent of reduction.

Being able to experimentally control the functional groups on GO in the form of a micron-thick film has a great advantage – the ability for bulk solution processing. Due to each group being reduced in a stepwise fashion, there are always remnant organic moieties on the graphitic plane, which allows for stable solutions forming in organic solvents, due to the electrostatic repulsion effect mentioned by Kaner and coworkers[50]. The relatively mild nature of hydrazine vapors is much more suited for stepwise reduction compared to existing reduction methods which involve harsh reaction conditions and extremely fast kinetics making it virtually impossible to gauge the chemical behavior of each group. Hydrazine vapors also

allow the reduction to be carried out at room temperature with only a dessicator being the necessary equipment.

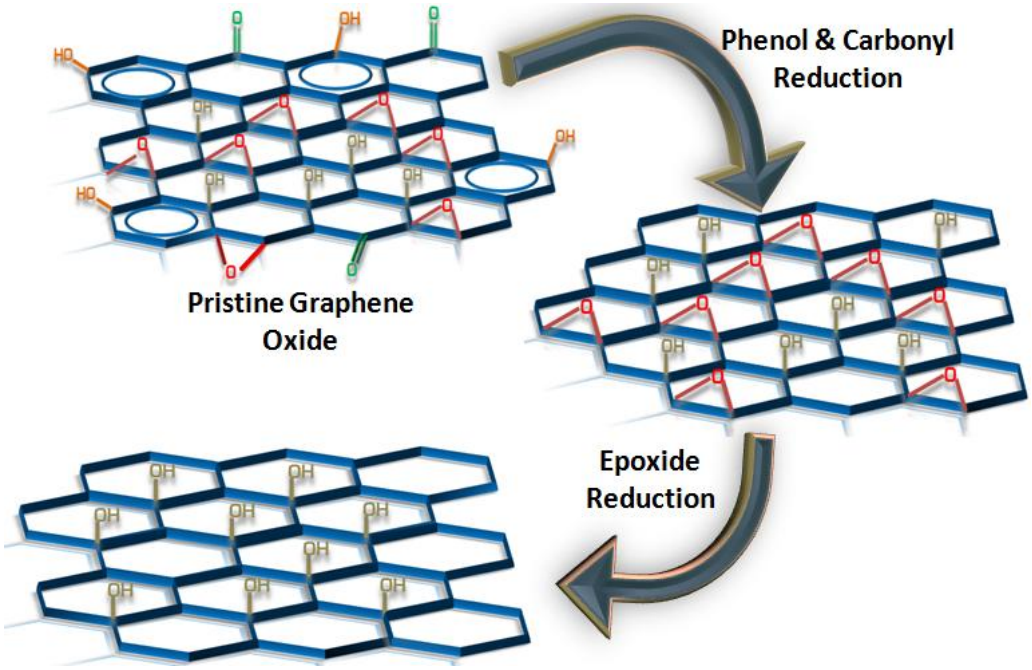

Figure 2.1 – Schematic showing the transitions in the chemical structure of GO as it is reduced after hydrazine vapor exposure. The carbonyl group is the first to be reduced, followed by the phenol and epoxides, and finally the tertiary alcohol.

2.2. Experimental Methods

2.2.1. **Synthesis of GO**

Graphite powder (flake size 45m, >99.99% purity) was oxidized using the improved method protocol (Section 1.3.3) and subsequently washed, dried and filtered as outlined in the procedure[27]. The result was a fluffy, yellowish-brown powder that formed stable colloidal dispersions in deionized water (2 mg/mL) with no settling observed over the course of 2 weeks.

To fabricate free-standing GO membranes, the above mentioned solutions were vacuum-filtered through 25 nm mixed cellulose ester membrane (Millipore), followed by overnight drying in a vacuum dessicator while on the filter paper[14]. The film is not exposed to heat due to the possibility of thermal reduction of labile oxygen. After 24 hours, the resulting membrane is easily peeled off the filter paper to yield a flexible, free-standing GO film.

2.2.2. **Reduction of GO**

An open, 25 mL bottle of hydrazine hydrate (Sigma Aldrich) was placed inside a larger beaker (to prevent spillage) and placed in a vacuum dessicator. The circular, free-standing GO film was cut into 6 equal pieces (~55 mg) and exposed to hydrazine vapors under vacuum in times ranging from 30 minutes to 7 days. Each film was removed from the dessicator after the desired time of exposure and *not* inserted back in. Over the course of reduction the color of films was seen to proceed

from dark brown to black, depending on the duration of exposure. Free-standing films were preferred over GO powder as they allowed for equal exposure of the film surface.

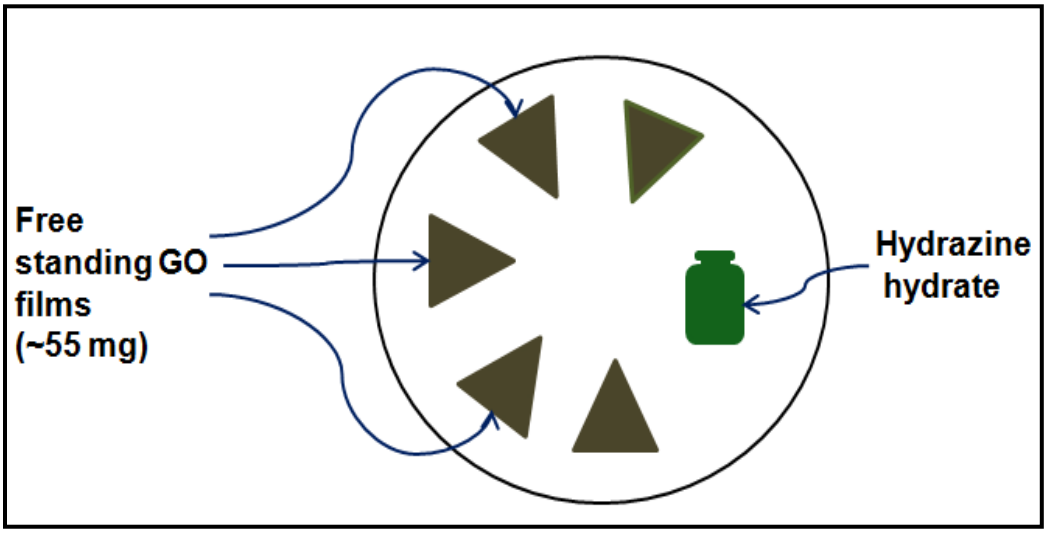

Figure 2.2- Hydrazine vapor reduction schematic with free-standing GO films placed in the desicator.

Figure 2.3 - Hydrazine dessicator set up. The reduction is conducted at room temperature in vacuo, with an open hydrazine container.

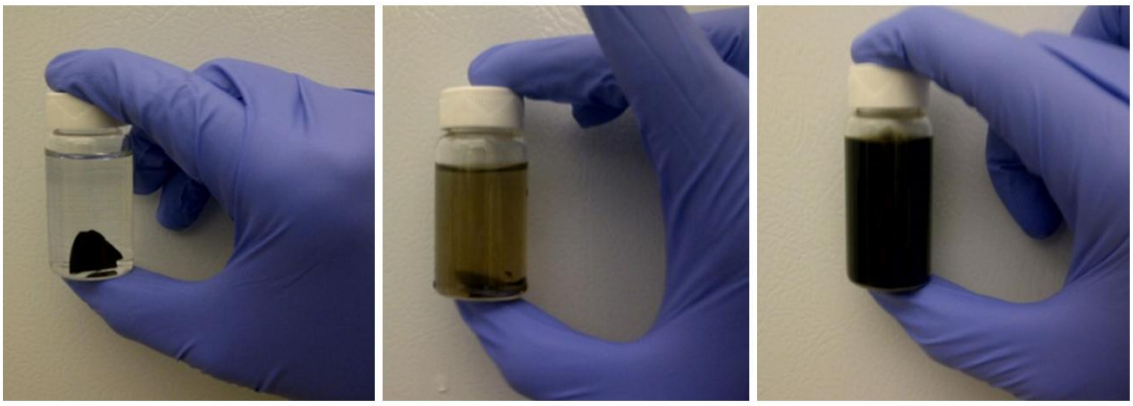

Figure 2.4-Solubility of free standing films of partially reduced GO (pRGO) at different stages of reduction in deionized water[16].

2.2.3. **Analytical Techniques**

Fourier Transform Infrared (FTIR) Spectroscopy analysis was done on a Nicolet FTIR microscope with a MCT/A detector in the ATR (Attenuated Total Reflectance) mode. For UV-Vis spectra, GO solutions were prepared in deionized water (250 mg/L) while pRGO solutions required sodium dodecylsulfate to form stable suspensions in DI water. Absorption measurements were done on a Shimadzu 3600 UV-Vis spectrophotometer. XPS analysis was done on a PHI Quantera x-ray photoluminescence spectrometer, at a chamber pressure of 5 x 10^{-9} torr, and Al cathode as the x-ray source, with power set to 100 W. The pass energy for the survey scan was 140.00 eV.

2.2.3.1. **Band gap Measurement – Tauc's Analysis**

An indicator of the extent of reduction is the optical gap of GO. A number of previous studies have reported the optical band gap of graphene[51], graphene

oxide[10],[52],[53] and boron nitride-graphene hybridized structures[54] using Tauc's analysis, a mathematical approach to calculate the optical band gap of amorphous materials. A typical Tauc plot looks as follows (shown in the inset of Figure 2.5):

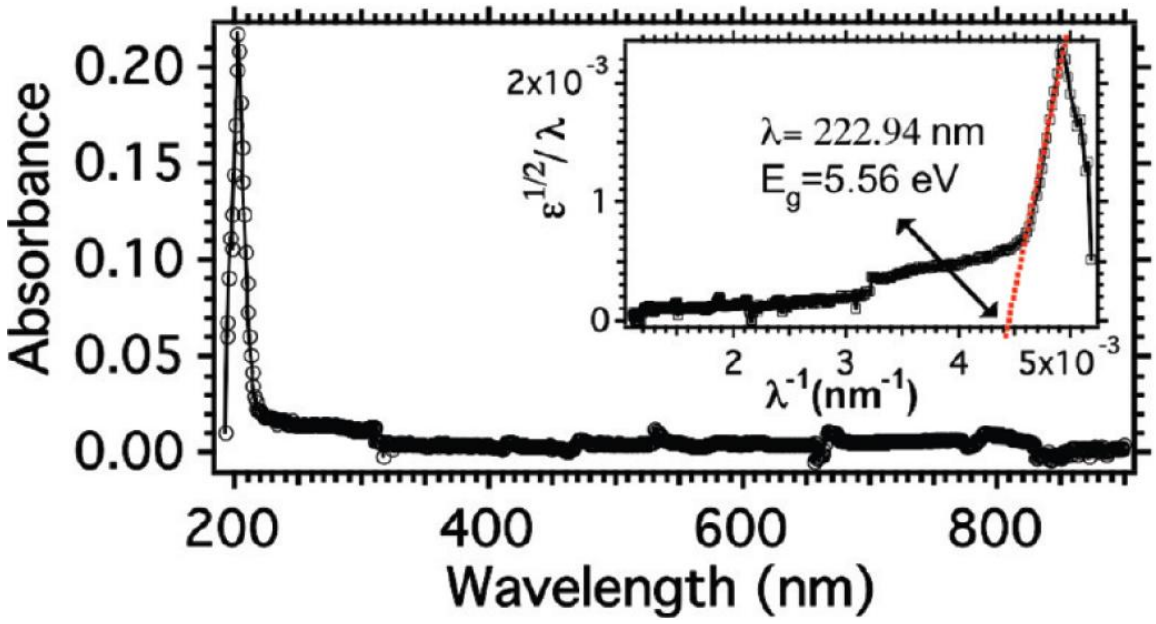

Figure 2.5 – Ultraviolet absorption spectra and the corresponding Tauc plot (inset) of a hexagonal BN film grown via CVD[54].

The abscissa typically represents the energy of the light (hν) which is normalized to λ^{-1} in this case, while the y-axis consists of a normalized absorbance ($\varepsilon^{1/2}/h\nu$). Previous studies that have reported the optical gap of graphene oxide have been between 3.3 – 3.6 eV[52], [53], [55],[56].

2.3. Results & Discussion

Looking at the characteristic ATR-FTIR peaks seen on a free-standing film of GO, all the functionalities are accounted for. Each of the peaks within the 800 – 2000 cm^{-1} region have been explained: while hydroxyl (-OH) groups do feature a prominent absorption band between the 3000 – 3500 cm^{-1} region a large contribution is due to intercalated moisture between GO sheets. Instead, precise information about the nature of alcohol functionalities has been pointed out in the 800 – 2000 cm^{-1} region.

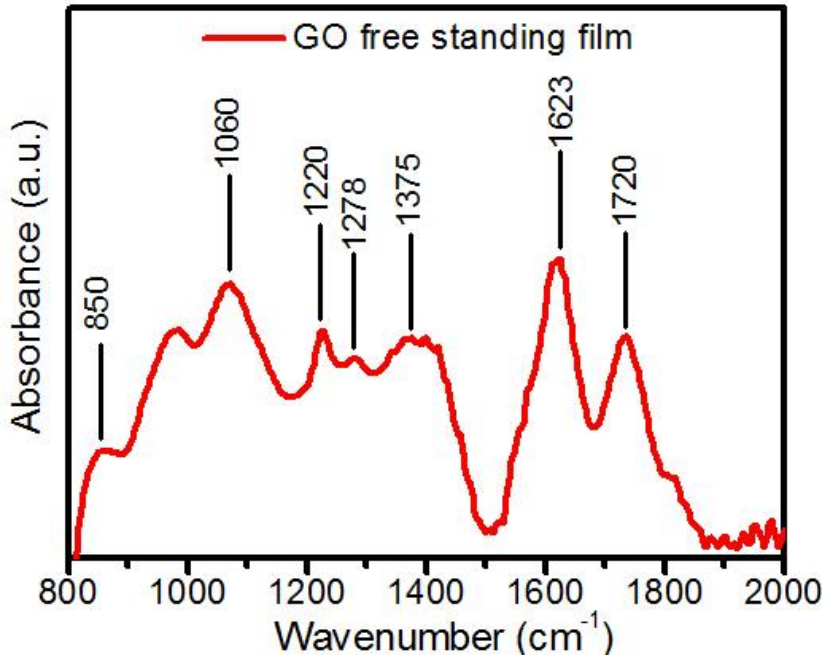

Figure 2.6 – ATR-FTIR of a free-standing film of graphite oxide. Looking at the 800-2000 cm^{-1} region, all the characteristic functionalities are accountted for. These include the epoxide bending (850 cm^{-1}), alkoxy vibrations (1060 cm^{-1}), epoxide stretching (1220 cm^{-1}), phenolic moieties (1278 cm^{-1}), tertiary alcohol vibrations (1375 cm^{-1}) and carbonyls (1720 cm^{-1}).

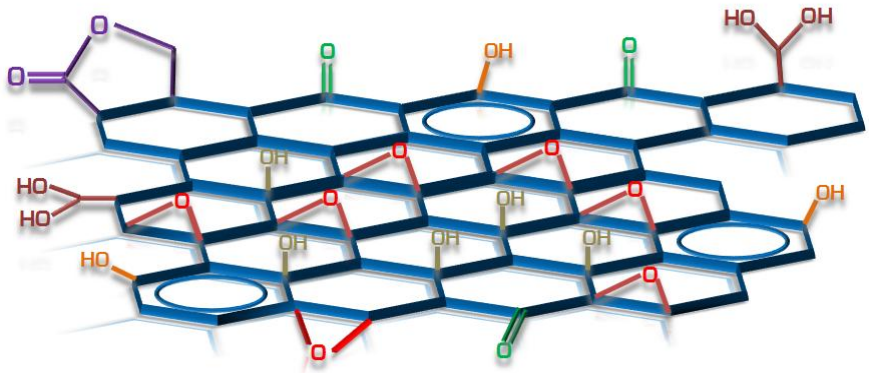

Figure 2.7 – A typical structural model for GO. All moieities presented in the FTIR are accounted for; carbonyl (green), epoxide (red), phenols (orange) and tertiary alcohols (grey).

In Figure 2.6, the peaks at 850 cm^{-1} and 1220 cm^{-1} represent the bending and asymmetric stretching modes of the epoxy (C-O-C) group and the 1060 cm^{-1} peak represents alkoxy (C-O) group vibrations. Alcohol moieties are differentiated as follows - the peak at 1278 cm^{-1} corresponds to phenolic groups (henceforth referred to as Ar-OH) while the tertiary alcohol bending is accounted for by a peak at 1375 cm^{-1}. This peak isn't resolved in Figure 2.6 due to a broad series of peaks spanning the 1300-1450 cm^{-1} region but becomes more obvious upon stepwise reduction. The feature at 1420 cm^{-1} corresponds to aryl stretching (C=C) and dominates the spectrum in this case, while the sharp peak at 1623 cm^{-1} is due to skeletal vibrations of the graphitic domain. Lastly, carbonyl (C=O) stretches are accounted for by the peak at 1720 cm^{-1}. Based on the FTIR data the structure of GO presented in Figure 2.7 is considered to be similar to that proposed in literature[57]–[60].

Free-standing films of GO were then exposed to hydrazine vapors. The first noticeable changes in appearance were within the first 2 hours of exposure,

particularly as the color of films increased in degree of darkness (i.e. going from light brown to dark brown and then to black on further exposure.) Noticeable changes were also recorded in FTIR spectra of partially reduced GO films. These spectra have been presented in Figures 2.8, 2.9 and 2.10 respectively. Looking at Figure 2.8, spectral changes are seen in the intensity of the carbonyl and phenol peaks. After 150 min (2.5h) of hydrazine exposure, there is an unambiguous drop in the intensity of the carbonyl peak, which continues to drop till the whole peak completely disappears from the spectrum at 8h. The phenol (Ar-OH) peak showed a similar, chronological decrease, starting with a well-resolved peak in GO at 1278 cm^{-1} which de-intensifies initially after 2.5h and is completely reduced after 16h. This is the first experimental evidence of the carbonyl and phenol group being reduced at different times when exposed to hydrazine vapors.

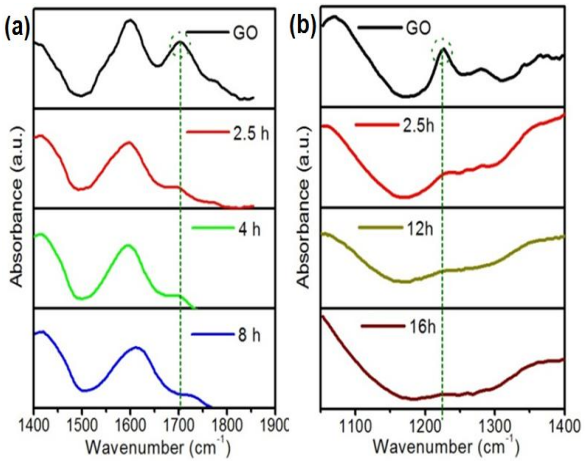

Figure 2.8 – FTIR spectra reveal sequential reduction of the (a) carbonyl (1720 cm^{-1}) and (b) phenol (1278 cm^{-1}). From the spectrum, the carbonyl group is seen to be completely reduced after 8 hours, while the phenol moiety is reduced at 16 hours.

Since different vibration modes of the epoxide group is represented by two peaks, the instance of epoxide removal was only identified after the intensity of both the peaks was no longer detected. The peak seen in Figure 2.9 (b) at 1220 cm^{-1}, corresponding to the asymmetric stretch, is the first to decrease in intensity and completely disappears from the spectrum after 4h of exposure. The epoxide bending peak seen at 850 cm^{-1} (Figure 2.10 (b)) can still be detected after 4h and is only completely reduced at 21.5h, indicating complete elimination of epoxide moieties.

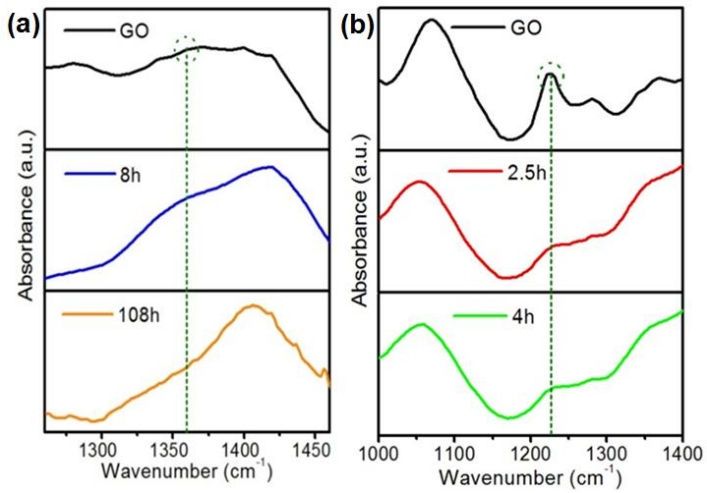

Figure 2.9 – FTIR spectra also show sequential removal of the (a) tertiary alcohol (1365 cm^{-1}) and the (b) epoxide (1220 cm^{-1}, molecular stretching) groups too. The tertiary alcohol group is reduced after 108 hours of hydrazine exposure, while there is a reduction in epoxide stretching intensity after 4 hours.

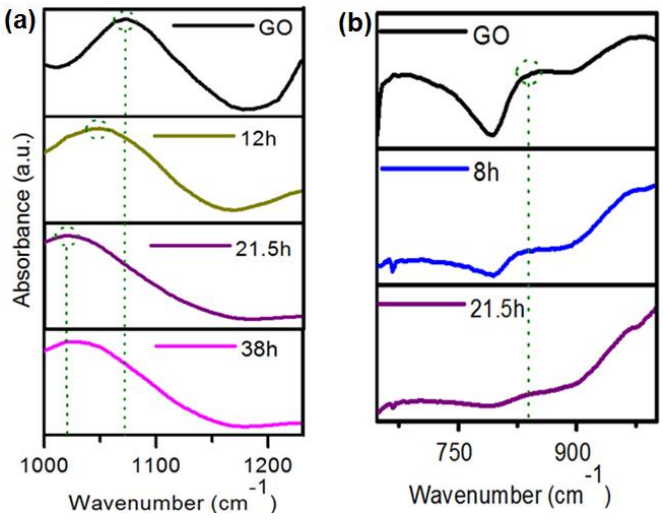

Figure 2.10 – The alkoxy peak (a) is seen to progressively shift from 1060 cm^{-1} to 1020 cm^{-1}, being a possible indicator for nitrogen-substitution at alkoxy sites. Lastly, complete reduction of the epoxide functional group only occurs after 21.5 hours (b).

The last moiety to be reduced is the tertiary alcohol (Figure 2.9 (a)). Initially, its characteristic peak at 1375 cm^{-1} can't be resolved in the broad feature between 1300 – 1450 cm^{-1}. After hydrazine exposure a significant change in its line shape is observed at 8h, indicating a decrease in the spectral weigh of a peak embedded within the band. Tertiary alcohol groups are known to absorb at 1375 cm^{-1} in their bonded state due to OH deformation, which is exactly where this decrease in spectral weight is observed[57]. The absorption intensity continues a gradual decrease and levels off after 108h of continuous hydrazine exposure. The only remaining peak is at 1420 cm^{-1} which is attributed to the stretching mode of aryl (C=C) bonds. Thus, we conclude that tertiary alcohol groups undergo near-complete removal only after 108h. The reason for their removal occurring much later than the

other functional groups is hypothesized to be due to steric hindrance hindering the reaction process. Previous studies have raised concerns regarding the possibility of hydroxyl groups not being reduced at all [33], and these results are in conjunction with those reports.

From the results obtained *via* ATR-FTIR trends in our data show the carbonyl group to be the first to be reduced at 8 hours, after which the phenol and epoxy groups are reduced at 16 and 21.5h each. The tertiary alcohol is the last to be reduced, after 108h.

Both Stankovich *et al.*[33] and Park *et al.*[19] report the incorporation of nitrogen into the aromatic domain during hydrazine reduction and our FTIR data bolsters these claims. The alkoxy group is represented by a single peak at 1060 cm^{-1} which gradually blue shifts as the time of hydrazine exposure increases (Figure 2.10 (a)) to ~1020 cm^{-1}. After 38h, no further blue shift is observed. Peaks near the 1020 cm^{-1} region are attributed to either in-plane aromatic vibrations or C-N moieties[57]. In addition to previous knowledge about the possibility of C-N bond formation during hydrazine reduction, elemental analysis showed the presence of nitrogen in partially reduced samples and the C/N ratio decreased from about 200:1 to 22:1. A conclusion that can be drawn from this result is that a substitution reaction is occurring between the hydrazine and the alkoxy bond, due to which no peak is detected at 1060 cm^{-1} in the spectrum. These findings compare differently to other studies. However, this is due to different reduction methods, thus implying completely separate reduction mechanisms for each mode of treatment.

The band structure of GO is another property that has been difficult to understand due to a large degree of structural and chemical inhomogeneity. Theoretical studies have suggested an energy gap that is directly dependent on the sp^2/sp^3 ratio[55], [61] which has also led to further reports on the origin of fluorescence in the material. In order to evaluate the extent of partial reduction we decided to *experimentally* look at the transition in its optical band gap. Previous reports have attempted to show a similar transition in the optical gap, but have done so during oxidation of graphite[61], [62]. The extremely rapid kinetics of oxidation makes it virtually impossible to identify the instance at which *each* functional group covalently bonds to the graphite, and furthermore, no steady increase in optical band gap is reported. Instead by using facile hydrazine vapors, the intention is to correlate the instance of removal a particular functional group to a corresponding decrease in the optical gap. Upon hydrazine exposure a gradual red-shift in the UV- Vis peak position is noted. Traditionally GO shows a characteristic peak at 226 nm, which after 108h of hydrazine exposure shifts to 261 nm. Peak positions have been presented in Figure 2.9, with CCG1 as a frame of reference. CCG1 shows an absorption peak at 264 nm, giving a qualitative idea of the extent of reduction of hydrazine vapors compared to $NaBH_4$. Sodium dodecylsulfate (SDS) which was used to disperse pRGO in deionized water does not show any absorption by itself.

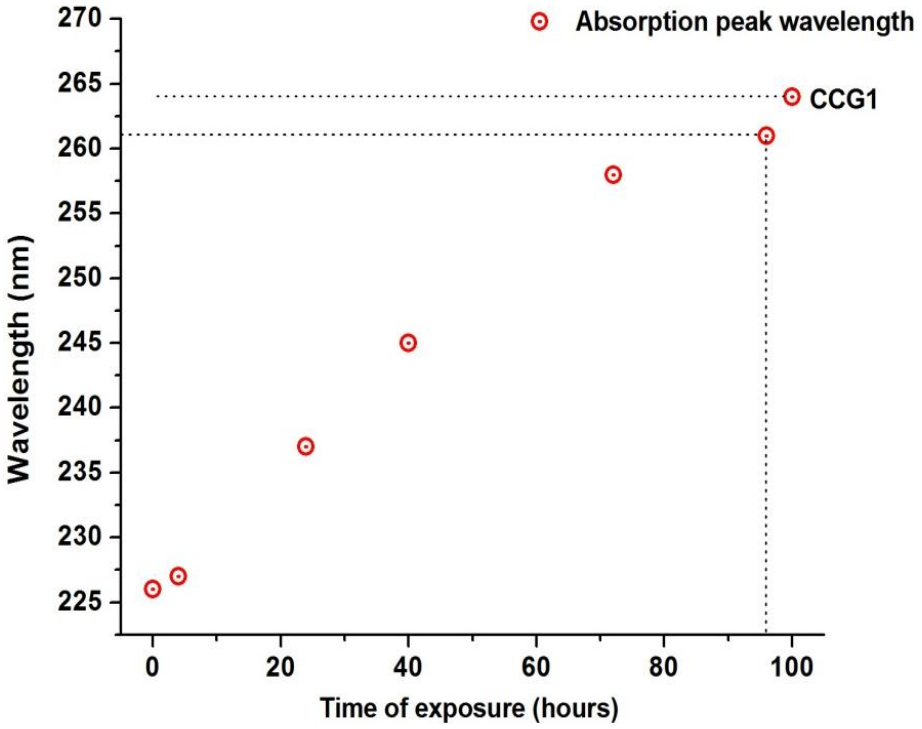

Figure 2.11 – Shift in the absorption peak of GO upon hydrazine vapors. A gradual red-shift is observed, starting from 226 nm up to 261 nm. CCG1, as synthesized Gao *et al.* is presented as a frame of reference.

The energy gap was then calculated from UV-Vis absorption spectra, using the following form of Tauc's expression[51], [54]:

$$\omega^2\varepsilon = (h\omega - E_g)^2$$

In this equation, ε is the measured absorption intensity, ω is the angular frequency ($2\pi/\lambda$) of the incident radiation, and E_g is the optical band gap. Previous reports have calculated the optical band gap of graphene oxide and similar derivatives by plotting ($\varepsilon^{1/2}/\lambda$) against the energy ($hc/\lambda$) and extrapolating the

linear region of the curve down to the x-axis to obtain the numerical value of the optical band gap. Figures 2.12 and 2.13 present Tauc plots that are used to calculate

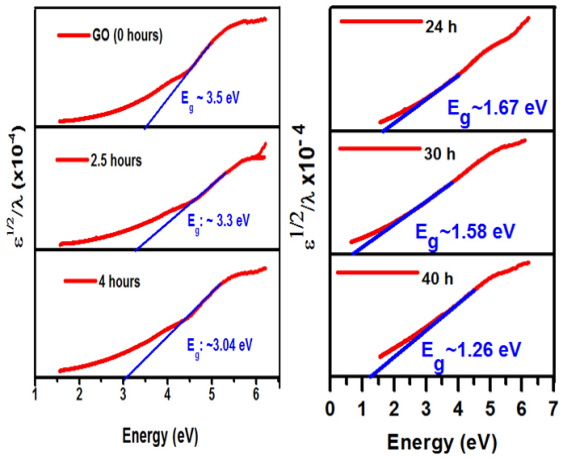

Figure 2.12 – Tauc plots showing a sequential decrease in the optical band gap from 3.5 eV(pristine GO) to 1.26 eV (pRGO @ 40h).

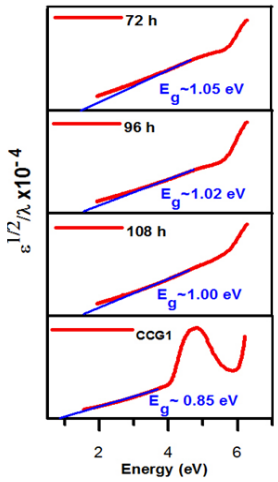

Figure 2.13 – A decrease of optical band gap is seen between 72 to 108 hours, albeit at a much slower rate. The optical gap remains near 1eV, indicating that a majority of oxidation has occurred at this point.CCG1 is shown for comparison.

E_g at different times of exposure. Initially, the insulating characteristics of GO are evident (3.5 eV, 0h) but in a very short time of exposure the partially reduced samples start showing steady decreases in the optical gap. Within the first 2.5 hours, the E_g is extrapolated to 3.3 eV and decreases further down to 3.0 eV after just 4 hours. This decreasing trend continues up to 40h, at which an E_g of 1.26 eV is extrapolated. In conjunction with FTIR data, the drastic initial decrease in E_g is in accordance with the carbonyl, phenol and epoxide moieties being reduced before the first 40 hours. Upon removal of these moieties the E_g progresses towards values that are less characteristic of insulators and more so of semiconductors. This is the first study which reports GO without external functionalization to show an optical gap within such a range. The trend of rapid reduction slows down after approximately 40 hours thus illustrating the increasing difficulty to reduce remnant oxygen groups, particularly the tertiary alcohol. A very minimal decrease in E_g is observed between 72h to 108h (from 1.05 eV to 1.0 eV), after which E_g remains constant. CCG1, as synthesized by Gao *et al.* [9] also has a majority of oxygen removed, with possible alcohols remaining on the basal plane and lactols on the edges, shows an E_g of 0.85 eV, giving an idea of the weak reducing power of hydrazine vapors. From the evidence noted, the hypothesis that each functional group plays a key role in the decrease in optical gap is well represented. Figure 2.14 on the following page summarizes these results.

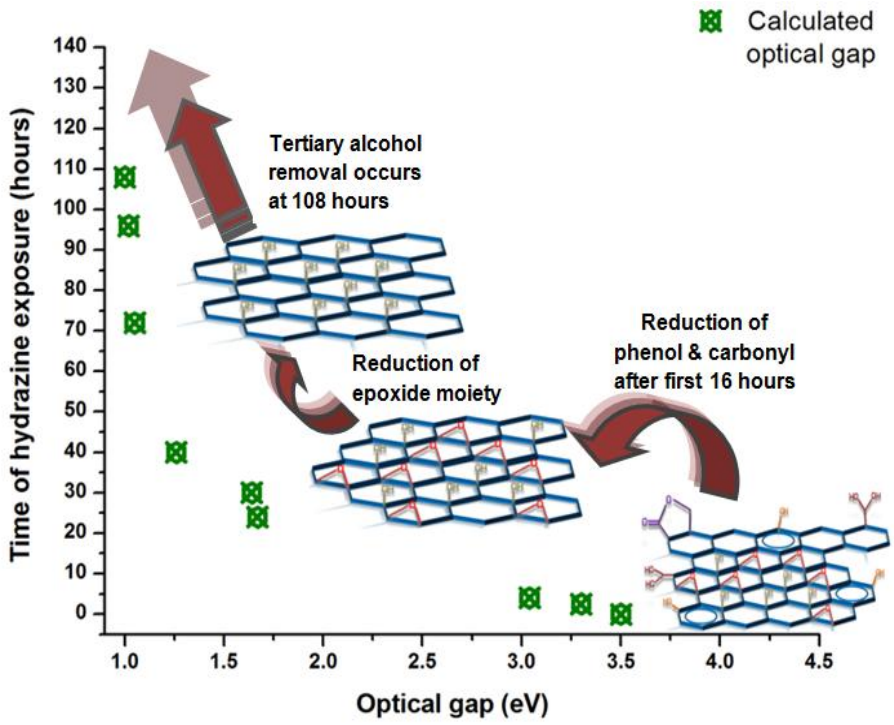

Figure 2.14- A stepwise decrease in the optical gap is recorded after exposure to hydrazine vapors. The hypothesized pRGO is given in the inset.

After being exposed to hydrazine vapors, elemental analysis of free-standing films of pRGO was conducted using XPS with following objectives:

(i) Determine the trends in C/O ratio

(ii) Correlate with the qualitatively determined extent of reaction (i.e. via E_g)

As anticipated, regular increases in the C/O ratio were recorded, and the extent of reduction was much lesser than conventionally harsh methods. Interestingly, certain 'spikes' in the C/O ratio were recorded at particular instances of hydrazine exposure and functional group removal. Figure 2.15 on the next page

shows these increases in C/O ratios, with hypothesized structural changes listed. The first notable spike is seen between 8 to 16 hours, which incidentally is exactly when carbonyl moieties are reduced (Figure 2.8 (a)). Another interesting observation is made after 40 hours, where the C/O ratio remains almost constant, between 3-3.5. After extended hydrazine exposure this C/O ratio increases to approximately 4.5. While this is still *significantly* lesser than values reported by stronger methods (i.e. $NaBH_4$ reduction, thermal annealing), the removal of the tertiary alcohol group follows a similar pattern in both FTIR and Tauc plots. Previously, Robinson *et al*. have reported this issue with hydrazine vapors, wording it as a proof of their 'weak, penetrative nature' [63] leading to incomplete reduction. Identifying the difficulty with removing a particular functional group is a complex problem, since it depends on a number of dynamic variables, which include but are not restricted to the rate of diffusion of hydrazine vapors, the reaction mechanism of hydrazine with each functional group, and quite possibly, the preferential reactivity of a particular group with hydrazine. Some of the mathematical implications of these have been discussed in Section 5.1. Instead, we have been able to identify the functional group associated with the transition into each regime by correlating it with the degree of reduction and the optical band gaps.

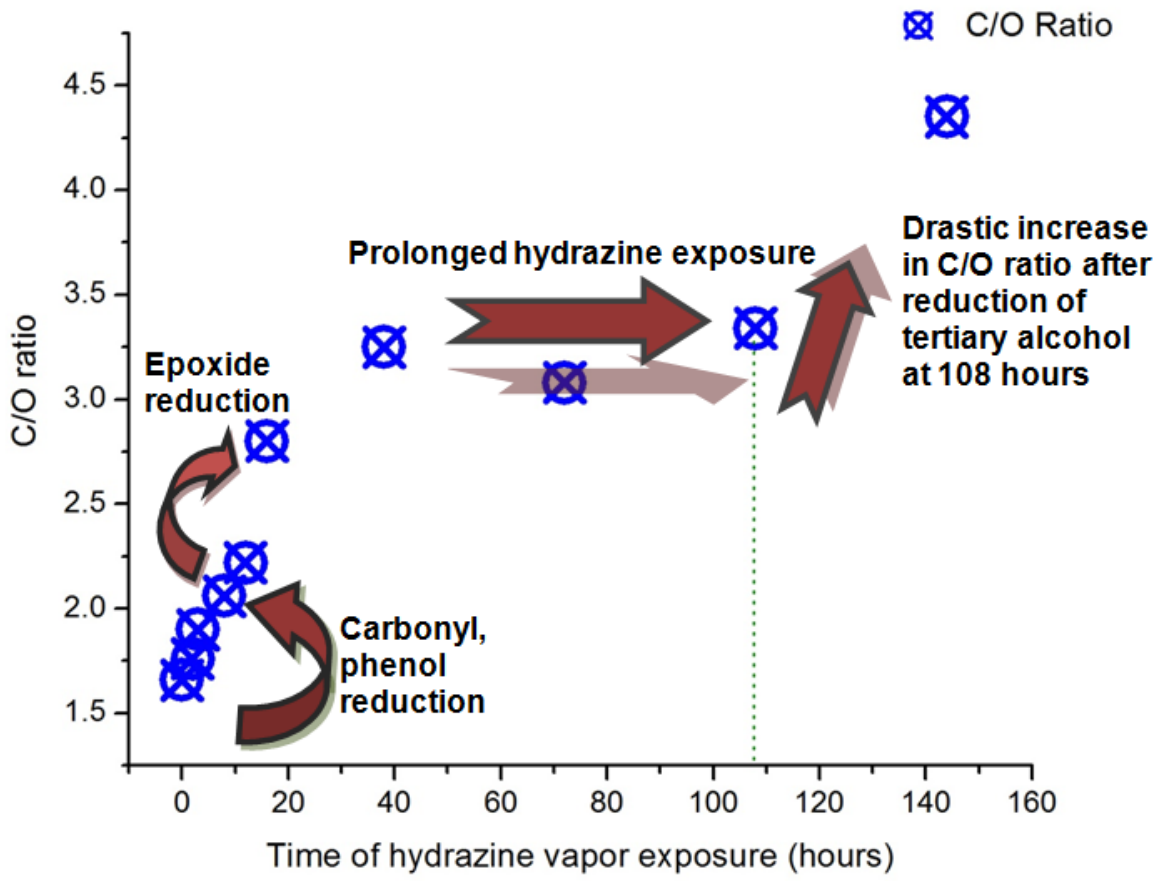

Figure 2.15 – The C/O ratio of free-standing films shows a sequential increase, from a ratio of ~1.7 in pristine GO to a final ratio of ~4.5. Spikes in the C/O ratio are seen at precisely the same time as moeity removal pointed out by FTIR.

2.4. Concluding Remarks

In conclusion, this chapter presents a first look at manipulating the surface characteristics of GO. We devise a room-temperature based reduction scheme that utilizes hydrazine vapors to reduce free-standing films of graphite oxide. Using a combination of characterization techniques, evidence for controlled, stepwise reduction of each functional group has been presented. ATR-FTIR spectroscopy was successfully applied to record the sequential reduction of the carbonyl, phenol, epoxide and tertiary alcohol groups at different times of hydrazine vapor exposure. Tauc's analysis was then used to calculate the optical band gap (E_g) of pRGOs and a progressive decrease was recorded from 3.5 eV (pristine GO) to 1 eV. Elemental analysis using XPS spectra showed a concurrent increase in the C/O ratios at exact intervals of times at which particular functional groups were eliminated. An increase in the C/N ratio was also recorded, suggesting substitution of nitrogen into the graphitic lattice at extended hydrazine exposure times.

The reduction method outlined in this chapter permits, for the first time, isolation of free-standing films of pRGO with desired functionalities. Instead of current efforts to 'open' a band gap in graphene, adopting this top-down approach to close up the optical gap in GO presents a great deal of value. Chhowalla and coworkers have referred to GO as a 'chemically tunable platform'[10] for a range of optical and electronic applications and the results presented in this chapter exemplify that.

Chapter 3

Inorganic Manipulation of GO: Tuning its wetting characteristics

The work presented in this chapter is critical due to two reasons. Firstly, fluorine is introduced on the surface of GO via covalent bonding, thus being the first instance of *inorganic* manipulation. Secondly, this study is the first to manipulate the wetting characteristics of GO chemically. This project was approached with the following motivation: with GO having outstanding solution processability, an approach to manipulate its wetting would result in it being a superior, inexpensive alternative to existing superhydrophobic materials. Simultaneously, fluorination of graphene theoretically has a string of advantages, but a synthetic route has previously posed considerable barriers. The approach presented in this chapter resolves both quandaries, and the resulting material has opened the path for a number of future works in various fields.

3.1. General Introduction & Motivation

The promise of GO as a manipulable organic and inorganic precursor has been evident through various studies. 'Tunability' as seen in Chapter 2, arises from variations in the chemical composition of GO by altering the ratio of sp^2 to sp^3 hybridized bonds and the C/O ratio. Other studies presented towards the end of Chapter 1, have introduced external compounds *via* covalent functionalization on the graphene basal plane followed by stacking individual GO sheets in solution. To reiterate, one of the advantages of GO is its outstanding solution processability, which makes its deposition much less of a barrier provided one has the ability to manipulate it chemically in a controlled manner. Much fewer reports have looked at inorganic manipulation of GO; chemical doping has a direct consequence on the physicochemical properties of GO, as seen in Section 1.6.2 where nitrogen doping leads to n-type behavior in carbon electronics. Since then however, reports have been limited to polymeric and biological materials [52], [64].

Within the broad topic of inorganic functionalization, fluorination of GO is an area that has not been explored greatly. Realizing a chemical approach to fluorinate graphene has a string of advantages, which arise from the carbon-fluorine (C-F) bond. Since fluorine is the most electronegative element in existence[65], the highly polar C-F bond is an attractive alternative to the C-O bond, which has been the subject of studies that report its outstanding electronegativity [66]. The C-F bond also demonstrates exceptional thermal and oxidative stability[67], and the relatively small size of the fluorine atom prevents steric hindrance from being a limitation for

further reactions if required. The versatile C-F bond is also key in biological applications, as paramagnetic centers within fluorine make it a good imaging agent in MRI measurements[68]. Most importantly, the low surface energy of the C-F bond[69] allows one to alter the wetting behavior of a surface. With reference to GO, this implies that by tuning the C/O and C/F ratio on the graphene basal plane, its conventionally hydrophilic behavior ought to be dramatically altered.

Fluorinating graphite-based materials, however, has been attempted in the previous years and imposed major restrictions due to toxicity and corrosivity of fluorinating agents[70]. A direct chemical approach to fluorinate graphene, such as electrophilic fluorination using xenon difluoride (XeF_2)[71] relies on selective, intricate chemistry and also generates unfavorable species. Other fluorinating precursors such as sulfur tetrafluoride and dimethylaminosulfur trifluoride (DAST) have shown superior fluorinating power but the former is an extremely corrosive gas, while the latter is not stable at higher temperatures[72].

With these considerations in mind, this chapter outlines a strategy to synthesize bulk quantities of fluorinated graphene oxide (FGO) with varying C/O and C/F ratios. The synthesized FGOs are in the form of 2-dimensional (2D) nanoflakes, and fluorine exists in the form of aliphatic C-F bonds covalently bonded to the basal plane. In addition to aliphatic fluorine, epoxide, tertiary alcohols, carbonyl and phenolic moieties are also retained on FGO. The one-pot synthesis scheme proposed yields two discrete products with different chemical compositions. These are entitled fluorinated graphene oxide (FGO) and highly

fluorinated graphene oxide (HFGO) respectively and have a chemical composition quite different from GO. As hypothesized, the low surface energy of C-F bonds results in tunable wetting characteristics. Ease of solution processing leads to fabrication of "inks" in volatile solvents that are sprayed on numerous porous and non-porous substrates to yield pinhole-free films that repel *both* water and organic solvents. Current methods to fabricate such surfaces have a number of disadvantages, such as high temperature processing or the use of specific infrastructure, all of which are bypassed by the proposed strategy. This is the first report of a chemical route to graphene-based *superamphiphobic* materials.

3.2. Manipulating Surface Wetting

Understanding the concept of manipulating the wetting behavior of a solid surface fundamentally involves the ability to vary the surface's free energy. The forces involved in the composite solid-liquid-vapor system that is in equilibrium when a liquid droplet is deposited on a solid surface are critical in determining whether the droplet will wet the surface. This section introduces these concepts and defines hydrophilic, superhydrophobic and superamphiphobic surfaces.

3.2.1. **Attaining Superhydrophobicity**

A 'superhydrophobic' surface is defined as one that fulfills the following two conditions for a water droplet (γ = 72.1 dyn/cm)[73]–[76]:

(i) Display an apparent contact angle equal or greater than 150^{o}

(ii) Exhibit low contact angle hysteresis ($< 5^{o}$)

Perfectly superhydrophobic surfaces exist in nature, and the lotus leaf (*Nelumbo nucifera)* is a widely-cited example. Hydrophobicity of the lotus leaf has been suggested to originate due to a combination of surface texture and chemical composition [77]. The surface of lotus leaves consists of papillose epidermal cells and epicuticular wax crystals, as shown in Figure 3.1 (c) and (d), which jut out of the surface. These result in a roughened surface on the micro-scale which traps air within its interstitial spaces, due to which the overall solid-liquid contact area decreases (i.e. contact area between the water droplet and lotus leaf).

Macroscopically, water droplets are observed to be spherical and roll-off at very low angles. SEM images of superhydrophobic leaf surfaces in nature (Figures 3.1 c, d, e) show contrasting surface morphology from those of smooth, wettable surfaces(Figures 3.1 a, b) [77].

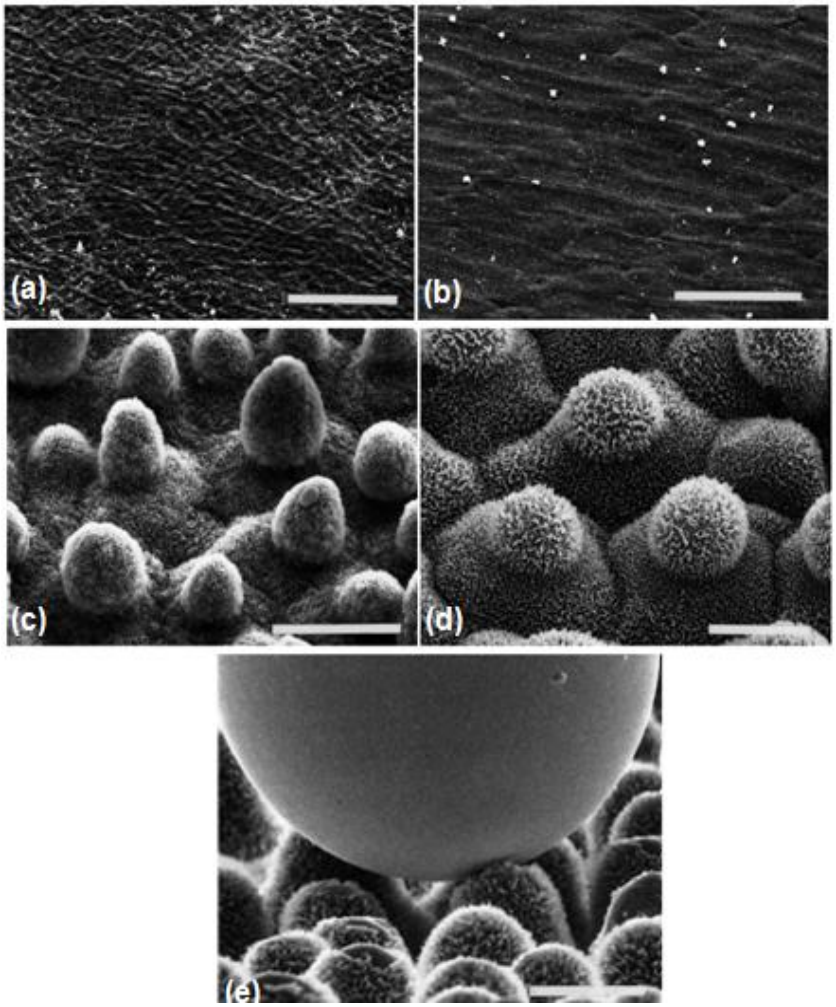

Figure 3.1 – SEM images of smooth, wettable (a,b) and rough, superhydrophobic leaf surfaces (c,d). The *Gnetum gneon* (a) and *Heliconia densiflora* (b) lack any microstructures while the lotus leaf, *Nelumo nucifera* (c) and *Colacasia esculenta* (d) show papillose epiderman cells [77].

From a quantitative perspective, the forces on a water droplet and the ensuing contact angle are explained by Young's equation. On a perfectly flat surface, an ideal droplet is subject to the following interfacial forces:

(i) Interfacial tension of water/air (Υ_{wa})

(ii) Interfacial tension of water/solid (Υ_{ws})

(iii) Interfacial tension of solid/air (Υ_{sa})

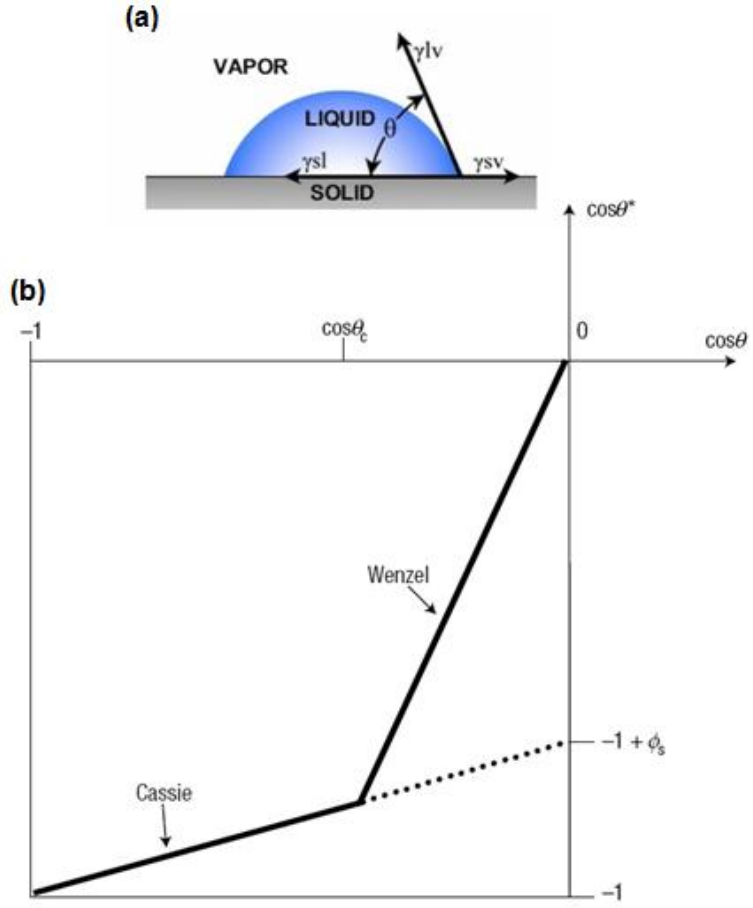

Figure 3.2 – Forces that an ideal water droplet is subject to on a flat surface (a). Wenzel and Cassie states are graphically represented (b), with a metastable Cassie state indicated by a dotted line[73] .

Figure 3.2 (a) shows the respective forces on a droplet of water, and the ratio between the three determines the contact angle (θ) of the droplet. Young's equation mathematically describes the relationship as follows:

$$\gamma_{SA} = \gamma_{WS} + \gamma_{WA} \cos\theta$$

Equation 3.1 – Young's Equation for a droplet resting on an ideal surface

However, a number of contact angles can be recorded for the same droplet placed on a surface. When a droplet is placed on a surface, as its volume increases, so does its contact angle. This increasing angle is known as the advancing angle (θ_{adv}) and is the maximum value of a contact angle that can be recorded. Similary, as a droplet is 'removed' from a surface, its volume and consequently the contact angle decreases. The minimum value of θ that is recorded is known as the receeding angle (θ_{rec}). This phenomenon of a droplet exhibiting an advancing and receeding angle is known as 'contact angle hysteresis' and is critical in understanding the definition of superhydrophobicity. Superhydrophobic surfaces usually display contact angle hysteresis below 5^{o}.

For non-ideal (i.e. roughened) surfaces, two models, in particular, have been developed to further understand superhydrophobicity mathematically. The Wenzel model (Equation 3.2), takes into account the surface roughness and is mathematically represented as:

$$\cos\theta^* = r\cos\theta$$

Equation 3.2 – The Wenzel model, described mathematically. The surface roughness is accounted for by 'r' and is greater than unity, while θ^* is the apparent contact angle on the rough surface

In this equation, θ* is the 'apparent' contact angle on a rough (hydrophobic) surface, whereas θ is the Young's contact angle on the same surface assuming flatness (i.e. an ideal surface). The roughness factor 'r', is simply the ratio of the rough interfacial area over the flat interfacial area on which the droplet is resting. The Wenzel model, however, assumes that there is no air trapped underneath the droplet, and it is solely the increased surface area due to surface roughness that contributes to superhydrophobicity. To bypass this, Cassie-Baxter proposed a mathematical model (Equation 3.3) to calculate the apparent contact angle, with a new variable φ_s, which is the fraction of solid in contact with the droplet.

$$\cos\theta^* = -1 + \varphi_s(1 + \cos\theta)$$

Equation 3.3 – The apparent contact angle for a Cassie droplet. φ_s is the fraction of the surface in contact with the liquid.

Since both equations hold for high values of θ, they can be equated to calculate a 'threshold' contact angle value, θ_c, which quantitatively represents a transition between the two possible wetting 'states' of a water droplet, and has been graphically represented in Figure 3.2 (b).

$$r cos\theta = -1 + \varphi_s(1 + cos\theta)$$

$$(r - \varphi_s)cos\theta = -1 + \varphi_s$$

$$\boldsymbol{cos\theta_c = \frac{\varphi_s - 1}{r - \varphi_s}}$$

Equation 3.4 – Threshold value for the contact angle (θ) beyond which a water droplet is conventionally considered to transition from a Cassie to Wenzel state. Metastable states that are exceptions to this have been recently reported[73]

Figure 3.2 (b) represents the possible states that a water droplet could be considered to be in, when on a rough, superhydrophobic surface. For surfaces that exhibit moderate hydrophobicity ($90< \theta< \theta_c$), the apparent contact angle is calculated using the Wenzel model, and vice versa for the Cassie Model. However, recent reports have shown that the line between the two might not be as black and white as the graph shows. Lafuma *et al.* report the presence of a metastable Cassie regime[73], that has been observed for $\theta< \theta_c$, and is represented by the dotted line in Figure 3.2 (b).

3.2.2. **Attaining Superamphiphobicity**

A 'superamphiphobic' surface is conventionally defined as one that is not wet by solvents with appreciably low surface tensions[69], [78]–[80]. Examples of such solvents are decane (γ = 23.8 dyn/cm), octane (γ = 21.6 dyn/cm) and methanol (γ =

22.5 dyn/cm). In accordance with Young's equation, the lower the surface tension of a solvent, the greater its tendency to homogeneously wet the surface. Quantitatively, superamphiphobic surfaces display contact angles near 150^{o} while maintaining low contact angle hysteresis. Such surfaces are also referred to as 'superoleophobic' surfaces in other reports[69], [75], [80], [81][82]–[84]. A number of studies have attempted to fabricate similar omnirepellant surfaces, amongst which breakthrough findings were published by Tuteja *et al.* [69](2007) and Deng *et al.*[78] (2012). In addition to having a surface with low overall free energy and surface roughness, both these studies present novel ways to further reduce free energy. Broadly, these are:

(i) Increase the surface concentration of –CF, $-CF_2$ & $-CF_3$ bonds (chemically reduce the overall surface energy)

(ii) Introduce surface roughness *via* electrospinning (Figure 3.3)

(iii) Fabricate 'overhang structures' using clean-room techniques to create a composite interface (Figure 3.4)

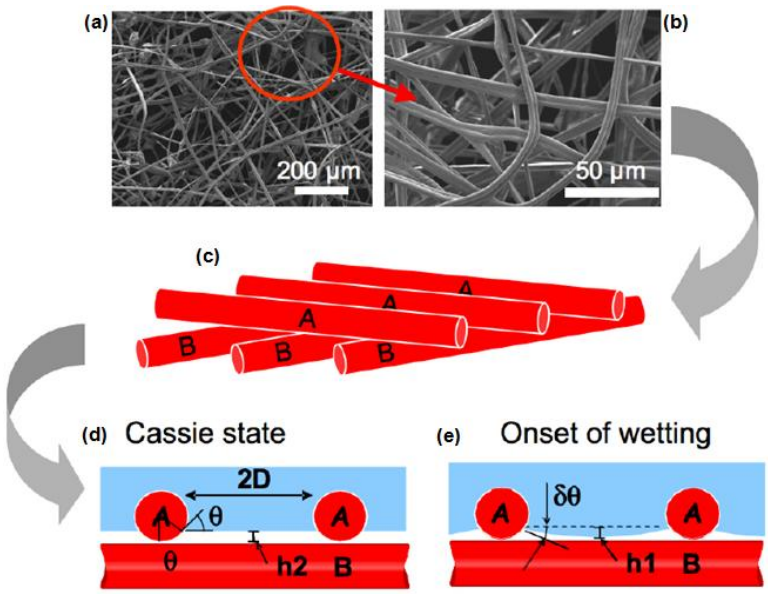

Figure 3.3 – SEM images of an electrospun fiber mat (a, b) which closely resemble the model shown in (c). The anticipated solid-liquid-air interface is illustrated in (d), with the droplet resting in a Cassie State[69].

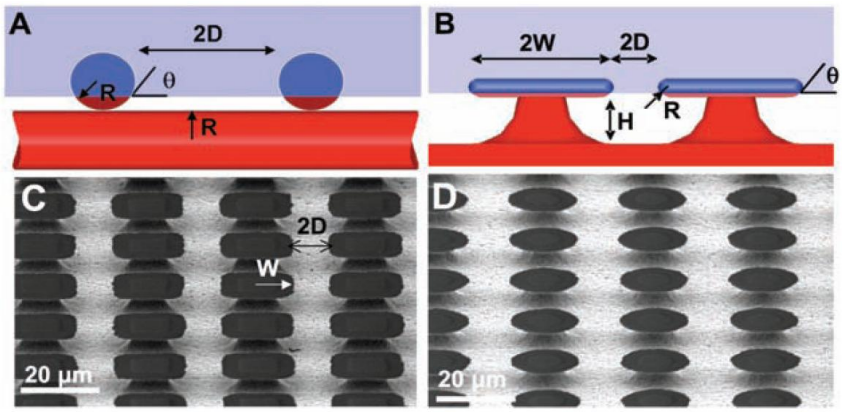

Figure 3.4 – The fabricated 'microhoodoos' by *Tuteja* and coworkers are shown in both schematic (A & B) and SEMs (C and D). Blue represents the wetted surface, whereas red represents non-wetted areas. The design parameters, W,D,R & H are controlled via lithographic techniques. These re-entrant structures lead to the formation of a composite liquid-solid-air interface on a curved surface[69].

More recently, *Deng* and coworkers used candle soot coated with a nanometer thick layer of silica to demonstrate superamphiphobicity. The silica shell is coated using chemical vapor deposition (CVD) of tetraethoxysilane (TES), with ammonia as a catalyst, followed by calcination of the C-Si bilayer at 600°C. Finally, the surface free energy of silica particles is reduced by coating with fluorinated silane, again by CVD. These surfaces exhibited outstanding superamphiphobicity, with static contact angles over 150° with tetradecane (γ = 26.5 dyn/cm). Furthermore, the thin nature of the reported superamphiphobic films is evident in transmittance spectra in comparison to pristine glass. The results are summarized in Figure 3.5.

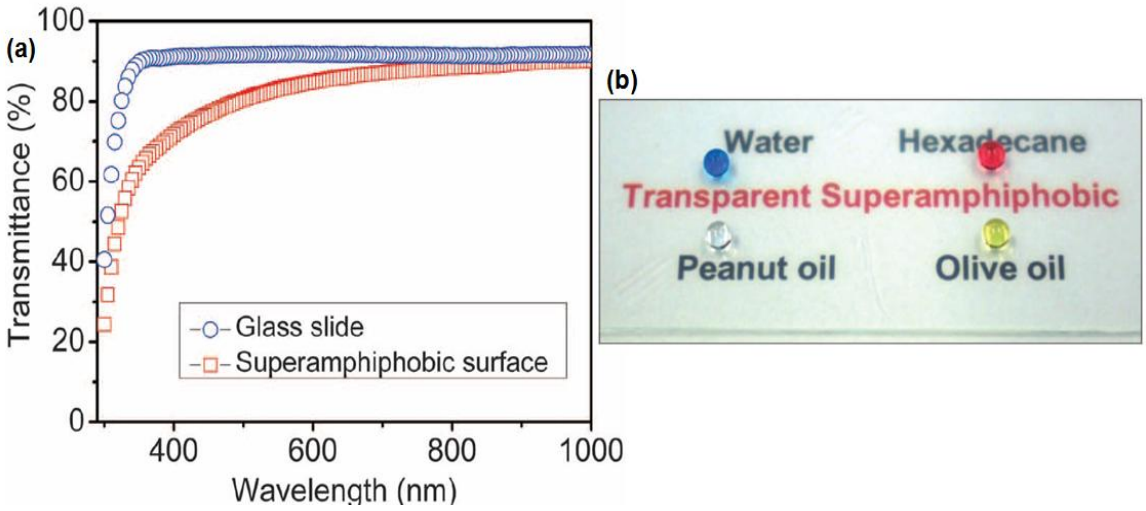

3.5 – Transmittance spectrum of a 3 µm superamphiphobic film compared to a pristine glass slide (a). The same glass slide exhibits self-cleaning behavior down to surface tensions of 27.5 dyn/cm (hexadecane)[78].

3.3. Experimental Methods

3.3.1. **Synthesis of Fluorinated Graphene Oxides**

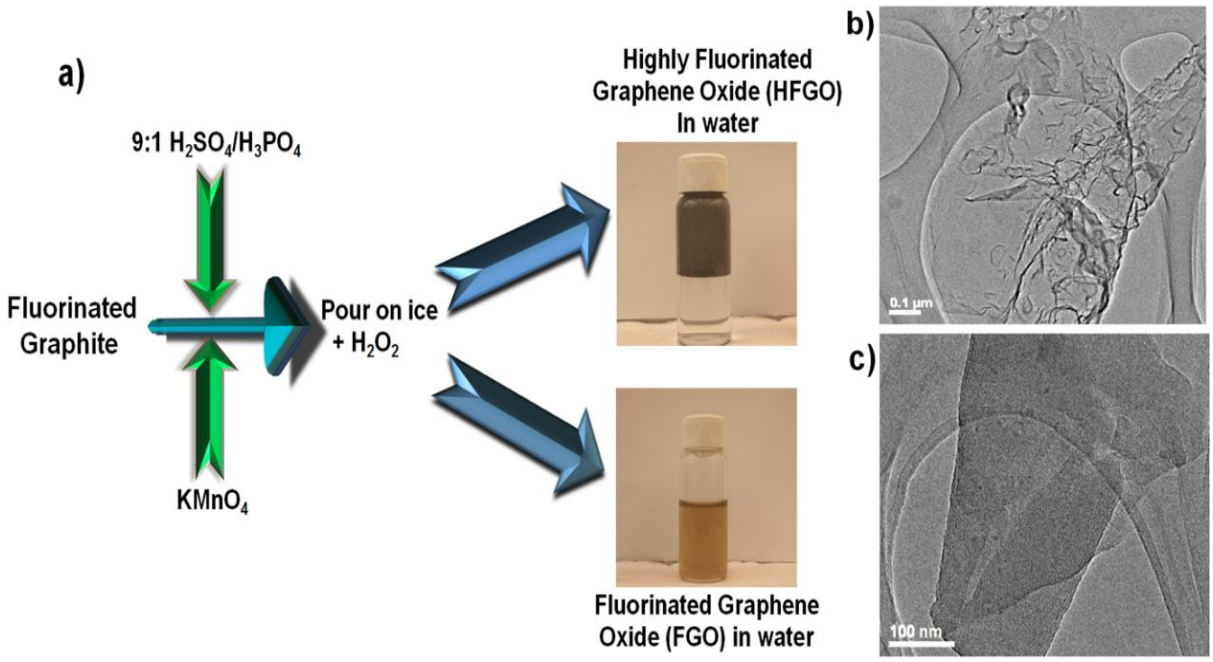

Figure 3.6 - A schematic showing the involved to synthesize FGO and HFGO (a). Upon oxidation, two distinct solid phases are observed, one of which forms a homogeneous, light-brown suspension in water, while the other rests on top, as demonstrated in the photograph. TEM images of FGO (b) and HFGO (c) show sheeted structures, with both nanomaterials existing as 2D nanoflakes upon exfoliation, having defined geometries on the basal plane and edges. XRD (d) shows a considerable increase in interplanar spacing, almost identical to that of GO, after oxidation, while Raman spectra (e) show a much more restored sp^2 lattice[85].

4 g of fluorinated graphite polymer (Alfa Aesar, 42537) was dispersed in a 9:1 mixture of H_2SO_4:H_3PO_4 and stirred at 50°C for 2 hours. 18 g of $KMnO_4$ (Aldrich) was then added to the mixture in parts. During $KMnO_4$ addition, a highly exothermic

reaction was observed along with an increase in temperature to 90°C, so it is critical that it is not added to the highly acidic solution in bulk. Upon addition of $KMnO_4$, the black acidic dispersion is seen to change to a dark brown color, after which the mixture is left to stir overnight at 90°C. The mixture is then poured over ice (~400 mL) and 10 mL H_2O_2, resulting in vigorous effervescence and a yellowish-brown color. Simultaneously, a fluffy dark brown solid phase precipitates out of solution to the top of the flask, while the lighter brown phase settles in solution. The two solids are then allowed to phase separate overnight. Drastic differences in the chemical composition and thus the wetting characteristics of the two phases results in no mixing. The experiment was repeated over 10 times, and each time 2 distinct phases were obtained.

The top phase (HFGO) was then scooped out of solution, along with most of the acid-water mixture and filtered out with an Omnipore membrane. The bottom phase (FGO) was also simply filtered out with a Durapore (0.1 μm) membrane. The mechanism for synthesis and phase separation can be proposed as follows: the harsh acid treatment and subsequent oxidation result in the immediate, complete oxidation and exfoliation of surface layers of the planar, hexagonal fluorinated graphite (FG). FG contains both semi-ionic and covalent C-F bonds. The semi-ionic bonds can be easily removed by this treatment due to which, one part of FG gets completely oxidized and settles in solution. The other phase remains hydrophobic even after exfoliation due to the high content of polar C-F bonds. Both phases were then dispersed in appropriate solvents (FGO in water and HFGO in

Tetrahydrofuran) and centrifuged (6000 rpm, 2 hrs) after which they are isolated and washed with 200 ml of 30 wt% HCl, 200 mL ethanol and soaked in diethyl ether. In appearance, FGO is a light brown powder which forms homogeneous colloidal suspensions in water, while HFGO has a light gray color and repels water.

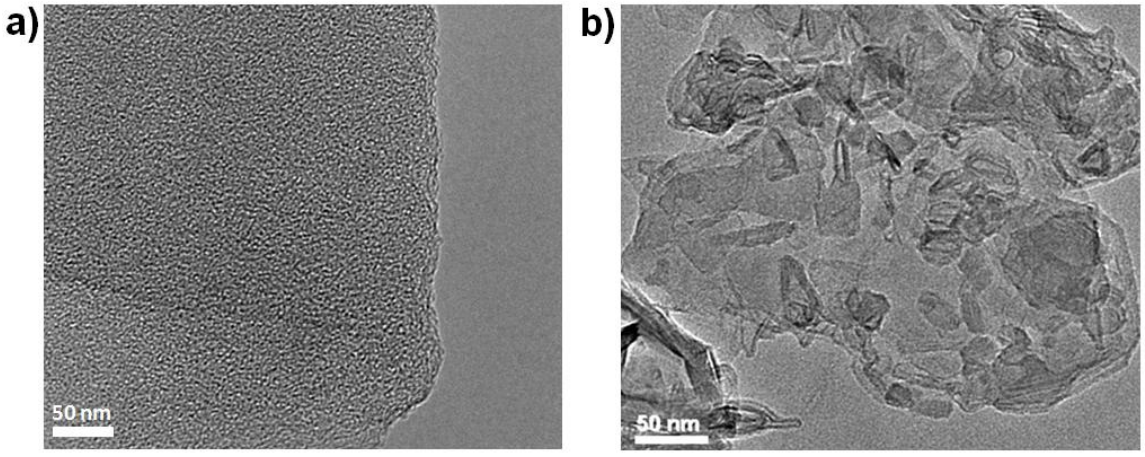

Figure 3.7 – Additional TEM images of few-layered HFGO (a) and FGO (b).

3.3.2. **Characterization**

FTIR analysis was conducted in attenuated total reflectance (ATR) mode on a Nicolet FTIR microscope with a MCT/A detector. XPS analysis was done on a PHI Quantera X-ray photoluminescence spectrometer, at a chamber pressure of 5×10^{-9} torr and Al cathode as the x-ray source, with power set to 100 W and the pass energy for the survey scan was 140.00 eV. MAS ^{13}C NMR spectra were obtained on a Bruker Avance III spectrometer (200.13 MHz ^{1}H frequency, 50.33 MHz ^{13}C frequency). Parameters for Figure 3.13 (c) , (d) - 4mm rotor spinning at 15.0 kHz (so that any spinning sidebands are multiples of + or -298 ppm from a centerband),

90° ^{13}C pulse, 20.5-ms FID with ^{1}H decoupling, 40-s relaxation delay and 12,360 scans. Chemical shifts relative to glycine carbonyl defined as 176.46 ppm[86]. A preliminary spectrum of FGO obtained with only a 20-s relaxation delay was very similar to that obtained with a 40-s relaxation delay. A cubic spline baseline correction (standard Bruker software) was applied to remove baseline curvature. X-ray diffraction studies were conducted on the powder samples using a Rigaku Cu Kα radiation (λ=1.5418Å), with a graphite monochrometer, and scintillation counter detector. Raman studies were conducted using a 633 nm laser excitation. A JEM-2100F Field Emission Electron Microscope featuring ultrahigh resolution and rapid data acquisition was used for taking TEM images.

3.3.3. **Calculating surface tensions of water-MEA mixtures**

In order to obtain a lower-limit on the extent of amphiphobicity, the surface tension of water-MEA mixtures was calculated. MEA is an important solvent in the refining industry as it is used for removal of CO_2 and H_2S from flue gas. Vazquez *et al.* have measured the surface tensions of water + methanolamine binary mixtures between 25°C to 50°C for varying mass fractions of MEA[87], while the temperature control precision is reported at $\pm$0.5 deg and surface tension at $\pm$0.02 mN/m. . The surface tension is measured at 5° intervals using a Traube stalagmometer and a Prolabo tensiometer, the experimental procedure of which has been described elsewhere[88]. The results are presented in Figure 3.8 on the following page.

Table 1. Surface Tension (σ/mN m^{-1}) of Monoethanolamine (A) + Water (B)

	t/°C				
x_A	25	30	35	40	45
0.000	72.01	71.21	70.42	69.52	68.84
0.015	68.45	67.66	66.86	65.99	65.32
0.032	65.97	65.17	64.41	63.50	62.83
0.049	64.09	63.29	62.51	61.63	60.96
0.069	62.63	61.84	51.06	60.17	59.49
0.112	60.41	59.61	58.84	57.94	57.27
0.164	58.74	57.94	57.15	56.27	55.58
0.228	57.31	56.52	55.74	54.84	54.16
0.307	55.99	55.20	54.43	53.52	52.84
0.407	54.66	53.86	53.07	52.18	51.49
0.541	53.18	52.37	51.58	50.69	50.00
0.726	51.38	50.57	49.77	48.88	48.18
1.000	48.95	48.14	47.34	46.43	45.73

MEA Concentration (wt %)

Figure 3.8 – Surface tension data for MEA-Water binary mixtures from 25°C to 50°C[87] .

For a given temperature, the surface tension of a binary MEA-water mixture was seen to decrease with an increase in the MEA concentration. This trend was observed to be non-linear, with the magnitude of surface tension decrease being larger at low concentrations than at higher concentrations. Vazquez *et al.* fit the following equation to each data point as a mathematical relation:

$$\frac{\sigma_w - \sigma}{\sigma_w - \sigma_A} = \left(1 + \frac{a x_w}{1 - b x_w}\right) x_a$$

Equation 3.5 – Mathematical relation to calculate the surface tension of water-MEA binary mixtures[88]

Where σ is surface tension (w: pure water; a: pure methanolamine;) and x represents their *mole* fraction respectively. The authors have calculated the parameters a and b, which for MEA at 25^{o}C, are 0.6272 and 0.9465 respectively [88].

3.3.4. **Fabricating inks & spray-painting methodology**

HFGO inks were prepared between concentrations of 2 – 4 mg/ml. The inks were initially bath sonicated for 2 hours, followed by 4 minutes of tip sonication. The airbrush spray-paint gun deposited 2 μL per 'run', and a minimum of 3 runs were necessary to form a pinhole-free film. The morphology of spray painted substrates was examined under a scanning electron microscope (SEM) using a FEI Quanta 400 a high resolution field emission SEM.

Figure 3.9 - The airbrush spray gun used for imparting HFGO inks onto the desired porous/non-porous substrates.

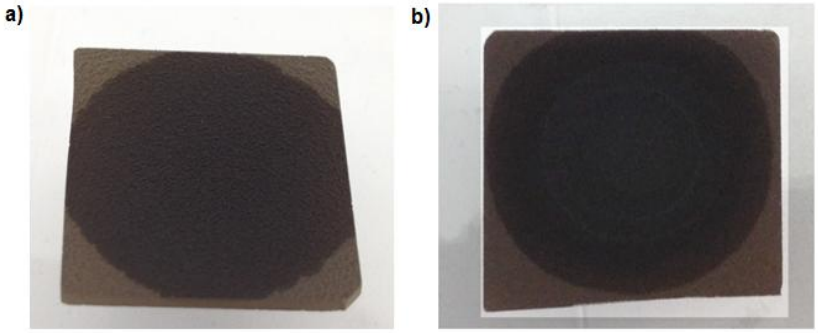

Figure 3.10 – Spray-painted films of FGO (a) and graphite oxide (b). FGO exhibits superhydrophilic characteristics similar to GO and water droplets immediately wet the surface.

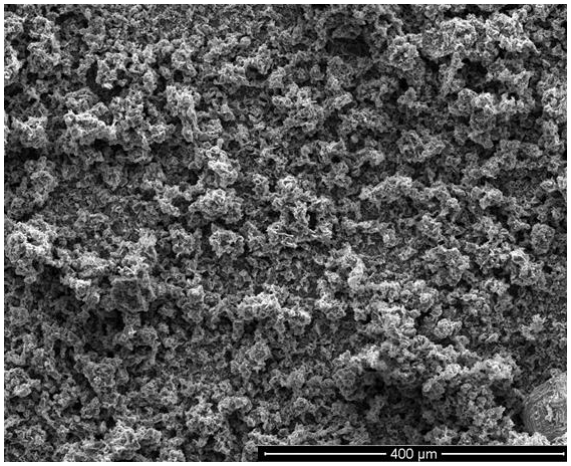

Figure 3.11 – SEM of spray-painted HFGO on silica substrate. A pinhole-free film is observed.

3.4. Results & Discussion

3.4.1. **Characterization & Nomenclature**

The risk posed by synthetic routes to fluorinate graphite, as discussed in Section 3.2, call for finding an alternative means which can be consistently reproduced on a lab-scale. The route adopted, as shown in Figure 3.6, starts with a fluorinated precursor, which is then oxidized heavily in accordance with classical oxidation techniques for GO. The raw material, fluorinated graphite polymer (FG), has the chemical formula $(CF_{0.25})_n$ and consists of cross-linked fluoroaliphatic monomers assembled into a 1-D polymer strand with both C-C and C-F bonds. The first mention of such materials was made by Ishikawa *et al.* in the 1970s[86]. These are significantly different from flouro-organic aliphatic and/or aromatic polymers, due to the presence of 2D and 3D structures within the monomer itself [89]. Upon reaction with H_2O_2, the originally black dispersion turns to a yellowish-brown color, indicating oxidation of the graphitic planes in the fluorinated graphite. At the same time, another dark-grey solid precipitates out of solution and settles on top of the acid-water mixture, as shown in Figure 3.6 (a). Such behavior is hypothesized due to major differences in chemical composition with the yellow-brown phase that forms stable colloidal dispersions in water. In terms of surface morphology, however, both phases exist in the form of 'flakes' or 'sheets' and the hexagonal lattice pattern is preserved on the basal plane and edges (Figure 3.6 (b) and (c)), with flake sizes between 500-800 nm which is within the same range as that of GO. X-ray diffraction

(XRD) confirms stacking of the nanosheets, while also giving insight into the order/disorder prior to and post-synthesis.

Since the first successful synthesis of C_4F ($CF_{0.25}$ or tetracarbon monoflouride) by *Rudorff et al.* several models have been proposed that suggest a layered structure of C_4F. Mitkin and coworkers [89] proposed a model containing regular distorted regions of graphitic sp^2 planes with three C-C sp^3 bonds, one covalent C-F sp^3 bond and structurally isolated hexagonal regions with conjugation of three C-C bonds. The XRD spectrum of pristine fluorinated graphite polymer, which also has the chemical formula $(CF_{0.25})_x$ exhibits a sharp graphitic peak at 26^o corresponding to the (002) plane of graphite while the remaining peaks are in agreement with those reported by Mitkin and DFT theory[72]. The XRD spectra of the exfoliated nanoflakes, which have previously not been studied, show unique features. The hydrophilic (yellow-brown) phase has a prominent peak at 10^o, which is also found in GO resulting from an increase in interlayer spacing from 3.3 A to 6 A due to functionalization of the basal plane. The remaining peaks are diminished, possibly due to the partial removal of other semi-ionic/covalent C-F bonds**.** Raman analysis gives an idea of the order and disorder, especially from the perspective of the graphitic lattice. In Figure 3.12 (b), FG does not show graphitic D or G peaks due to a highly distorted graphitic lattice, while the hydrophilic sample (FGO) shows both peaks, confirming the restoration of the graphitic lattice in it. The top (dark gray) phase also shows an XRD peak at 10^o, indicating functionalization and exfoliation in solution, while its Raman spectrum shows less intense D and G peaks corresponding to a sp^2 lattice

with slightly less order compared to the hydrophilic phase. Most significantly, however, our reaction scheme provides a route to synthesize ordered nanoflakes from a highly distorted raw material.

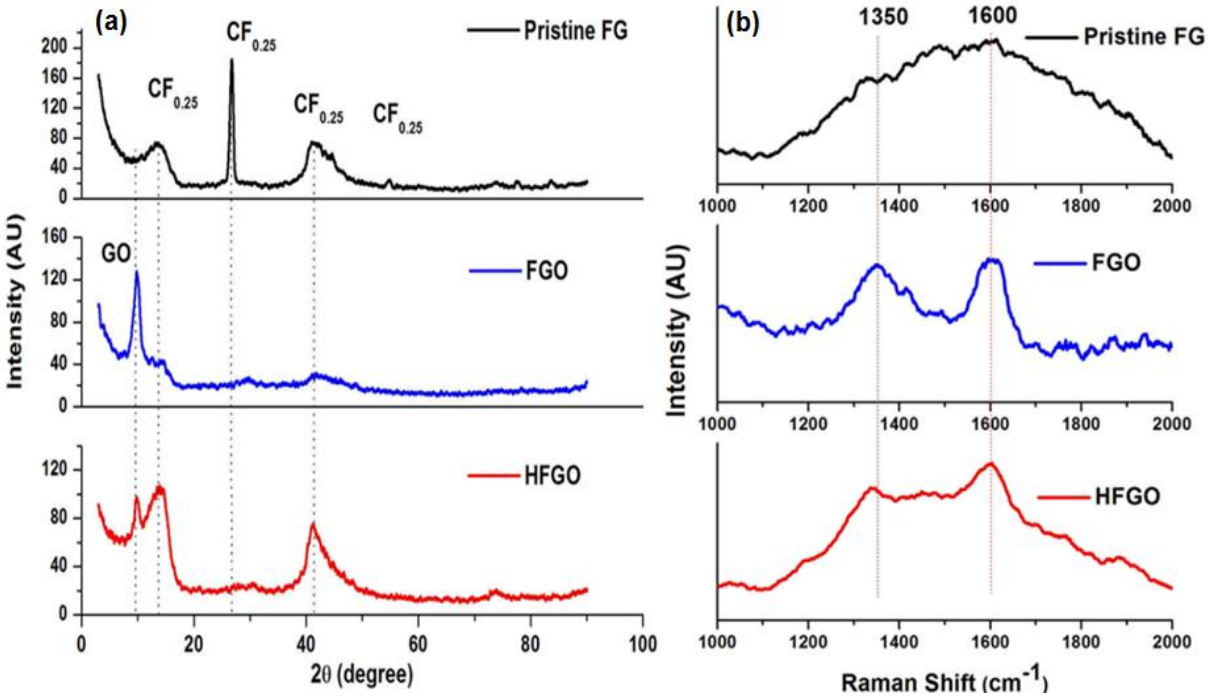

Figure 3.12- XRD (a) shows a considerable increase in interplanar spacing, almost identical to that of GO, after oxidation, while Raman spectra b) show a much more restored sp^2 lattice.

Magic angle spinning (MAS) ^{13}C NMR serves as a powerful tool to provide a closer look at the chemical composition of each phase. The MAS ^{13}C NMR spectrum of the bottom phase (Figure 3.13 a) is almost identical to that of GO, with the exception of a distinctive signal at 88 ppm that does not appear in the spectrum of GO[9]. A signal at 88 ppm is consistent with a tertiary alkyl fluoride environment, as opposed to a secondary, primary alkyl fluoride, or an aromatic fluoride, all of which

would display significantly more deshielded ^{13}C signals for the C-F bond that would be obscured by other signals[90]. The other signals are typical of the epoxide, alcohol, alkene, aromatic and carbonyl functional groups in GO[9]. The relative signal intensities are believed to be meaningful, as a preliminary spectrum obtained with a shorter relaxation delay is similar (details in Section 3.2). Since we are able to synthesize exfoliated nanoflakes of graphene oxide with tertiary alkyl fluorides covalently attached to the basal plane, we choose to entitle the bottom phase *fluorinated graphene oxide (FGO).* The signal at 88 ppm dominates the spectrum of the top phase (Figure 3. 13 b) while still showing the presence of epoxy, alcohol, and aromatic peaks. On the other hand, there is no detectable carbonyl intensity in the sample. Intuitively, the top phase is entitled *highly fluorinated graphene oxide (HFGO)*. The relative abundance of each organic moiety, in particular the aliphatic C-F, is different in each structure, thus the nomenclature.

The ability of MAS at 15 kHz to effectively eliminate ^{13}C-^{19}F dipole-dipole broadening has been demonstrated in work on fluorinated carbon nanotubes[90]. High power ^{1}H decoupling is still used to eliminate ^{13}C-^{1}H dipole-dipole broadening. The reasons for the absence of any detectable scalar ^{13}C-^{19}F coupling in the MAS ^{13}C NMR spectra of FGO and HFGO are the same as in the MAS ^{13}C NMR spectra of fluorinated carbon nanotubes.

In addition to XRD and Raman data, the tuning and matching characteristics of the NMR probe with FGO and HFGO provide another indication of the relative amount of structural alteration of the graphitic plane of the FG precursor. While FGO

exhibits a modest change in probe tuning and matching for both the ^{13}C and ^{1}H channels compared to glycine, HFGO exhibits almost no change, i.e., even more extensive functionalization of the graphitic plane has occurred. Fluorinated graphite (FG) is conductive. A useful MAS ^{13}C NMR spectrum could not be obtained from FG dispersed in silica (10:90 w/w), which is consistent with previous reports[89].

ATR-FTIR spectra of both FGO and HFGO confirm the presence of the moieties identified by ^{13}C NMR. The sharp peaks at 1208 cm^{-1} in both spectra (Figures 3.13 c, d) are due to stretching vibrations of the C-F bond from tertiary sp^3 carbons. Representative structures for each phase can then be formulated, as shown in Figures 3.14 (a) and (b), both of which are essentially modifications of the original GO structure. FGO consists of a graphene basal plane with tertiary alkyl fluorides in addition to epoxy, carbonyl and hydroxyl functionalities. HFGO also has a graphene basal plane with a greater amount of tertiary alkyl fluorides. The presence of carbonyl groups is believed to be very minimal, since only a low intensity peak was noted in FTIR. Both epoxy and alcohol functional groups are present but are much lesser in abundance relative to those in FGO.

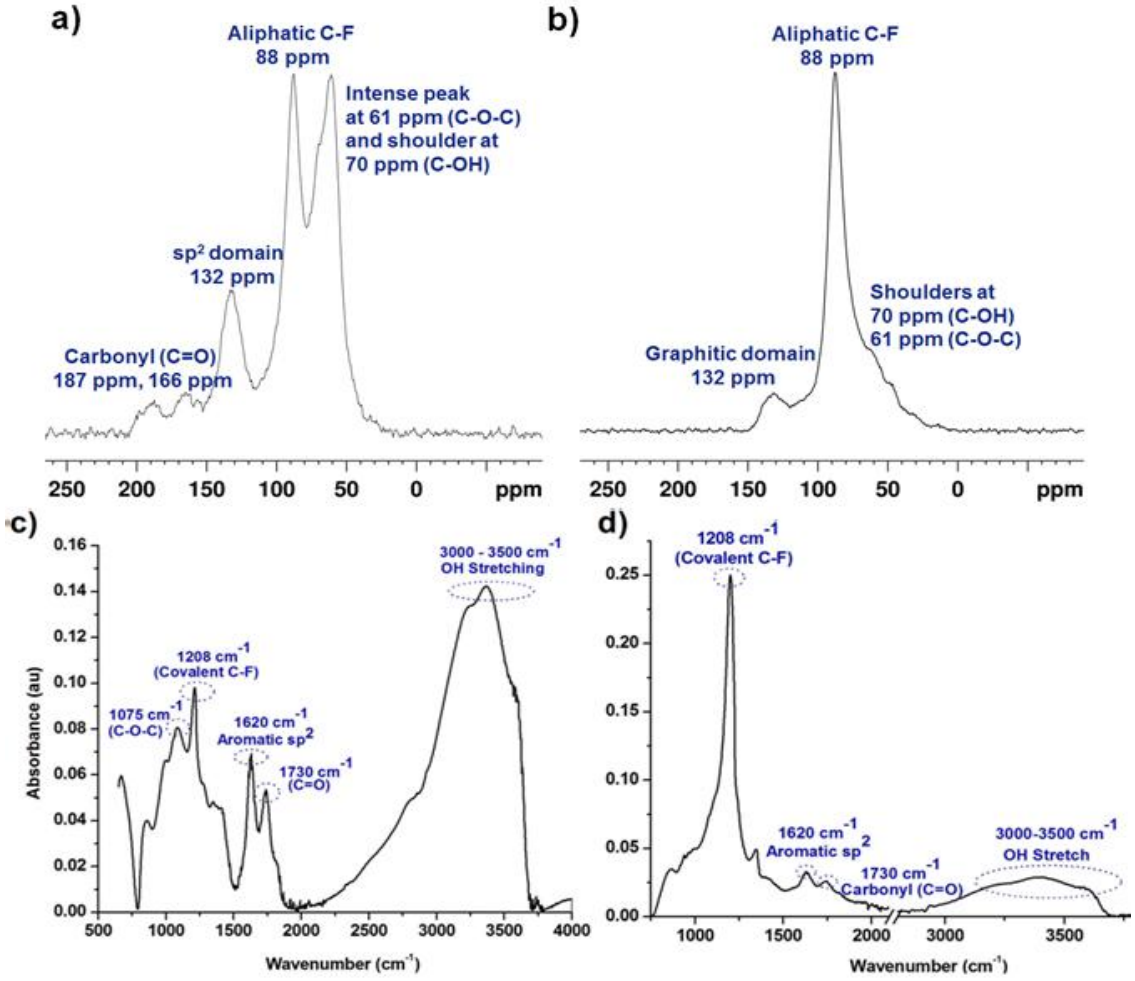

Figure 3.13 - 50.3 MHz ^{13}C MAS NMR spectra of (a) FGO and (b) HFGO. Both spectra show a signal at 88 ppm due to the presence of tertiary alkyl fluorides. ATR-FTIR of FGO (c) is identical to GO[1] with a sharp peak at 1208 cm^{-1} indicating the presence of covalent C-F bonds, while the remaining peaks have been accounted for in previous literature. HFGO shows the same peak at a considerably greater intensity (d) and confirms an aromatic domain (1620 cm^{-1}) with other organic moieties. Additional experimental parameters have been listed in Section 3.3.2.

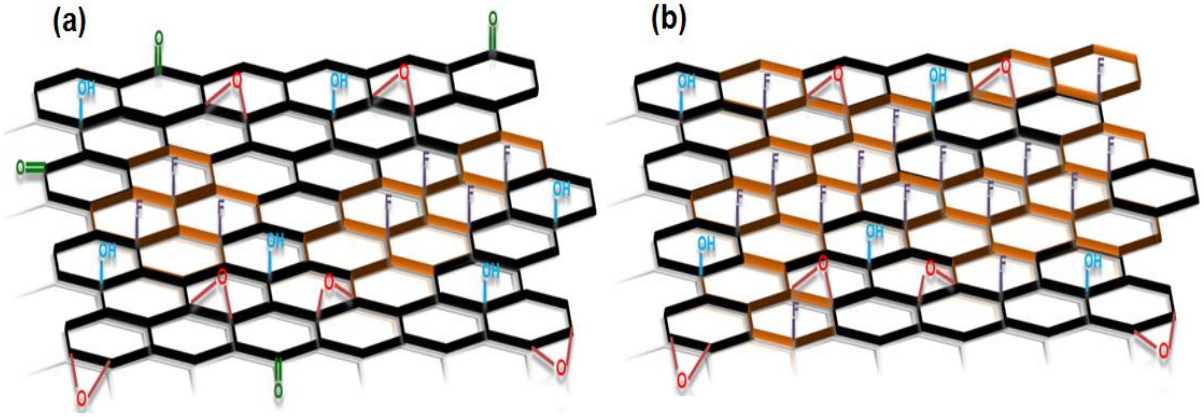

Figure 3.14 – Based on characterization, the following structures for FGO (a) and HFGO (b) are proposed. Both nanoflakes have graphitic domain with aliphatic tertiary fluorides covalentyl bonded. HFGO does not have carbonyl bonds (C=O) and a greater % of C-F bonds compared to FGO.

Deconvolution of the C 1s peak in HFGO (Figure 3.15 a) shows a C-F peak [91] with greater intensity than that in FGO (Figure 3.15 b), indicating a *much* higher % of fluorine in HFGO. Atomic % of C, F and O shown in Table 3.1 explain the vast difference in wetting characteristics of the two compounds, and also why FGO is similar to GO in terms of wetting characteristics (i.e. forming stable colloidal dispersions in water). From a structural point of view, this is also in agreement with FTIR and NMR data, both of which point towards similar structures for both FGO and HFGO with the latter having a *significantly* higher abundance of fluorine.

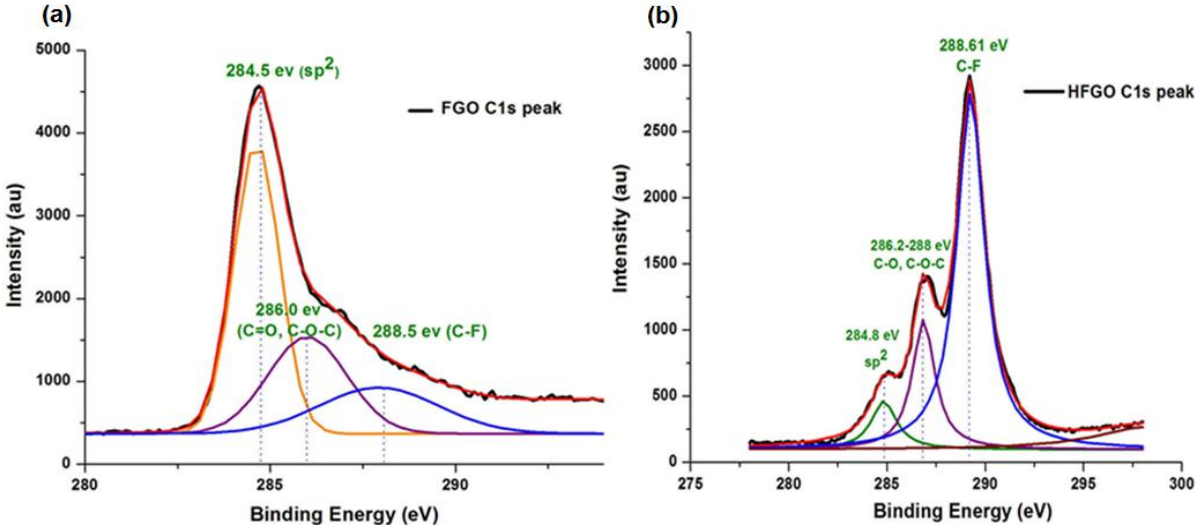

Figure 3.15- Deconvoluted XPS spectra of FGO and HFGO. FGO (a) shows a well-defined sp^2 domain with organic functional groups that are also confirmed by Figure 2. There is also a C-F peak. The C 1s peak of HFGO (b) shows the same functionalities and a defined sp^2 domain, with a considerably sharper C-F peak on a relatively well-defined sp^2 domain.

Compound	C (%)	O (%)	F (%)
Fluorinated Graphene Oxide (FGO)	76.60	17.80	5.60
Highly Fluorinated Graphene Oxide (HFGO)	64.61	11.45	23.00
Graphite Oxide (GO)	65.2	34.71	0

Table 3.1 – Atomic percentages of C,F and O in GO, FGO and HFGO. Fluorinated graphite (FG) has 27% fluorine, and a chemical formula of $(CF_{0.25})_n$

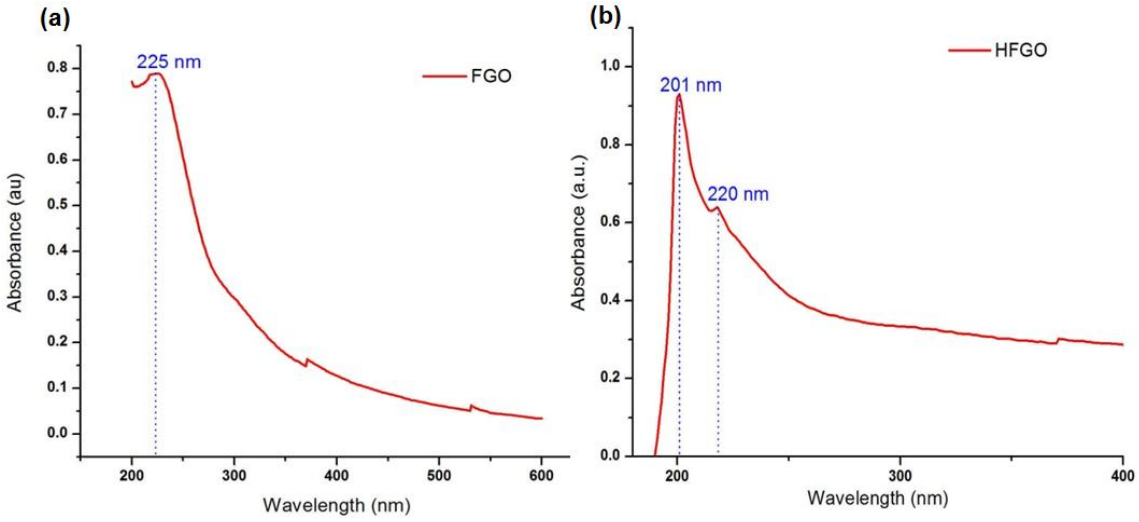

Figure 3.16 – UV-Vis absorption spectra of FGO (a) and HFGO (b)

Both FGO and HFGO showed well-defined absorption peaks in Figure 3.16. The absorption spectrum of FGO is almost identical to GO, showing a peak at 225 nm[16] corresponding to the $\pi \rightarrow \pi^*$ transition and a slight shoulder at ~300 nm due to the $n \rightarrow \pi^*$ transition of the carbonyl bonds[2]. HFGO shows no such shoulder at 300 nm, while showing a slightly less intense peak at 220 nm.

3.4.2. **Superamphiphobic Graphene-Based Inks**

A direct application of fluorinating GO arises from the low surface energy of the C-F bond, which is responsible for the superhydrophobicity of HFGO. Quantitatively, this can be understood by Young's equation (Equation 3.1). With the surface tension of the liquid being a constant, the only manipulable parameter is the surface energy of the solid surface (γ_{sl}). Minimizing the surface free energy leads to the highest possible contact angle, depending on the surface tension of the liquid. Films of both FGO and HFGO displayed considerable variation in their wetting

characteristics; a drop of deionized water shows a contact angle on the order of 150^{o} on HFGO, while a FGO film was considerably superhydrophilic as the droplet immediately wet the surface (Figure 3.10), similar to GO[20]. The variation in contact angles is directly related to the chemical environment and polarity of each sample. In FGO, while C-F bonds are present in relatively low abundance, the high abundance of the polar hydroxyl, carbonyl and carboxylic acid moieties results in electrostatic repulsion in solution, as previously noted by *Gilje et al.* similar to that in GO, leading to the formation of stable colloidal suspensions in water[50]. The surface free energy of the solid is still slightly reduced due to the presence of tertiary alkyl fluorides on GO, but the decrease is not of a considerable magnitude to affect wetting. From a quantitative perspective, the organic functionalities clearly outnumber the tertiary alkyl fluorides so there is no drastic variation in the wetting behavior between GO and FGO (see Experimental Methods, Figure 3.10). On the other hand, HFGO, which has a much greater % of C-F bonds demonstrated outstanding superhydrophobicity, something that has previously not been reported with graphene oxide-based materials. This represents a sizeable reduction in the surface energy of GO due an increase in the C-F bonds on the surface. While a number of other materials show similar outstanding superhydrophobicity, it is the ease of solution processing that makes HFGO a superior candidate. The pursuit for fabricating surfaces that repel both water and organic solvents (i.e., those that have surface tensions lower than water) has led to some prominent, breakthrough reports[69], [78] These studies, however, require exclusive infrastructure

(lithography, CVD), high temperature processing (i.e. silanization at 600^{o}C) and restrict the type of substrates they can be coated on. This limits the *accessibility* of the coating, which is vital. Other reports that rely on vacuum filtration[76] amplify this dilemma since the ability to manipulate the size and substrate is limited to a great extent by the diameter of the filter paper and scaling up is unattainable.

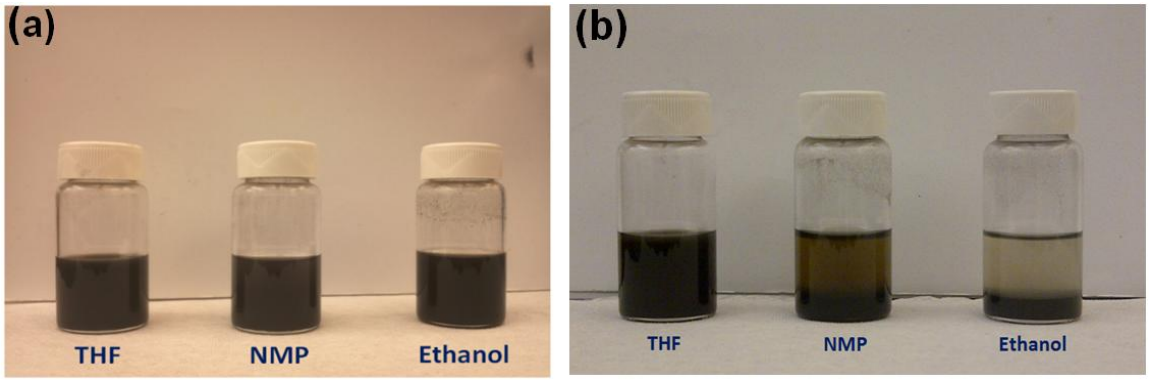

Figure 3.17 – Inks of HFGO were prepared (a) in THF, NMP and Ethanol. After bath sonication, inks were left for 1 hour at room temperature, and THF showed best stability (b).

The simplicity associated with the solution processing of HFGO permitted fabrication of 'inks' that were sprayed on a range of substrates using an airbrush spray-gun. The spray-painted films are between hundreds of nanometers to a few microns in thickness and maintain the superhydrophobic standards displayed by vacuum-filtered HFGO films. Inks were created in a number of organic solvents (Figure 3.17 (a)) with the main criteria being to identify a (i) solvent with a low boiling point and (ii) a solvent which forms a stable solution of HFGO. Inks were sonicated and left to stabilize for an hour, after which THF showed the best stability

(Figure 3.17 b). Its low boiling point (66^{o}C) enabled spray-painting at room temperature without the need to heat the substrate for enhanced evaporation. Upon spraying 1.2 mL of HFGO ink, the wetting behavior of a steel disc was greatly affected (Figure 3.18(b)) with water showing a contact angle of 151^{o}. Monoethanolamine (MEA, 30 wt%), which has a surface tension of 59 dyn/cm and is an essential solvent during CO_2 adsorption processes[87] was also 'repelled' from the surface (Figure 3.18 (b), light pink liquid droplets), showing a contact angle of 145^{o} (Figure 3.18 (a)).

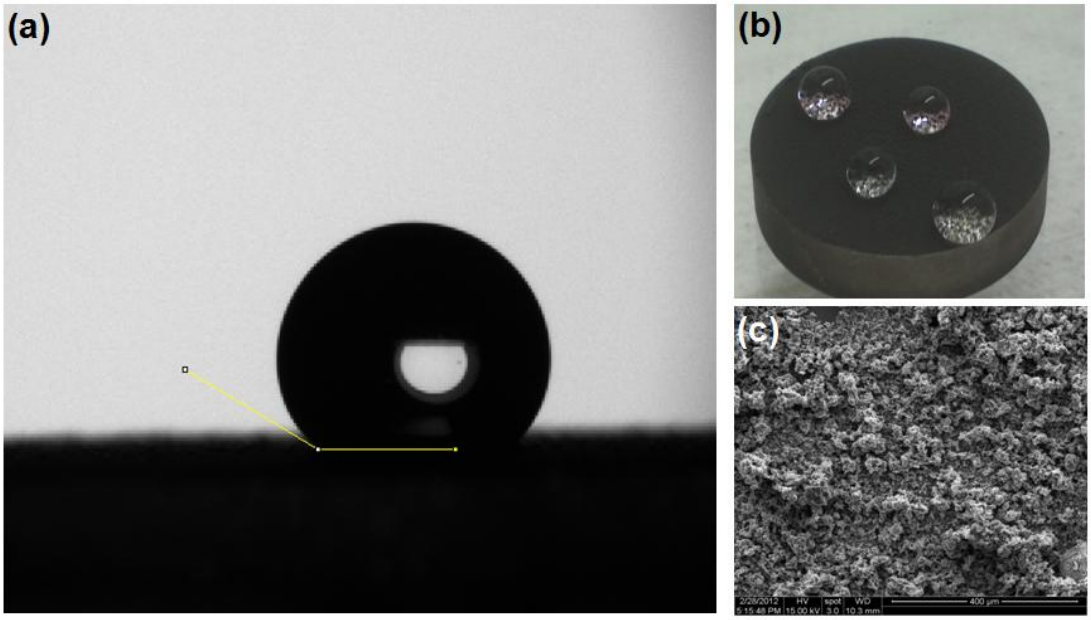

Figure 3.18 - With 30 wt% monoethanolamine, HFGO shows a contact angle of 145^{o} (a). HFGO inks were sprayed on steel discs, and both superhydrophobicity (colorless DI water) and amphiphobicity (light pink MEA) were demonstrated (b). SEM of spray-painted HFGO shows a pinhole-free surface.

Such “amphiphobic” behavior of functionalized graphene oxide has not been previously reported. SEM images of sprayed surfaces (Figure 3.18 (c)) indicate the formation of a uniform coating. The coating thickness can also be modulated by viscosity/concentration of the ink and air pressure during spraying. Amphiphobic, spray-paintable inks can also be extended to non-porous substrates of varying geometries. The pinhole-free nature of the films was taken advantage of by spraying HFGO inks on paper towels, which are exceptionally porous (Figure 3.19 (b)). Droplets of both MEA (pink) and water were repelled from the now amphiphobic paper towel. HFGO inks were also spray-painted onto fabrics, which are innately amphiphilic (Figure 3.19 (b)) but upon spray-painting, demonstrate outstanding amphiphobicity (Figure 3.19 (c)). Such ‘self-cleaning’ fabrics have always held great value, and the inexpensive nature of this methodology for HFGO synthesis, along with the ability to “coat” virtually any surface and geometry, makes it directly applicable in the textile industry due to resistance to soiling.

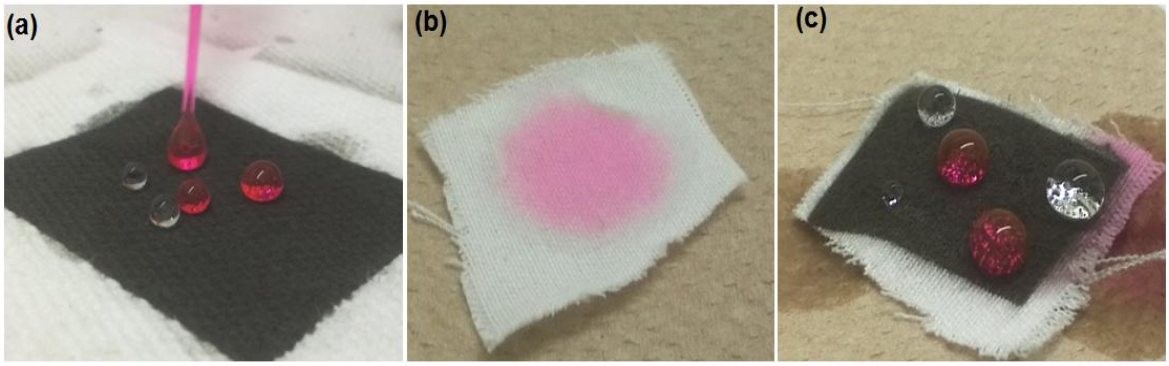

Figure 3.19 – HFGO inks maintained self-cleaning behavior on porous substrates as well. Shown are a paper towel (a) and fabric (c). The same piece of fabric is wetted by MEA before treatment (b).

To gauge the surface free energy of spray-painted HFGO, several contact angles at progressively decreasing surface tensions were measured. As shown in Figure 3.20, amphiphobic behavior was maintained up to a surface tension of 58.7 dyn/cm (135°), after which contact angles decreased to 92.5°, which is categorized as amphiphobic. The need for rigorous, time-consuming methods that are currently being implemented for fabricating self-cleaning amphiphobic surfaces is thus very close to being eliminated. Moreover, incorporating CF_2/CF_3 groups on the FGO surface by substitution reactions, particularly with carbonyl/ketone moieties would extend superamphiphobicity down to solvents with ~20 dyn/cm and is another immediate challenge posed by the current study.

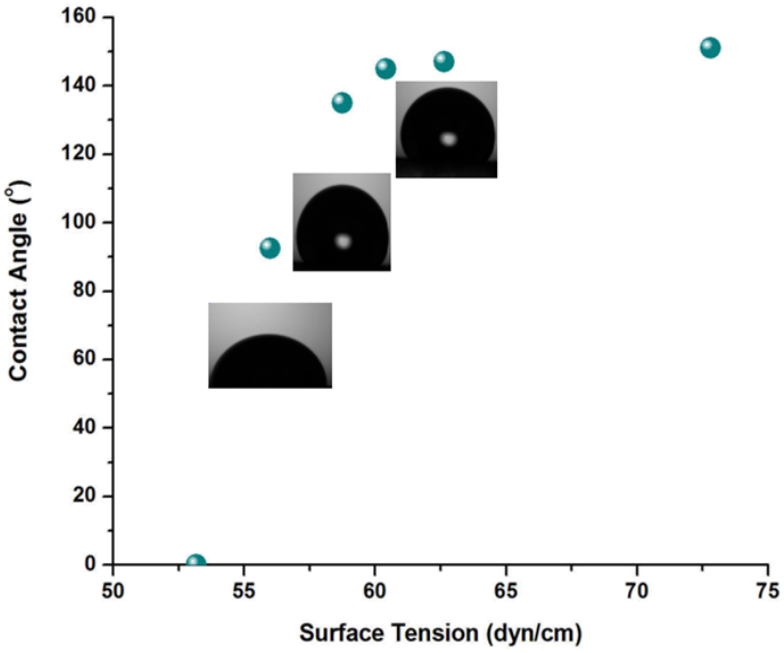

Figure 3.20 – A summary of behavior of spray-painted HFGO filns on glass, showing a limit of just below 60 dyn/cm, after which superamphiphobicity is no longer demonstrated.

3.5. Concluding Remarks & Future Direction

This chapter reports a chemical scheme to synthesize nanoflakes of graphene oxide with fluorine atoms covalently attached to the graphitic basal plane. MAS ^{13}C NMR confirms the presence of fluorine in the form of tertiary alkyl fluorides, while additional characterization techniques provide further details about the two forms of fluorinated graphene oxide. Accordingly, structures for fluorinated graphene oxide (FGO) and highly fluorinated graphene oxide (HFGO) are proposed.

The hypothesis of reducing the overall free energy of a surface by introducing C-F bonds is then tested. The outstanding solution processability of GO enables the fabrication of amphiphobic inks that can be sprayed on to virtually *any* surface to repel water and organic solvents. The lower limit of amphiphobicity, obtained by equating the mass fraction of monoethanolamine (MEA) with tabulated data of water-MEA binary mixtures, was calculated to be 58.7 dyn/cm. The inexpensive nature of the proposed synthesis methodology and the potential for applications in both the oil and textile industries augment the value of fluorinated graphene oxide, while spray-painting doesn't restrict the accessible geometries. Thus in addition to exceptional electronic and energy[47], [63], [92] storage properties, we introduce graphene-based materials into the field of amphiphobicity**.** A facile, bulk synthetic method to fluorinate the graphene basal plane using wet chemistry has previously not been reported, and FGO has a number of direct applications in related fields: the presence of fluorine on the surface of GO has a direct effect on its electrical properties, which affects its behavior as a dual

electrolyte/electrode separator in supercapacitors [93]. Since both HFGO and FGO readily exfoliate in solution, wet chemistry reduction methods provide a means to realize a *chemical* route to fluorographene, a highly intriguing material, which still lacks a synthetic scheme.

Looking ahead, the work presented in this chapter has scope for improvement, and has laid groundwork for further research in fluorination of GO. Firstly, by choosing to oxidize a fluorinated precursor, one is limited by the raw material. Instead, realizing a chemical method to directly fluorinated GO itself, by taking advantage of its oxygen-rich basal plane has considerably greater value. Secondly, the adhesion of pristine HFGO, especially on smoother substrates such as steel and glass is relatively poor compared to conventionally superhydrophobic polymeric materials (i.e. PTFE). Both of these issues are addressed in chapter 5, as part of further work that has stemmed from this chapter.

Chapter 4

Creating Supersolvophobic Nanocomposites

This work presented in this chapter is the result of a collaborative project with ConocoPhillips (COP) in 2011. The objective was to leverage the carbon nanomaterial expertise at the Ajayan research group and introduce novel, functionalized nanomaterials into existing COP technologies, particularly polymeric films. In terms of functionalization chemistry, this problem was approached similar to the previous chapter. However, with scale-up concerns being a direct consequence, the issues encountered were very different from previous studies. Lastly unlike the previous two chapters, the material in focus in this chapter is carbon nanotubes (CNTs), which pose different challenges when it comes to solution processing.

4.1. General Introduction & Motivation

Altering the surface properties of polymeric films and achieving chemical control during processing enhances their value in a range of applications in the electronics and energy industries[94]. Carbon nanotubes (CNTs)[8], [95], [96] have always been an ideal candidate to enhance surface superhydrophobicity due to their inherent nanoscale roughness[74] which enables the formation of a composite solid-liquid-air interface. Correspondingly, the reduced free energy of this surface is responsible for a droplet of ionized water being repelled from it. Superhydrophobic behavior of CNTs has been extensively studied and documented in previous reports[74], [76],[97],[98].

However, when exposed to solvents with surface tensions much lower than that of water (72 dyn/cm) the "phobic" nature of CNTs diminishes as solvents readily penetrate their surface. In this chapter, the solvent of interest is 30 wt% monoethanolamine (MEA), a common solvent for CO_2 absorption in energy applications with a surface tension of 59 dyn/cm. MEA is representative of a number of solvents that are used for industrial CO_2 capture applications, and its behavior with CNTs has not been investigated before. The motivation behind this work is to chemically and/or physically tailor the surface characteristics of polymeric thin films to 'repel' 30 wt% MEA. Throughout this chapter, surfaces which give a contact angle of approximately 150^o with 30 wt% MEA and display low contact angle hysteresis are referred to as *supersolvophobic* surfaces.

Fluoro-functionalization of carbon nanomaterials is a technique that has previously been employed to reduce their free energy due to the low surface energy of the C-F and CF_2 bonds[69], [99]. With respect to graphene-based nanomaterials, Section 3.1 summarizes advances in this field, while Chapter 3 itself provides a route to synthesizing fluorinated graphene oxide, albeit from a fluorinated precursor. In terms of pristine CNTs, *Wang* et al. report their solubilization of in Nafion[100] to make solution processing much more accessible. *Luo* et al. show evidence of conductive CNT-polymer membranes produced by filtration which show outstanding superhydrophobicity due to similar fluorine-based chemistry[76]. However, filtration imposes a set of restrictions, such as the diameter and thickness of the filter paper and restricts the range of geometries. Furthermore, transferring superhydrophobic CNT coatings onto other surfaces is virtually impossible. Other studies reporting superhydrophobicity involve complex lithographic methods[81] that also limit the type of substrate and/or require use of harmful chemicals such as HF and XeF_2.

This work illustrates two techniques that enhance supersolvophobicity of inherently solvophilic polymeric thin films. The first technique involves creating a *perfluoro*-functionalized CNT-based "ink" that can be sprayed on any surface, including polymeric thin films to greatly enhance supersolvophobicity. Our results show contact angles greater than 150^o with 30 wt% MEA on films of polysulfone (PSF) and polyimide. The second method involves synthesizing a homogeneous, composite solution consisting of polymer (either PSF or polyimide) and perfluoro-

functionalized CNT (hereafter referred to as fCNTs). Drop-coated films from fCNT-polymer composite solutions ensure that supersolvophobicity is present within the nanocomposite thereby extending the proposed chemistry to a range of length scales. The ratio of polymer:fCNT was varied to identify an upper limit at which supersolvophobicity was maintained on the surface of the films. XPS and SEM confirm the presence of fCNTs within the polymer matrix that are responsible for the alteration in wetting behavior. As a control, PTFE-polymer composites were also fabricated compared to which fCNT-polymer composites exhibited superior supersolvophobicity at lower mass fractions due to their low density.

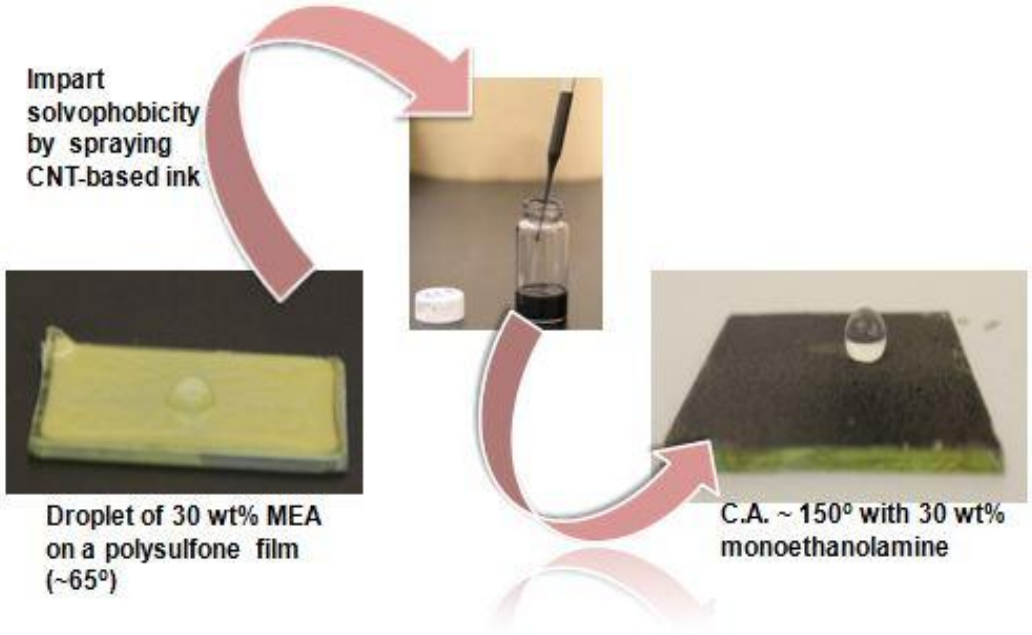

Figure 4.1 – Schematic showing a solvophilic polyimide film, which exhibits supersolvophobicity after fCNT ink is sprayed on its surface. The colorless liquid is 30 wt% monoethanolamine (MEA).

4.2. Introduction to carbon nanotubes (CNTs)

4.2.1. **Properties of CNTs**

Carbon nanotubes (CNTs) have attracted a significant amount of attention since 1991. Theoretically their structure was first hypothesized by Dresselhaus *et al.,* proposing a tubular carbon structure capped by fullerenes at either end[101][102]. Experimental evidence was first presented when Iijima *et al.* identified them as nanometer-sized 'needle-shaped tubes of carbon'[5]. Over the years, it's not only their unique geometry, but also their outstanding mechanical, electronic and chemical properties that have gained them enormous popularity[103]–[106]. These allotropes of carbon have a max length:diameter ratio of 1.32E08:1[107], a Young's modulus as high as 1-5 TPa, tensile strength of up to 100 GPa complimented by excellent hardness properties (withstand pressure up to 24 GPa without deformation)[108]–[110]. Electrical properties of CNTs show a major dependence on their structure. Depending on the *(n,m)* values of a particular carbon nanotube it could either show metallic or semiconducting properties[101], [111]–[113].

CNTs exist as either single-walled nanotubes (SWNTs), double-walled (DWNTs) or multi-walled (MWNTS) and are synthesized by a variety of techniques reported elsewhere[8], [114]. With regards to this thesis, the most significant of these is chemical vapor deposition (CVD). A typical CVD setup is shown in Figure 4.2, in which a hydrocarbon vapor is passed through a furnace, resembling a tubular reactor at elevated temperatures (~700^{o}C), which in turn results in CNT growth on

a catalyst surface, typically Al_2O_3 mixed with metal nanoparticles. CVD growth conditions have been optimized to control the length, diameter and chirality of synthesized CNTs[115], [116].

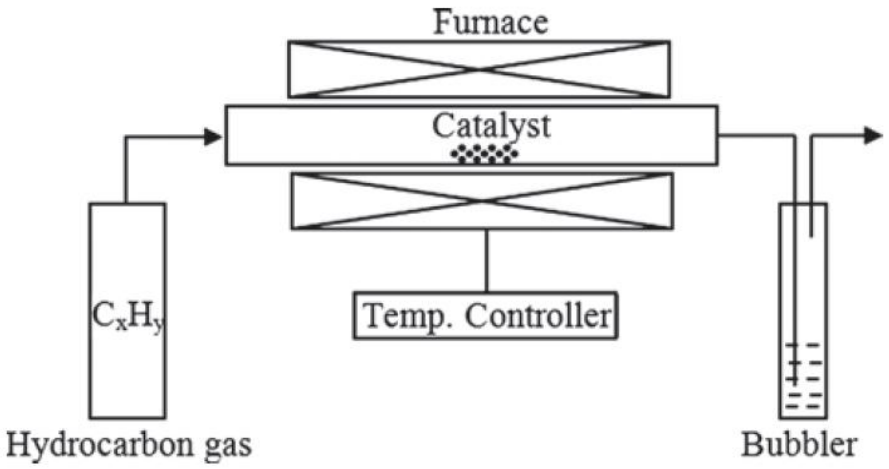

Figure 4.2 – A typical, simplified CVD setup for CNT growth.

4.2.2. **CNT-Polymer Nanocomposites**

Nanocomposites are defined as materials in which at least one phase has a physical dimension between 1-100 nm [117]. In terms of carbon materials, this nanoscale phase can either be 1-dimensional (i.e. CNTs), 2-dimensional (i.e. graphene) or 3-dimensional (i.e. an inter-connected porous network). While efforts in engineering are ongoing to create optimal nanocomposites, some of the best nanocomposites are seen in nature. For instance, osseous tissue (i.e. bone tissue) is in fact a composite material consisting of apatite nanocrystals (i.e. calcium hydroxylapatite) dispersed in a collagen matrix[118], [119]. While the osseous tissue contributes to bone rigidity the collagen provides elasticity. The idea of

implementing nano-sized additions to greatly expand the portfolio of properties that the material (i.e. the polymer) would never achieve by itself makes nanocomposite engineering a critical field, especially as substantial improvements are made to properties of nanomaterials themselves.

The key principle with implementing CNTs is to embed them homogeneously within lightweight polymer matrices. Experimentally, CNT-nanocomposites were first realized by Ajayan *et al.* in 1994[95], by cutting an epoxy/CNT composite to align CNTs within a matrix. In the years that followed, a great number of reports aiming to optimize mechanical and electrical properties have devised techniques to fabricate CNT-polymer composites of an assortment of architectures. However, as-grown CNTs are inhomogeneous, i.e. having different chiralities, defects and impurities and unequal lengths and diameters. More importantly, solution processing of CNTs is a major challenge as they are not stable in organic solvents, due to which increasing the volume fraction of CNTs in a composite becomes exponentially more difficult[120]. The criticality of surface functionalization and chemistry becomes evident in this case. Oxidation and further derivatization reactions have been one way to bypass such issues (Figure 4.3). Carboxylic acid (COO^-) groups on CNT sides make them susceptible to additional grafting reactions with polymers that have reactive end groups. Examples of such chemistry are ester and amide linkages. Other studies have also reported condensation, nucleophilic substitution and anionic polymerization of styrene onto CNTs[121], [122], [123], [124].

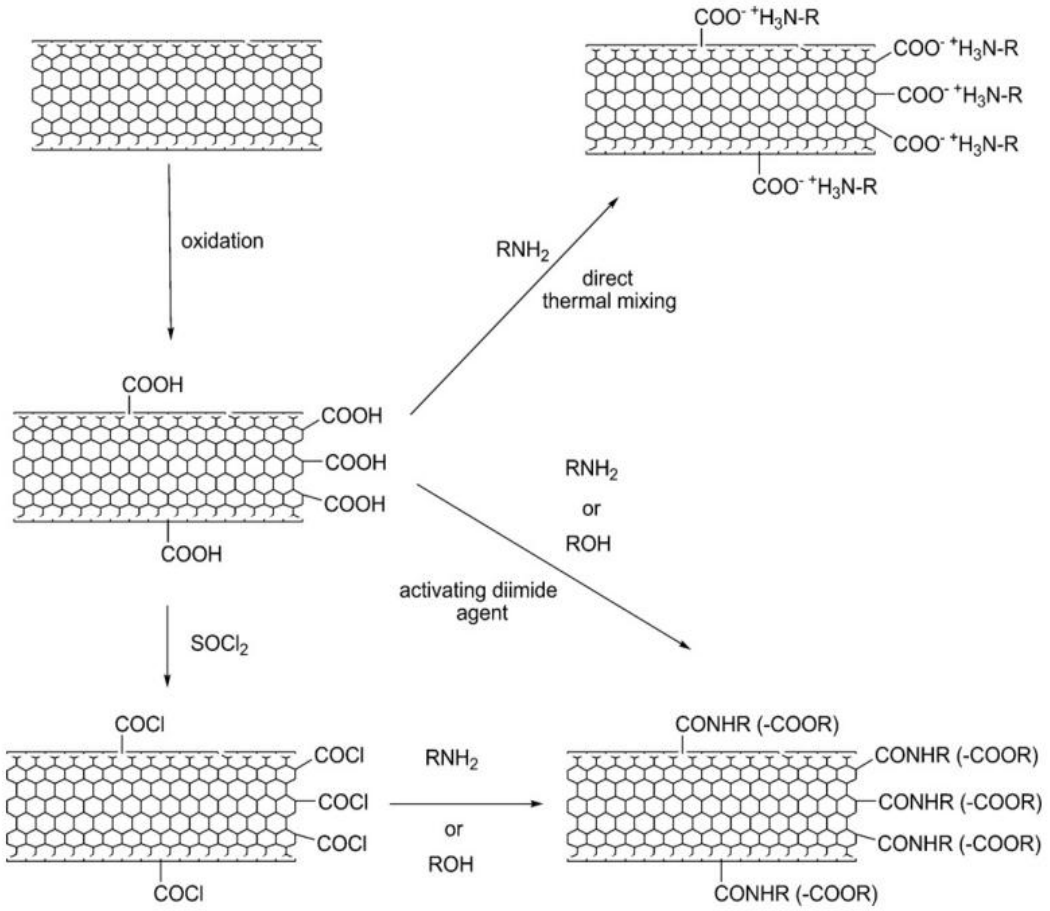

Figure 4.3 – Examples of functionalization chemistry on CNTs. Shown here are oxidation and derivitization reactions[120].

In this chapter, the surface chemistry is achieved by 'wrapping' CNTs with perfluoropolymer chains, which makes both solution processing and fabrication of CNT nanocomposites less challenging. The volume fraction of CNTs in solution can consequently be increased, and with the advantages fCNTs have over conventional superhydrophobic filler materials, this is a noteworthy development in this field. Lastly, CNT nanocomposites which repel organic solvents have not been the subject of many studies in literature, and this chapter opens avenues for further pursuit.

4.3. Experimental Methods

4.3.1. **Preparation of free-standing polymer films**

Both polysulfone (PSF) pellets and polyimide powders were dissolved in tetrahydrofuran (THF) and drop-casted onto glass slides. To control the rate of evaporation, an inverted funnel was placed on top of the slide and left overnight at room temperature. When making N-methylpyrrolidone (NMP)-based films, solutions were drop-casted on slides and left overnight at 100^{o}C in a vacuum oven.

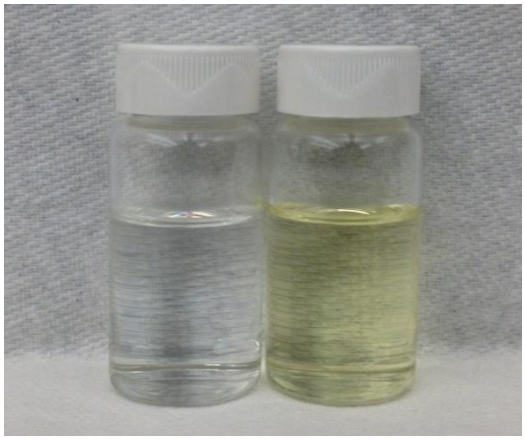

Figure 4.4 – Stable solutions of Polyimide (yellow) and PSF (colorless) in NMP. Solutions in THF also show high solubility.

4.3.2. **CNT growth conditions**

Multi-walled carbon nanotubes (MWNTs) were synthesized via floating catalyst aerosol-assisted chemical vapor deposition onto silicon substrates with a 100 nm oxide layer. The synthesis procedure and apparatus is similar to that published elsewhere[125], [126]. The substrates were placed within a 46 mm I.D.

quartz tube furnace (30 cm heating zone) and brought to a temperature of 800^{0}C in an inert environment and atmospheric pressure conditions. The precursor solution was prepared using toluene (Aldrich, ≥ 99.9%) and ferrocene (Alpha Aesar, 99%) at a concentration of 60 mg/mL. During growth, argon carrier gas flow rate was set to 4.00 L min^{-1} which carried the precursor solution into the reactor in the form of an aerosol generated at a feed rate of 0.8 ml min^{-1} using a 2.4 MHz ultrasonic generator device (Model 241PGT by Sonaer Ultrasonics Inc., Farmingdale, NY).

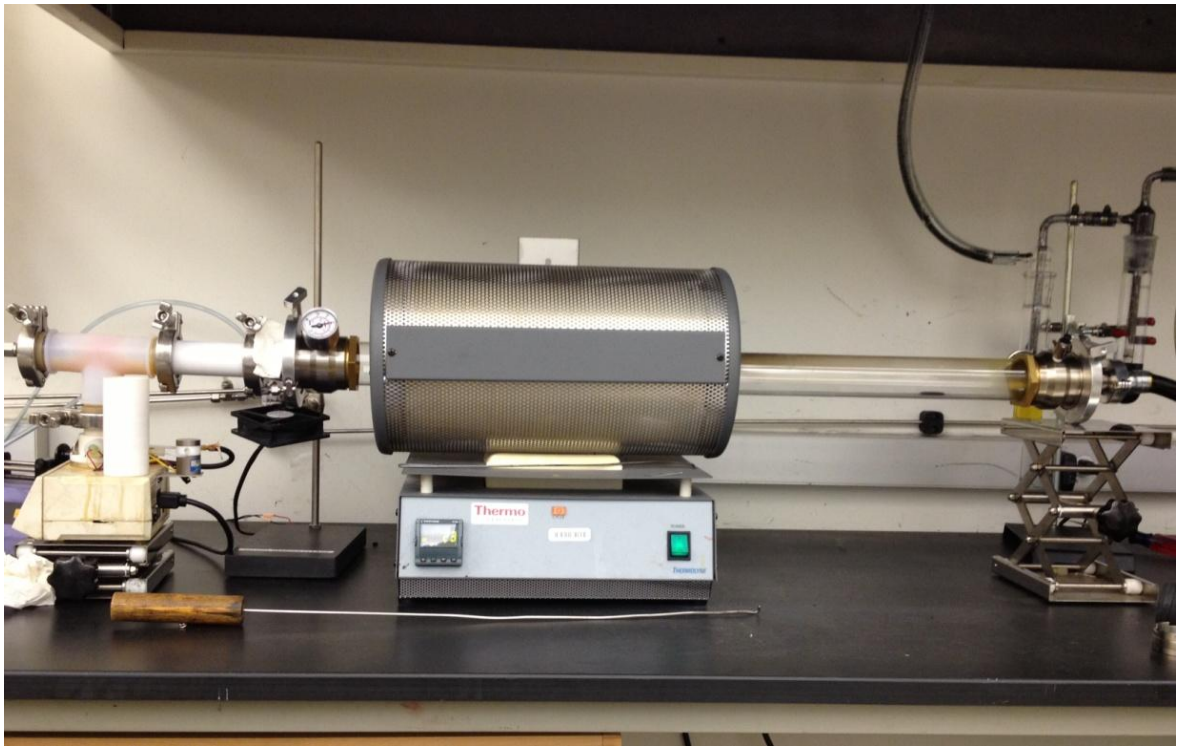

Figure 4.5 – CVD setup for MWNT growth

4.3.3. **Perfluoro-functionalization of CNTs and Deposition**

Carbon nanotubes were functionalized by combining 1 mL of perfluorosulfonic acid-PTFE copolymer solution (5% w/w, Alfa Aesar) with 50 mg of pristine multi-walled nanotubes (MWNTs) in ethanol. The mixture was bath sonicated for 2 hours followed by tip sonication for 5 minutes. All spraying procedures were carried out using an airbrush spray gun (Deluxe Airbrush Kit, Central Pneumatic; Chapter 3). No vacuum drying was required due to the volatile nature of ethanol.

4.3.4. **Isolation of fCNTs and fabrication of supersolvophobic films**

The CNT ink described above was vacuum filtered using a 0.45 μm Fluoropore membrane (Millipore) to isolate perfluoro-functionalized CNTs which showed supersolvophobicity in the solid phase. These were mixed with 5 – 12 wt% solutions of either PSF or polyimide in solvent (THF or NMP) and bath-sonicated overnight and stirred to form composite solutions. These solutions were drop-casted onto desired substrates. Free-standing films were obtained by drop-casting on glass substrates, followed by immersing in a water bath which resulted in superhydrophobic films that were readily removable from the substrate. For comparison, identical procedures were followed to prepare composite films comprising of PTFE-PSF and PTFE-polyimide.

4.3.5. **Characterization**

Scanning electron microscopy (SEM) images were obtained on a high-resolution field-emission scanning electron microscope (FEI Quanta 400) and solid fCNTs were used directly for X-ray photoelectron spectroscopy (XPS, PHI Quantera). Contact angle measurements were performed at laboratory conditions using the standard sessile drop technique. 5 drops of solvent were measured at different places on the film and the average value is reported. The contact angles of both de-ionized water and 30 wt% monoethanolamine (MEA) were measured to characterize the surfaces. For all experiments, 99% purity MEA was used.

4.4. Results & Discussion

Evidence suggests that the inherent nanoscale roughness of a free-standing 'cake' of multi-walled carbon nanotubes (MWNTs) is responsible for their superhydrophobic characteristics as demonstrated in Figure 4.6. The contact angle with deionized water was measured to be 158°, which is consistent with other studies[74].

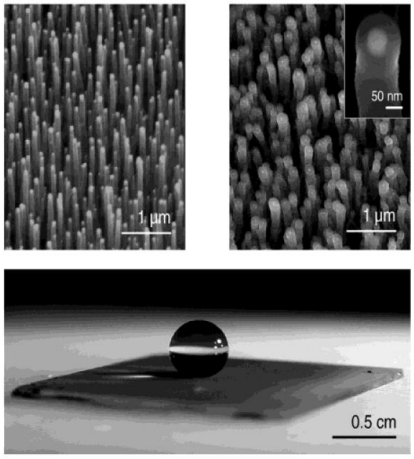

Figure 4.6 – SEM of a CNT 'forest'[74] and a droplet of water being repelled by a free-standing film of CNTs.

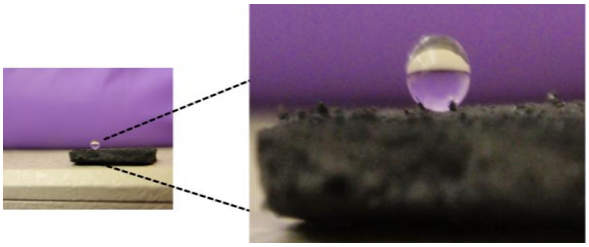

Figure 4.7 – A free-standing 'cake' of MWNTs exhibits a static contact angle of over 150° with deionized water.

Organic solvents such as 30 wt% MEA, penetrate the surface of CNTs due to two mechanisms: firstly, the defined sp^2 domain of MWNTs has great affinity for organic solvents over water and secondly the surface tension of the MEA is considerably lower than water (59 dyn/cm versus 72 dyn/cm for water, 25^{o}C). The need for introducing fluorine into CNTs to reduce its surface free energy is thus apparent. The hypothesis was that an increase in the number of C-F bonds would serve a two-fold purpose: 1) increase supersolvophobicity by decreasing the overall surface free-energy and 2) enable solution processing of MWNTs due to their solubilization. 5% w/w perfluorosulfonic acid – PTFE copolymer (Alfa Aesar, 42118) in its concentrated, aqueous form was an ideal candidate for introducing C-F bonds onto pristine CNTs and *Wang* et al. report wrapping of CNTs by polymeric side chains to show a vast improvement in solubility without limiting the physical properties of CNTs[100].

Upon implementing a similar strategy in this case, the resulting solubilized fCNT solutions showed no aggregation in solution (see Section 4.3). Inks ranging from 5 to 12 wt % fCNTs, e.g. Figure 4.7 (c), were prepared and sprayed on select surfaces with equipment similar to that in Chapter 3. The airbrush paint gun (Figure 3.9) sprayed approximately 200 μl of ink during each run, while the coated substrate shown in Figure 4.7 (d) was obtained after 4 runs. Figure 4.7 (a) shows a droplet of 30 wt% MEA on a film of polyimide (yellow) on a glass substrate displaying a contact angle of 65^{o}. Both polyimide and PSF films (which showed similar contact angles) are relatively *solvophilic*. After spraying the surface of the

polyimide film with 12 wt% fCNT ink, the contact angle of a droplet of 30 wt% MEA increases to 158° (Figure 4.8 (a), (b), (c)). Spray-painted fCNT films were extremely stable at room temperature, and no phase separation was observed on the surface after over 1 week.

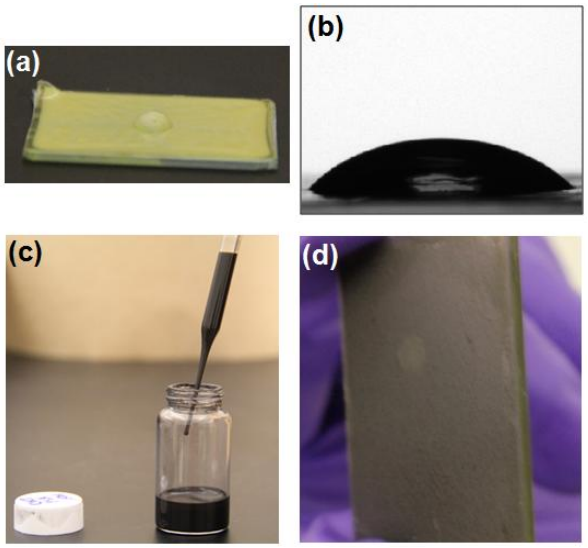

Figure 4.8 – A solvophilic polyimide film (a) shows a contact angle of ~65° with 30 wt% MEA (b). Perfluoro-functionalized CNTs show stability in ethanol up to 12 wt%, due to which inks (c) were created and sprayed onto substrates (d).

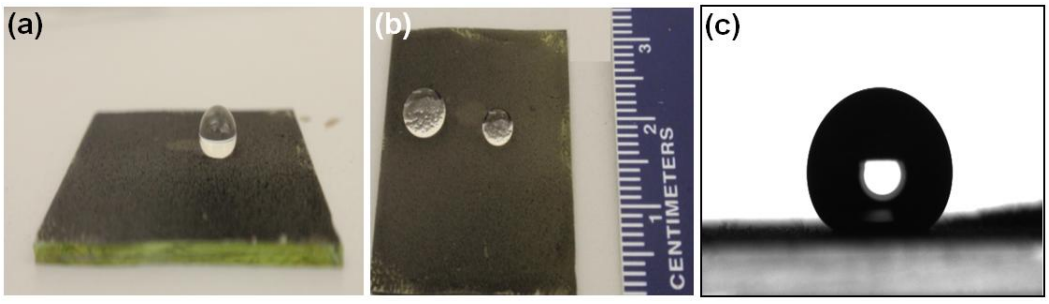

Figure 4.9 – The same film of polyimide demonstrates supersolvophobicity with respect to 30 wt% MEA (a, b) after spraying with perfluoro-functionalized CNTs. The static contact angle is recorded at 158°.

Another possible advantage of spraying inks, specifically those comprising of CNTs, as opposed to conventional coating methods such as drop and spin coating is the surface morphology of the coated layer. *Tuteja* et al. have reported the presence of air pockets upon electrospinning fluoro-POSS (polyhedral oligomeric silsesquioxane) based polymers/fibers that enhance the superoleophobicity of surfaces[69]. These micro-pockets lead to the formation of a metastable solid-liquid-air interface which enables a droplet of a solvent with a lower surface tension to rest on the solid surface without wetting it (Chapter 3). From the SEM images shown in Figures 4.10 (a) and (b), air pockets are observed between the randomly aligned fCNTs. These air pockets contribute to a further decrease in the surface energy in addition to the C-F bonds. This effect is not seen in FGO due to its 'sheeted' morphology, in comparison to the tubular nature of CNTs (i.e. Figure 3.11) . For further studies, this can be exploited by using CNT fibers [126] which can be similarly functionalized in ethanol to form fiber-like surfaces that do not need to be electrospun. Unlike electrospinning the simplistic concept of spray-painting doesn't require a defined infrastructure with a voltage. In addition, spraying bypasses nozzle maintenance issues which have been documented as a disadvantage during electrospinning of nanofibers[127]. In Figure 4.10 (c), XPS spectra of dried fCNTs confirm the presence of the C-F bond in the C1s peak with an atomic C/F ratio of 2.45. Deconvolution of XPS spectra in Figure 4.10 (d) shows the presence of CF_2 groups[91] (291.4 eV), due to functionalization with perfluorosulfonic acid-PTFE copolymer. These groups are directly responsible for reducing the surface energy of

the CNT surface, thereby increasing the supersolvophobicity of the sprayed coating. Alkoxy (C-O, 286.0 eV) signals originate from C-O linkage[13] which are present in the perfluoropolymer.

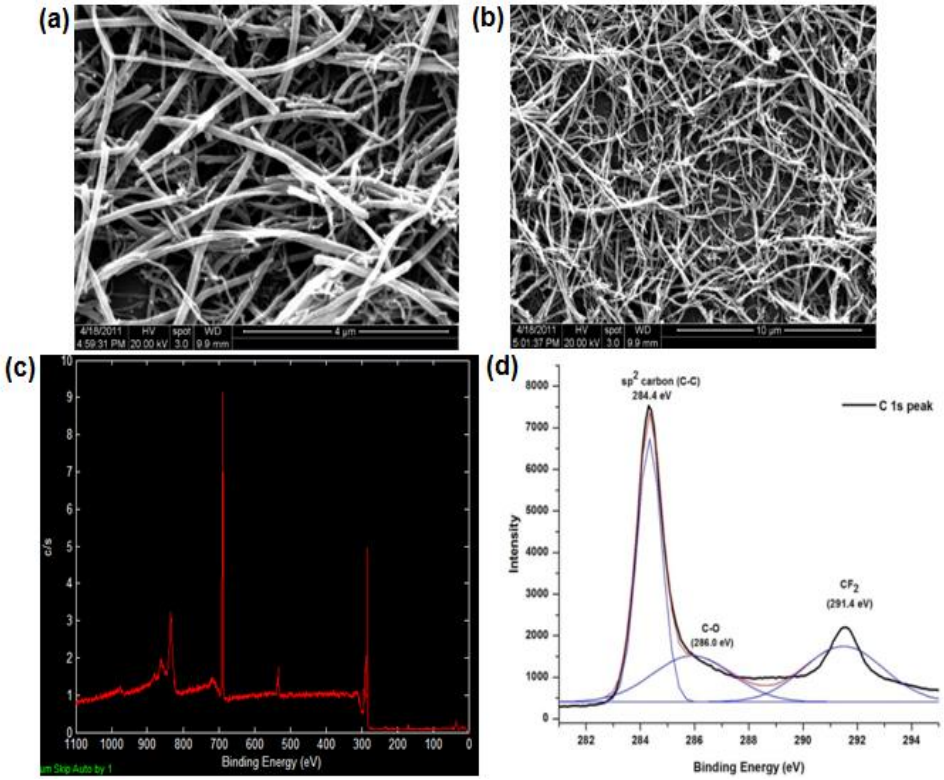

Figure 4.10 – The sprayed fCNT films (a, b) show the p resence of air pockets that could contribute to decreased surface wetting. Deconvoluted XPS spectra identify the nature of fluorine functionality present (c.d).

While supersolvophobic inks are an elegant means to reduce surface wetting, the *intrinsic* wetting characteristics of the polymer remain unchanged. A vast majority of reports suggest that almost all studies that pursue the reduction of surface energy involve surface treatment. Instead, by isolating solid fCNTs, nanocomposites were fabricated that maintained supersolvophobicity throughout

the core of the material. This is a major step up from spray-paintable inks, or any surface treatment for that matter, as a reduction in form factor would lead to a situation where altering the surface chemically would be virtually impossible (i.e. orifices). By creating intrinsically supersolvophobic materials, the material's geometry can be altered thereby reducing its dimensions to micro/nano- scales and bypassing the need for surface treatment of an innately solvophilic material (i.e. polyimide/PSF). The fluorine-based chemistry, however, remains the same.

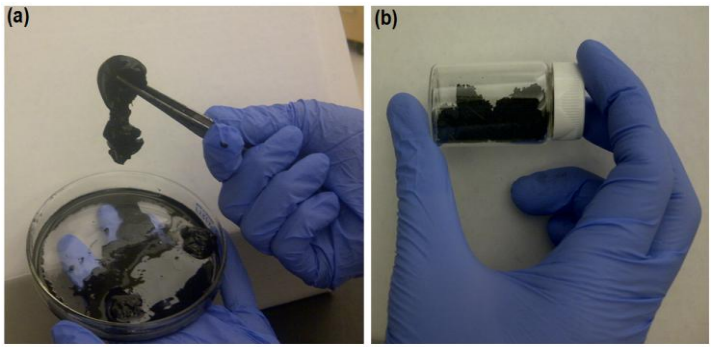

Figure 4.11 – Pristine CNTs reaggregate and precipitate out upon addition of aq. perfluoro-polymer (a) making solution processing a challenge. Instead, fCNTs were filtered, dried and isolate in their solid form (b), and then mixed with the polymer solution.

A key advantage of fCNTs over conventional superhydrophobic filler materials (i.e. PTFE) is their extremely low density, which results in an overall lower void fraction of the fCNT-polymer composite. Thus mixtures of fCNT:polymer at different ratios were created to obtain homogeneous solutions that could be drop-coated to form micron-thick supersolvophobic films. The ratio of fCNT to polymer (PSF or polyimide) was varied until an upper limit was identified at which the

composite film maintained its supersolvophobicity. One of the major challenges was restructuring the experimental methodology as a key parameter during solution processing was identifying a solvent in which (i) both PSF and polyimide were soluble and (ii) fCNTs formed stable dispersions. The high polarity index of THF and NMP made them potential candidates, but that led to the need for an experimental methodology different than that adopted for preparation of fCNT inks (which are ethanol-based). A major challenge consisted of overcoming re-aggregation of polymer (PSF/polyimide) upon addition of aqueous perfluorosulfonic acid – PTFE copolymer to fCNTs dispersed in either THF or NMP (Figure 4.11 (a)). As an alternative, the fCNTs were isolated by vacuum filtration (Figure 4.11 (b)) and simply mixed into PSF/polyimide in THF or NMP. NMP yielded better dispersions due to its higher polarity. Homogeneous, composite solutions consisting of 5 to 15 wt% fCNT showed outstanding stability at room temperature, from which films were drop-casted on the substrate of choice (See Experimental Section for details).

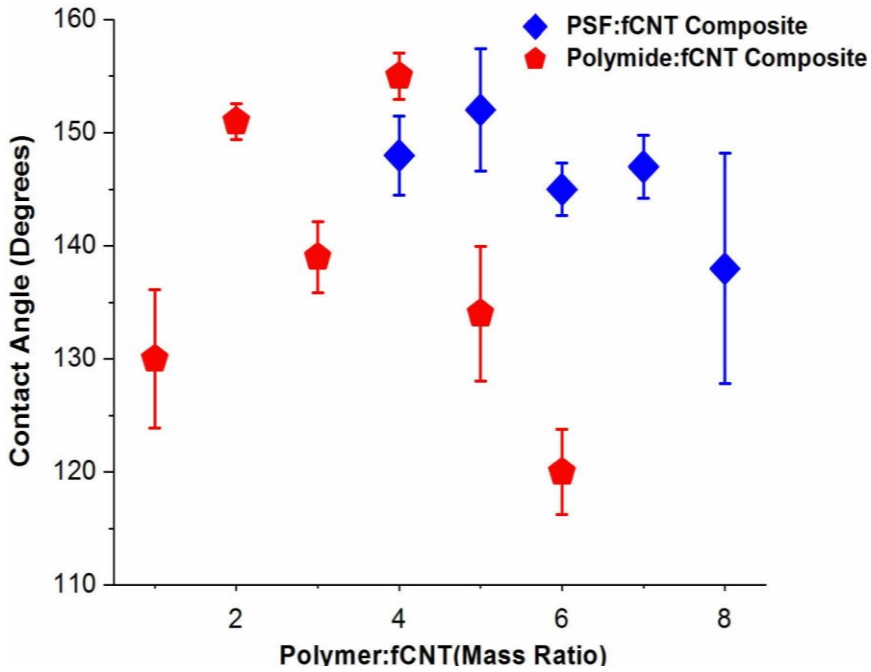

Figure 4.12 – Nanocomposites with both polymers show supersolvophobicity, especially up to 4:1 (polymer:fCNT), after which the contact angle decreases. PSF-fCNT nanocomposites show contact angles that are slightly higher.

As hypothesized, supersolvophobicity was observed in both PSF and polyimide based composite films. The contact angles have been summarized in Figure 4.12, with PSF-fCNT composites showing slightly higher contact angles. Up to ratios of 4:1 (polymer:fCNT) the contact angles are within the 140-155^{o} range, after which there is a considerable drop in polyimide-fCNT composites (120^{o} at 6:1) while PSF-fCNT composites remain within the 140-155^{o} regime up to a ratio of 7:1. Higher contact angles for PSF:fCNT composites could be due to favorable packing of fCNTs within the PSF matrix versus the polyimide matrix.

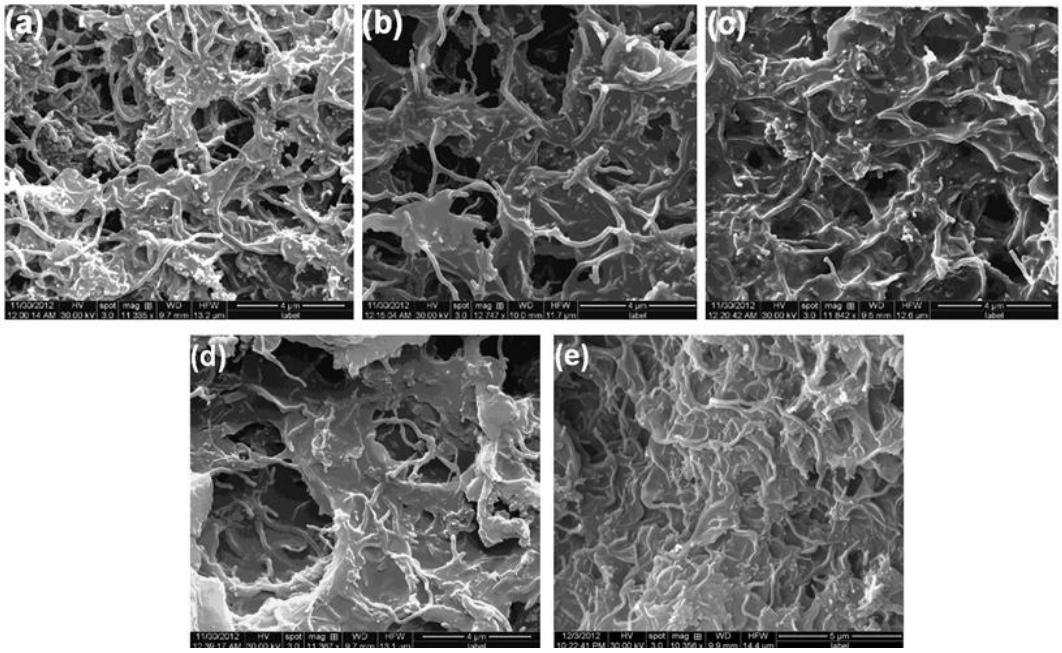

Figure 4.13 – As hypothesized, fCNTs are well dispersed within the polymer matrix. At lower ratios (i.e. 1:2, 1:3 & 1:4) the fCNTs are not engulfed by the polymer matrix, which accounts for the high contact angles that were similar to those observed for sprayed fCNTs. As the ratio increases (1:5, 1:6 and 1:8), the polymer matrix swells to encapsulate fCNTs and dominates the wetting behavior.

SEM images of PSF-fCNT and polyimide-fCNT composites show the fCNTs to be very well dispersed within the respective polymer matrices (shown in Figure 4.13). At lower ratios (up to 1:4), fCNTs are not encapsulated by the swollen polymer matrix, which provides a possible reasoning into why very high contact angles (~150^{o} and higher) are recorded. Intuitively, this fCNT-dominated wetting behavior starts diminishing as the ratio of fCNTs is further decreased and intrinsic polymer wetting dominates as the maximum ratio of 1:7 is approached. As the ratio

was further increased past 1:8, 30 wt% MEA displayed contact angles similar to pristine PSF and polyimide films.

To emphasize the low density of fCNTs as a key advantage in being able to increase their mass fraction in the nanocomposite itself, PTFE-based composites were fabricated as a control. PTFE is a well-known, superhydrophobic material[128]–[130] that has been implemented commercially[131] in various industries. PTFE-PSF and PTFE-polyimide thin films were fabricated using a method similar to that described in Section 4.3 and their contact angles with 30 wt% MEA were compared to fCNT-polymer nanocomposite films. While PTFE composite films also exhibited solvophobicity, presumably due to the high concentration of C-F bonds on the surface, supersolvophobicity is only retained up to ratios of 1:6 and decreases dramatically for ratios greater than that. Both pristine fCNTs and pristine PTFE display identical static contact angles with 30 wt% MEA, which indicates that fCNTs are a superior candidate over PTFE in nanocomposite thin films. The hypothesized reason for this is the low density of fCNTs, which enables them to occupy a greater volume fraction for the same amount of mass, making these composites a superior alternative to commercial alternatives. Taking industrial considerations into account, this is a significant advance of this study.

4.5. Concluding Remarks

In conclusion, this chapter presents two separate methodologies to manipulate the wetting characteristics of naturally solvophilic polymeric materials. The first method introduces a technique to treat the surfaces of PSF and polyimide films by spraying a fluorine-functionalized carbon nanotube (fCNT) based *ink*. The surface energy of CNTs is hypothesized to be reduced by mixing them with aqueous perfluorosulfonic acid – PTFE copolymer in ethanol. Polymeric chains "wrap" around CNTs to enable solution processing in addition to a reduction in surface energy[100]. Introducing an ink greatly improves the accessibility of the supersolvophobic surface and reinforces the advantages that are presented in Chapter 3. However the effects of the fluoropolymer have not been evaluated at higher temperatures, where there is a possibility of HF forming due to a hydrolysis reaction. The second methodology presented in this chapter bypasses the need for surface treatment by creating polymer/fCNT nanocomposites that are *intrinsically* supersolvophobic. This facilitates scaling down to smaller form factors where surface treatment (i.e. spray-painting) is not a viable option, or scaling up to higher dimensions. With 30 wt% MEA a ratio of 7:1 (PSF:fCNT) was identified as an upper limit for supersolvophobicity. Both composite and spray-painted films display contact angle hysteresis under 5^{o}, thus confirming supersolvophobicity. These results provide insight about the interaction between solvents like MEA and supersolvophobic surfaces with carbon nanotubes. By using nanomaterials to

reduce surface wetting, MEA can be exploited further as viable solvent for CO_2 separation.

Chapter 5

Looking Ahead: Further Work from this Thesis

Chemically altering nanomaterials, be it graphene oxide or carbon nanotubes using solution chemistry brings a vast array of advantages. Specific cases of organic and inorganic manipulation have been documented in this thesis, starting with experimentally controlling the functionalities that are reduced on graphene oxide (GO) to introducing fluorine onto its basal plane. Macroscopic consequences of these nanoscale alterations are a sequential reduction in the optical band gap which takes GO from insulating through semiconducting states, while the latter results in a drastic alteration in its wetting characteristics from hydrophilic to superamphiphobic. With respect to CNTs upon reducing their surface energy using a different functionalization approach, a solution-based method has been presented to fabricate nanocomposite structures that are not restricted by form factor that

repel 30 wt% MEA, a critical solvent in CO_2 absorption. This approach has direct applications in the refining industry and is unique in that it doesn't require a fluorinated precursor, as it starts with pristine MWNTs that are surface functionalized, as opposed to fluorinated graphite polymer being oxidized.

5.1. Modeling diffusion kinetics of hydrazine vapors

Each of the chapters have a number of further studies that can be conducted to either develop a better understanding of the reaction mechanisms, or broaden the impact of the material. With partially reduced GO (pRGO) for instance, the diffusivity of hydrazine vapors plays a key role in determining the extent of reaction. Diffusion coefficients in gases are typically between 0.1 – 1 cm^2/s and are usually dependent on the pressure, temperature and molecular weights of the compounds involved [132]. Mathematically, these relationships are not straightforward. If one could model the diffusion of hydrazine vapors within the dessicator and relate it to the extent of reduction of GO, a much more quantitative insight into this problem would be obtained. Secondly, studies to record changes in the structural morphology of GO could also be conducted by exposing it to hydrazine vapors. A monolayer of GO dispersed on an appropriate substrate (i.e. glass slide) can be exposed to hydrazine vapors over time, and subject to HRTEM or *in-situ* TEM to note morphological changes as each functional group is reduced. This could also provide specific points of time when each defect (i.e. Stone Wales, pentagon-heptagon pairs, platelet formation) is introduced onto the graphitic basal plane.

5.2. Direct chemical fluorination of GO

While synthesizing fluorinated graphene oxide (FGO) is a major advance of this thesis, the reported procedure is limited by the raw material: fluorinated graphite polymer (FG). Instead, the richly functionalized basal plane of GO provides tremendous opportunity for additional surface reactions. An example is the thioacetalization reaction, which 'protects' the carbonyl group on the surface of GO by forming a thioacetal using the following reaction[133]:

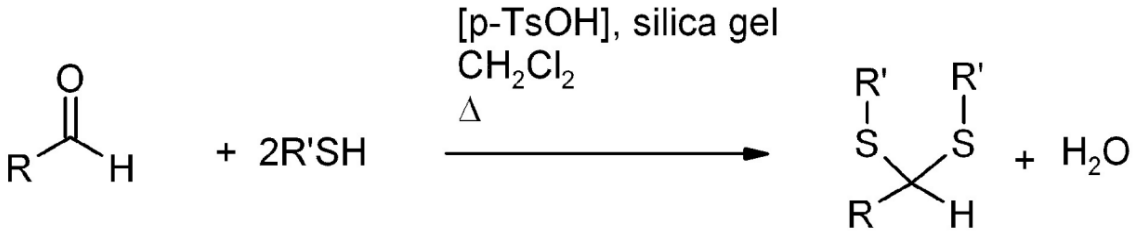

Equation 5.1 – Proposed thioacetalization of graphene oxide[133]

While RC=OH corresponds to carbonyls on graphene oxide, the thiol (R'SH) to be used is 1,2 perfluorodecanethiol ($CF_3(CF_2)_7CH_2CH_2SH$). The presence of a much greater concentration of -CF_3 and –CF_2 over –CF groups will definitely further reduce the surface free energy of GO. Previous studies have reported superamphiphobicity of perfluorodecanethiol, and with the appropriate covalent bond forming on GO, superamphiphobicity below 50 dyn/cm will be retained.

The experiment is straightforward, with dichloromethane being the solvent of choice under reflux, and *p*-toluenesulfonic acid as a catalyst on a bed of silica powder (~4 grams). Characterization of the final product has certain challenges

associated with it due to the presence of excessive silica powder, and calls for chemical means that involve HF etching. Figure 5.1 illustrates these difficulties. Individual silica grains are between 60 – 90 μm in size (Figure 5.1 a), and encapsulate functionalized GO sheets, which are anticipated to be between 100-500 nm. Furthermore silica is hydrophilic and prevents one from understanding the wetting characteristics of perfluoro-functionalized GO itself. Silica powder was dissolved by mixing with HF at different concentrations. The resulting GO powders are currently undergoing characterization, and the first FTIR results are promising (Figure 5.2, on the following page). Two peaks show a gradual increase in intensity as presumably, silica gets dissolved. These peaks are at 1145 cm^{-1} and 1205 cm^{-1} respectively. From previous studies (Chapter 3) the 1205 cm^{-1} peak is very close to the 1208 cm^{-1} peak which indicates covalent C-F bonds, which is extremely encouraging. Further characterization (i.e. XPS, XRD etc) of these powders is ongoing.

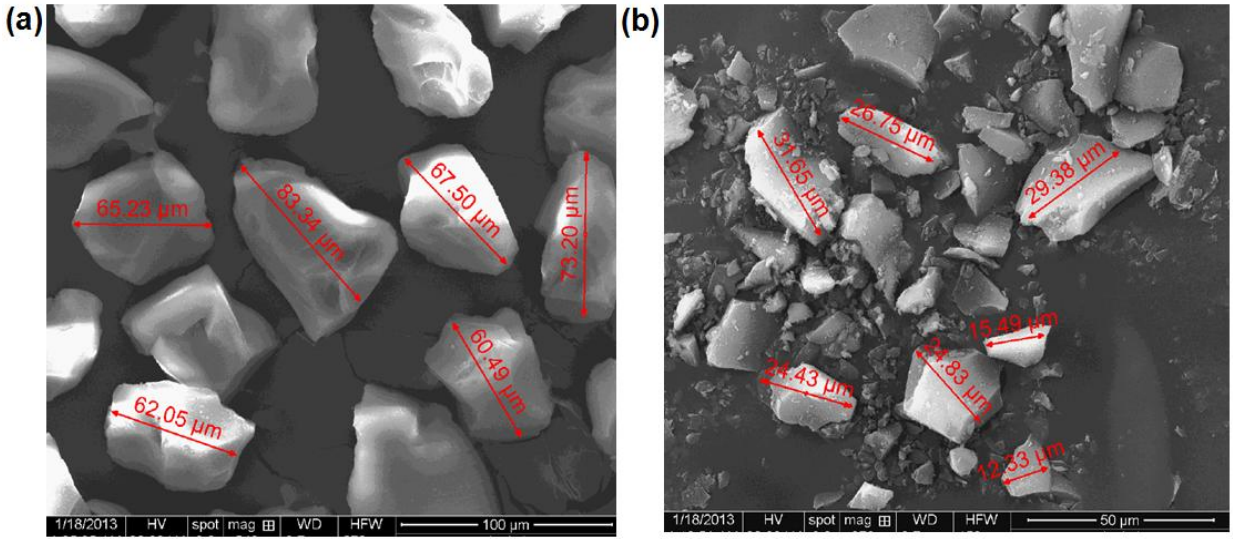

Figure 5.1 - SEM images of pristine silica powder (a) before reaction, and silica-GO mixture (b) post thiocetalization. Characterizing inidividual flakes of GO requires further purificaiton using chemical techniques.

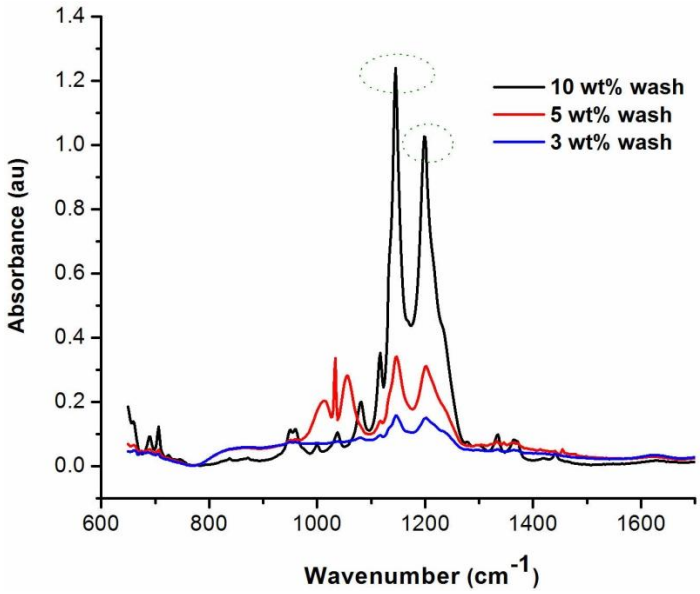

Figure 5.2 – FTIR spectra after HF wash at different concentrations. Two peaks are seen to increase in intensity (circled in green) at 1145 cm^{-1} and 1200 cm^{-1} respectively, as the concentration of HF is increased.

Notes

1. Findings from Chapter 2 published at:

   http://pubs.acs.org/doi/abs/10.1021/jz300096t

2. Findings from Chapter 3 published at:

   http://onlinelibrary.wiley.com/doi/10.1002/ppsc.201200091/pdf

3. Findings from Chapter 4 published at:

   http://pubs.rsc.org/en/content/articlelanding/2013/ra/c3ra22443k

References

[1] A. L. Lavoisier, *Oeuvres: Traité élémentaire de chimie*. Imprimerie impériale, 1864.

[2] J. W. Patrick, Ed., *Porosity in Carbons: Characterization and Applications*, 1st ed. John Wiley & Sons, 1994.

[3] W. I. F. David, R. M. Ibberson, J. C. Matthewman, K. Prassides, T. J. S. Dennis, J. P. Hare, H. W. Kroto, R. Taylor, and D. R. M. Walton, "Crystal structure and bonding of ordered C60," *Nature*, vol. 353, no. 6340, pp. 147–149, Sep. 1991.

[4] H. Kroto, J. Heath, S. O'Brien, R. Curl, and R. Smalley, "C60: Buckminsterfullerene," *Nature*, vol. 318, no. 6042, pp. 162–163, Nov. 1985.

[5] S. Iijima, "Helical microtubules of graphitic carbon," *Nature*, vol. 354, pp. 56–58, Nov. 1991.

[6] K. S. Novoselov, A. K. Geim, S. V. Morozov, D. Jiang, Y. Zhang, S. V. Dubonos, I. V. Grigorieva, and A. A. Firsov, "Electric Field Effect in Atomically Thin Carbon Films," *Science*, vol. 306, no. 5696, pp. 666–669, Oct. 2004.

[7] A. K. Geim and K. S. Novoselov, "The rise of graphene," *Nat Mater*, vol. 6, no. 3, pp. 183–191, Mar. 2007.

[8] T. W. Ebbesen and P. M. Ajayan, "Large-scale synthesis of carbon nanotubes," *Nature*, vol. 358, no. 6383, pp. 220–222, Jul. 1992.

[9] W. Gao, L. B. Alemany, L. Ci, and P. M. Ajayan, "New insights into the structure and reduction of graphite oxide," *Nat Chem*, vol. 1, no. 5, pp. 403–408, Aug. 2009.

[10] K. P. Loh, Q. Bao, G. Eda, and M. Chhowalla, "Graphene oxide as a chemically tunable platform for optical applications," *Nature Chemistry*, vol. 2, no. 12, pp. 1015–1024, 2010.

[11] H. A. Becerril, J. Mao, Z. Liu, R. M. Stoltenberg, Z. Bao, and Y. Chen, "Evaluation of Solution-Processed Reduced Graphene Oxide Films as Transparent Conductors," *ACS Nano*, vol. 2, no. 3, pp. 463–470, Mar. 2008.

[12] D. A. Dikin, S. Stankovich, E. J. Zimney, R. D. Piner, G. H. B. Dommett, G. Evmenenko, S. T. Nguyen, and R. S. Ruoff, "Preparation and characterization of graphene oxide paper," *Nature*, vol. 448, no. 7152, pp. 457–460, Jul. 2007.

[13] D. R. Dreyer, S. Park, C. W. Bielawski, and R. S. Ruoff, "The chemistry of graphene oxide," *Chem. Soc. Rev.*, vol. 39, no. 1, pp. 228–240, Dec. 2009.

[14] G. Eda, G. Fanchini, and M. Chhowalla, "Large-area ultrathin films of reduced graphene oxide as a transparent and flexible electronic material," *Nat Nano*, vol. 3, no. 5, pp. 270–274, May 2008.

[15] D. R. Dreyer, R. S. Ruoff, and C. W. Bielawski, "From Conception to Realization: An Historial Account of Graphene and Some Perspectives for Its Future," *Angewandte Chemie International Edition*, vol. 49, no. 49, pp. 9336–9344, 2010.

[16] A. Mathkar, D. Tozier, P. Cox, P. Ong, C. Galande, K. Balakrishnan, A. Leela Mohana Reddy, and P. M. Ajayan, "Controlled, Stepwise Reduction and Band Gap Manipulation of Graphene Oxide," *J. Phys. Chem. Lett.*, vol. 3, no. 8, pp. 986–991, Apr. 2012.

[17] C. Gómez-Navarro, R. T. Weitz, A. M. Bittner, M. Scolari, A. Mews, M. Burghard, and K. Kern, "Electronic Transport Properties of Individual Chemically Reduced Graphene Oxide Sheets," *Nano Lett.*, vol. 7, no. 11, pp. 3499–3503, Nov. 2007.

[18] X. Gao, J. Jang, and S. Nagase, "Hydrazine and Thermal Reduction of Graphene Oxide: Reaction Mechanisms, Product Structures, and Reaction Design," *J. Phys. Chem. C*, vol. 114, no. 2, pp. 832–842, Jan. 2010.

[19] S. Park, Y. Hu, J. O. Hwang, E.-S. Lee, L. B. Casabianca, W. Cai, J. R. Potts, H.-W. Ha, S. Chen, J. Oh, S. O. Kim, Y.-H. Kim, Y. Ishii, and R. S. Ruoff, "Chemical structures of hydrazine-treated graphene oxide and generation of aromatic nitrogen doping," *Nat Commun*, vol. 3, p. 638, Jan. 2012.

[20] J. I. Paredes, S. Villar-Rodil, A. Martínez-Alonso, and J. M. D. Tascón, "Graphene Oxide Dispersions in Organic Solvents," *Langmuir*, vol. 24, no. 19, pp. 10560–10564, Oct. 2008.

[21] C. Schafhaeutl, "LXXXVI. On the combinations of carbon with silicon and iron, and other metals, forming the different species of cast iron, steel, and malleable iron," *Philosophical Magazine Series 3*, vol. 16, no. 106, pp. 570–590, 1840.

[22] B. C. Brodie, "On the Atomic Weight of Graphite," *Philosophical Transactions of the Royal Society of London*, vol. 149, pp. 249–259, Jan. 1859.

[23] L. Staudenmaier, "Verfahren zur Darstellung der Graphitsäure," *Berichte der deutschen chemischen Gesellschaft*, vol. 31, no. 2, pp. 1481–1487, 1898.

[24] W. S. Hummers and R. E. Offeman, "Preparation of Graphitic Oxide," *J. Am. Chem. Soc.*, vol. 80, no. 6, pp. 1339–1339, Mar. 1958.

[25] K. R. Koch, "Oxidation by Mn207: An impressive demonstration of the powerful oxidizing property of dimanganeseheptoxide," *J. Chem. Educ.*, vol. 59, no. 11, p. 973, Nov. 1982.

[26] N. I. Kovtyukhova, P. J. Ollivier, B. R. Martin, T. E. Mallouk, S. A. Chizhik, E. V. Buzaneva, and A. D. Gorchinskiy, "Layer-by-Layer Assembly of Ultrathin Composite Films from Micron-Sized Graphite Oxide Sheets and Polycations," *Chem. Mater.*, vol. 11, no. 3, pp. 771–778, Mar. 1999.

[27] D. C. Marcano, D. V. Kosynkin, J. M. Berlin, A. Sinitskii, Z. Sun, A. Slesarev, L. B. Alemany, W. Lu, and J. M. Tour, "Improved Synthesis of Graphene Oxide," *ACS Nano*, vol. 4, no. 8, pp. 4806–4814, Aug. 2010.

[28] D. V. Kosynkin, A. L. Higginbotham, A. Sinitskii, J. R. Lomeda, A. Dimiev, B. K. Price, and J. M. Tour, "Longitudinal unzipping of carbon nanotubes to form graphene nanoribbons," *Nature*, vol. 458, no. 7240, pp. 872–876, Apr. 2009.

[29] W. Cai, R. D. Piner, F. J. Stadermann, S. Park, M. A. Shaibat, Y. Ishii, D. Yang, A. Velamakanni, S. J. An, M. Stoller, J. An, D. Chen, and R. S. Ruoff, "Synthesis and Solid-State NMR Structural Characterization of 13C-Labeled Graphite Oxide," *Science*, vol. 321, no. 5897, pp. 1815–1817, Sep. 2008.

[30] A. Lerf, H. He, M. Forster, and J. Klinowski, "Structure of Graphite Oxide Revisited‖," *J. Phys. Chem. B*, vol. 102, no. 23, pp. 4477–4482, Jun. 1998.
[31] J. P. Rourke, P. A. Pandey, J. J. Moore, M. Bates, I. A. Kinloch, R. J. Young, and N. R. Wilson, "The Real Graphene Oxide Revealed: Stripping the Oxidative Debris from the Graphene-like Sheets," *Angewandte Chemie International Edition*, vol. 50, no. 14, pp. 3173–3177, Mar. 2011.
[32] A. M. Dimiev, L. B. Alemany, and J. M. Tour, "Graphene Oxide. Origin of Acidity, Its Instability in Water, and a New Dynamic Structural Model," *ACS Nano*, vol. 7, no. 1, pp. 576–588, Jan. 2013.
[33] S. Stankovich, D. A. Dikin, R. D. Piner, K. A. Kohlhaas, A. Kleinhammes, Y. Jia, Y. Wu, S. T. Nguyen, and R. S. Ruoff, "Synthesis of graphene-based nanosheets via chemical reduction of exfoliated graphite oxide," *Carbon*, vol. 45, no. 7, pp. 1558–1565, Jun. 2007.
[34] A. Celzard, J. F. Marêché, F. Payot, and G. Furdin, "Electrical conductivity of carbonaceous powders," *Carbon*, vol. 40, no. 15, pp. 2801–2815, 2002.
[35] D. S. McLachlan, "Equations for the conductivity of macroscopic mixtures," *J. Phys. C: Solid State Phys.*, vol. 19, no. 9, p. 1339, Mar. 1986.
[36] D. S. McLachlan, "An equation for the conductivity of binary mixtures with anisotropic grain structures," *J. Phys. C: Solid State Phys.*, vol. 20, no. 7, p. 865, Mar. 1987.
[37] H. C. Schniepp, J.-L. Li, M. J. McAllister, H. Sai, M. Herrera-Alonso, D. H. Adamson, R. K. Prud'homme, R. Car, D. A. Saville, and I. A. Aksay, "Functionalized Single Graphene Sheets Derived from Splitting Graphite Oxide," *J. Phys. Chem. B*, vol. 110, no. 17, pp. 8535–8539, May 2006.
[38] K. N. Kudin, B. Ozbas, H. C. Schniepp, R. K. Prud'homme, I. A. Aksay, and R. Car, "Raman Spectra of Graphite Oxide and Functionalized Graphene Sheets," *Nano Lett.*, vol. 8, no. 1, pp. 36–41, Jan. 2008.
[39] A. Bagri, C. Mattevi, M. Acik, Y. J. Chabal, M. Chhowalla, and V. B. Shenoy, "Structural evolution during the reduction of chemically derived graphene oxide," *Nature Chemistry*, vol. 2, no. 7, pp. 581–587, Jun. 2010.
[40] H. A. Becerril, J. Mao, Z. Liu, R. M. Stoltenberg, Z. Bao, and Y. Chen, "Evaluation of Solution-Processed Reduced Graphene Oxide Films as Transparent Conductors," *ACS Nano*, vol. 2, no. 3, pp. 463–470, Mar. 2008.
[41] K.-H. Liao, A. Mittal, S. Bose, C. Leighton, K. A. Mkhoyan, and C. W. Macosko, "Aqueous Only Route toward Graphene from Graphite Oxide," *ACS Nano*, vol. 5, no. 2, pp. 1253–1258, Feb. 2011.
[42] J. E. Kim, T. H. Han, S. H. Lee, J. Y. Kim, C. W. Ahn, J. M. Yun, and S. O. Kim, "Graphene Oxide Liquid Crystals," *Angewandte Chemie International Edition*, vol. 50, no. 13, pp. 3043–3047, Mar. 2011.
[43] C. M. Hill, Y. Zhu, and S. Pan, "Fluorescence and Electroluminescence Quenching Evidence of Interfacial Charge Transfer in Poly (3-hexylthiophene): Graphene Oxide Bulk Heterojunction Photovoltaic Devices," *ACS Nano*, vol. 5, no. 2, pp. 942–951, Feb. 2011.

[44] O. C. Compton, B. Jain, D. A. Dikin, A. Abouimrane, K. Amine, and S. T. Nguyen, "Chemically Active Reduced Graphene Oxide with Tunable C/O Ratios," *ACS Nano*, vol. 5, no. 6, pp. 4380–4391, Jun. 2011.

[45] A. J. Patil, J. L. Vickery, T. B. Scott, and S. Mann, "Aqueous Stabilization and Self-Assembly of Graphene Sheets into Layered Bio-Nanocomposites using DNA," *Advanced Materials*, vol. 21, no. 31, pp. 3159–3164, 2009.

[46] Y. Wang, Z. Li, D. Hu, C.-T. Lin, J. Li, and Y. Lin, "Aptamer/Graphene Oxide Nanocomplex for in Situ Molecular Probing in Living Cells," *J. Am. Chem. Soc.*, vol. 132, no. 27, pp. 9274–9276, Jul. 2010.

[47] J. D. Fowler, M. J. Allen, V. C. Tung, Y. Yang, R. B. Kaner, and B. H. Weiller, "Practical Chemical Sensors from Chemically Derived Graphene," *ACS Nano*, vol. 3, no. 2, pp. 301–306, Feb. 2009.

[48] X. Li, H. Wang, J. T. Robinson, H. Sanchez, G. Diankov, and H. Dai, "Simultaneous Nitrogen Doping and Reduction of Graphene Oxide," *J. Am. Chem. Soc.*, vol. 131, no. 43, pp. 15939–15944, Nov. 2009.

[49] J. M. Englert, C. Dotzer, G. Yang, M. Schmid, C. Papp, J. M. Gottfried, H.-P. Steinrück, E. Spiecker, F. Hauke, and A. Hirsch, "Covalent bulk functionalization of graphene," *Nature Chemistry*, vol. 3, no. 4, pp. 279–286, Mar. 2011.

[50] D. Li, M. B. Müller, S. Gilje, R. B. Kaner, and G. G. Wallace, "Processable aqueous dispersions of graphene nanosheets," *Nat Nano*, vol. 3, no. 2, pp. 101–105, Feb. 2008.

[51] L. Ci, L. Song, C. Jin, D. Jariwala, D. Wu, Y. Li, A. Srivastava, Z. F. Wang, K. Storr, L. Balicas, F. Liu, and P. M. Ajayan, "Atomic layers of hybridized boron nitride and graphene domains," *Nat Mater*, vol. 9, no. 5, pp. 430–435, May 2010.

[52] S.-S. Li, K.-H. Tu, C.-C. Lin, C.-W. Chen, and M. Chhowalla, "Solution-Processable Graphene Oxide as an Efficient Hole Transport Layer in Polymer Solar Cells," *ACS Nano*, vol. 4, no. 6, pp. 3169–3174, Jun. 2010.

[53] H.-C. Hsu, I. Shown, H.-Y. Wei, Y.-C. Chang, H.-Y. Du, Y.-G. Lin, C.-A. Tseng, C.-H. Wang, L.-C. Chen, Y.-C. Lin, and K.-H. Chen, "Graphene oxide as a promising photocatalyst for CO2 to methanol conversion," *Nanoscale*, vol. 5, no. 1, pp. 262–268, Dec. 2012.

[54] L. Song, L. Ci, H. Lu, P. B. Sorokin, C. Jin, J. Ni, A. G. Kvashnin, D. G. Kvashnin, J. Lou, B. I. Yakobson, and P. M. Ajayan, "Large Scale Growth and Characterization of Atomic Hexagonal Boron Nitride Layers," *Nano Letters*, vol. 10, no. 8, pp. 3209–3215, Aug. 2010.

[55] G. Eda, C. Mattevi, H. Yamaguchi, H. Kim, and M. Chhowalla, "Insulator to Semimetal Transition in Graphene Oxide," *J. Phys. Chem. C*, vol. 113, no. 35, pp. 15768–15771, Sep. 2009.

[56] Y. Matsuo, T. Mimura, and Y. Sugie, "Preparation of Semiconducting Graphene-based Carbon Films from Silylated Graphite Oxide and Covalent Attachment of Dye Molecules," *Chemistry Letters*, vol. 39, no. 6, pp. 636–637, 2010.

[57] N. B. Colthup, L. H. Daly, and S. E. Wiberley, *Introduction to Infrared and Raman Spectroscopy, Third Edition*, 3rd ed. Academic Press, 1990.

[58] W. R. Collins, E. Schmois, and T. M. Swager, "Graphene oxide as an electrophile for carbon nucleophiles," *Chemical Communications*, vol. 47, no. 31, p. 8790, 2011.
[59] M. Acik, G. Lee, C. Mattevi, M. Chhowalla, K. Cho, and Y. J. Chabal, "Unusual infrared-absorption mechanism in thermally reduced graphene oxide," *Nat Mater*, vol. 9, no. 10, pp. 840–845, Oct. 2010.
[60] Y. Si and E. T. Samulski, "Synthesis of Water Soluble Graphene," *Nano Letters*, vol. 8, no. 6, pp. 1679–1682, Jun. 2008.
[61] H. K. Jeong, M. H. Jin, K. P. So, S. C. Lim, and Y. H. Lee, "Tailoring the characteristics of graphite oxides by different oxidation times," *Journal of Physics D: Applied Physics*, vol. 42, no. 6, p. 065418, Mar. 2009.
[62] M. Jin, H.-K. Jeong, W. J. Yu, D. J. Bae, B. R. Kang, and Y. H. Lee, "Graphene oxide thin film field effect transistors without reduction," *Journal of Physics D: Applied Physics*, vol. 42, no. 13, p. 135109, Jul. 2009.
[63] J. T. Robinson, F. K. Perkins, E. S. Snow, Z. Wei, and P. E. Sheehan, "Reduced Graphene Oxide Molecular Sensors," *Nano Lett.*, vol. 8, no. 10, pp. 3137–3140, Oct. 2008.
[64] X. Sun, Z. Liu, K. Welsher, J. T. Robinson, A. Goodwin, S. Zaric, and H. Dai, "Nano-graphene oxide for cellular imaging and drug delivery," *Nano Res.*, vol. 1, no. 3, pp. 203–212, Sep. 2008.
[65] P. Chantharasupawong, R. Philip, N. T. Narayanan, P. M. Sudeep, A. Mathkar, P. M. Ajayan, and J. Thomas, "Optical Power Limiting in Fluorinated Graphene Oxide: An Insight into the Nonlinear Optical Properties," *J. Phys. Chem. C*, vol. 116, no. 49, pp. 25955–25961, Dec. 2012.
[66] J. A. Wilkinson, "Recent advances in the selective formation of the carbon-fluorine bond," *Chemical reviews*, vol. 92, no. 4, pp. 505–519, 1992.
[67] I. B. Johns, E. A. McElhill, and J. O. Smith, "Thermal Stability of Some Organic Compounds.," *J. Chem. Eng. Data*, vol. 7, no. 2, pp. 277–281, Apr. 1962.
[68] M. Srinivas, P. A. Morel, L. A. Ernst, D. H. Laidlaw, and E. T. Ahrens, "Fluorine-19 MRI for visualization and quantification of cell migration in a diabetes model," *Magnetic Resonance in Medicine*, vol. 58, no. 4, pp. 725–734, 2007.
[69] A. Tuteja, W. Choi, M. Ma, J. M. Mabry, S. A. Mazzella, G. C. Rutledge, G. H. McKinley, and R. E. Cohen, "Designing Superoleophobic Surfaces," *Science*, vol. 318, no. 5856, pp. 1618–1622, Dec. 2007.
[70] Y. Liu, R. L. Vander Wal, and V. N. Khabashesku, "Functionalization of Carbon Nano-onions by Direct Fluorination," *Chemistry of Materials*, vol. 19, no. 4, pp. 778–786, Feb. 2007.
[71] J. T. Robinson, J. S. Burgess, C. E. Junkermeier, S. C. Badescu, T. L. Reinecke, F. K. Perkins, M. K. Zalalutdniov, J. W. Baldwin, J. C. Culbertson, P. E. Sheehan, and E. S. Snow, "Properties of Fluorinated Graphene Films," *Nano Letters*, vol. 10, no. 8, pp. 3001–3005, Aug. 2010.
[72] S. S. Han, T. H. Yu, B. V. Merinov, A. C. T. van Duin, R. Yazami, and W. A. Goddard, "Unraveling Structural Models of Graphite Fluorides by Density

Functional Theory Calculations," *Chem. Mater.*, vol. 22, no. 6, pp. 2142–2154, Mar. 2010.

[73] A. Lafuma and D. Quéré, "Superhydrophobic states," *Nature Materials*, vol. 2, no. 7, pp. 457–460, Jun. 2003.

[74] K. K. S. Lau, J. Bico, K. B. K. Teo, M. Chhowalla, G. A. J. Amaratunga, W. I. Milne, G. H. McKinley, and K. K. Gleason, "Superhydrophobic Carbon Nanotube Forests," *Nano Letters*, vol. 3, no. 12, pp. 1701–1705, Dec. 2003.

[75] M. Im, H. Im, J.-H. Lee, J.-B. Yoon, and Y.-K. Choi, "A robust superhydrophobic and superoleophobic surface with inverse-trapezoidal microstructures on a large transparent flexible substrate," *Soft Matter*, vol. 6, no. 7, p. 1401, 2010.

[76] C. Luo, X. Zuo, L. Wang, E. Wang, S. Song, J. Wang, J. Wang, C. Fan, and Y. Cao, "Flexible Carbon Nanotube–Polymer Composite Films with High Conductivity and Superhydrophobicity Made by Solution Process," *Nano Letters*, vol. 8, no. 12, pp. 4454–4458, Dec. 2008.

[77] W. Barthlott and C. Neinhuis, "Purity of the sacred lotus, or escape from contamination in biological surfaces," *Planta*, vol. 202, no. 1, pp. 1–8, Apr. 1997.

[78] X. Deng, L. Mammen, H.-J. Butt, and D. Vollmer, "Candle Soot as a Template for a Transparent Robust Superamphiphobic Coating," *Science*, vol. 335, no. 6064, pp. 67–70, Dec. 2011.

[79] L. Cao, T. P. Price, M. Weiss, and D. Gao, "Super Water- and Oil-Repellent Surfaces on Intrinsically Hydrophilic and Oleophilic Porous Silicon Films," *Langmuir*, vol. 24, no. 5, pp. 1640–1643, Mar. 2008.

[80] B. Leng, Z. Shao, G. de With, and W. Ming, "Superoleophobic Cotton Textiles," *Langmuir*, vol. 25, no. 4, pp. 2456–2460, Feb. 2009.

[81] T. Darmanin, F. Guittard, S. Amigoni, E. T. de Givenchy, X. Noblin, R. Kofman, and F. Celestini, "Superoleophobic behavior of fluorinated conductive polymer films combining electropolymerization and lithography," *Soft Matter*, vol. 7, no. 3, pp. 1053–1057, Jan. 2011.

[82] J. Yang, Z. Zhang, X. Men, X. Xu, and X. Zhu, "A simple approach to fabricate superoleophobic coatings," *New Journal of Chemistry*, vol. 35, no. 3, p. 576, 2011.

[83] D. Wang, X. Wang, X. Liu, and F. Zhou, "Engineering a Titanium Surface with Controllable Oleophobicity and Switchable Oil Adhesion," *J. Phys. Chem. C*, vol. 114, no. 21, pp. 9938–9944, Jun. 2010.

[84] H. Zhao, K.-Y. Law, and V. Sambhy, "Fabrication, Surface Properties, and Origin of Superoleophobicity for a Model Textured Surface," *Langmuir*, vol. 27, no. 10, pp. 5927–5935, May 2011.

[85] A. Mathkar, T. N. Narayanan, L. B. Alemany, P. Cox, P. Nguyen, G. Gao, P. Chang, R. Romero-Aburto, S. A. Mani, and P. M. Ajayan, "Synthesis of Fluorinated Graphene Oxide and its Amphiphobic Properties," *Particle & Particle Systems Characterization*, p. n/a–n/a, 2013.

[86] V. N. Mitkin, "Types of Inorganic Fluorocarbon Polymer Materials and Structure–Property Correlation Problems," *Journal of Structural Chemistry*, vol. 44, no. 1, pp. 82–115, 2003.

[87] G. Vázquez, E. Alvarez, J. M. Navaza, R. Rendo, and E. Romero, "Surface tension of binary mixtures of water+ monoethanolamine and water+ 2-amino-2-methyl-1-propanol and tertiary mixtures of these amines with water from 25 C to 50 C," *Journal of Chemical & Engineering Data*, vol. 42, no. 1, pp. 57–59, 1997.

[88] G. Vazquez, E. Alvarez, and J. M. Navaza, "Surface Tension of Alcohol Water + Water from 20 to 50 .degree.C," *J. Chem. Eng. Data*, vol. 40, no. 3, pp. 611–614, May 1995.

[89] V. N. Mitkin, "Types of Inorganic Fluorocarbon Polymer Materials and Structure–Property Correlation Problems," *Journal of Structural Chemistry*, vol. 44, no. 1, pp. 82–115, Jan. 2003.

[90] L. B. Alemany, L. Zhang, L. Zeng, C. L. Edwards, and A. R. Barron, "Solid-State NMR Analysis of Fluorinated Single-Walled Carbon Nanotubes: Assessing the Extent of Fluorination," *Chem. Mater.*, vol. 19, no. 4, pp. 735–744, Feb. 2007.

[91] S. R. Coulson, I. S. Woodward, J. P. S. Badyal, S. A. Brewer, and C. Willis, "Ultralow Surface Energy Plasma Polymer Films," *Chemistry of Materials*, vol. 12, no. 7, pp. 2031–2038, Jul. 2000.

[92] Y. Nishi, "Lithium ion secondary batteries; past 10 years and the future," *Journal of Power Sources*, vol. 100, no. 1, pp. 101–106, 2001.

[93] W. Gao, N. Singh, L. Song, Z. Liu, A. L. M. Reddy, L. Ci, R. Vajtai, Q. Zhang, B. Wei, and P. M. Ajayan, "Direct laser writing of micro-supercapacitors on hydrated graphite oxide films," *Nature Nanotechnology*, vol. 6, no. 8, pp. 496–500, Jul. 2011.

[94] H. Y. Erbil, A. L. Demirel, Y. Avcı, and O. Mert, "Transformation of a Simple Plastic into a Superhydrophobic Surface," *Science*, vol. 299, no. 5611, pp. 1377–1380, Feb. 2003.

[95] P. M. Ajayan, T. W. Ebbesen, T. Ichihashi, S. Iijima, K. Tanigaki, and H. Hiura, "Opening carbon nanotubes with oxygen and implications for filling," *Nature*, vol. 362, no. 6420, pp. 522–525, Apr. 1993.

[96] P. M. Ajayan and S. Lijima, "Capillarity-induced filling of carbon nanotubes," *Nature*, vol. 361, no. 6410, pp. 333–334, Jan. 1993.

[97] L. Feng, S. Li, Y. Li, H. Li, L. Zhang, J. Zhai, Y. Song, B. Liu, L. Jiang, and D. Zhu, "Super-Hydrophobic Surfaces: From Natural to Artificial," *Advanced materials*, vol. 14, no. 24, pp. 1857–1860, 2002.

[98] S. Li, H. Li, X. Wang, Y. Song, Y. Liu, L. Jiang, and D. Zhu, "Super-Hydrophobicity of Large-Area Honeycomb-Like Aligned Carbon Nanotubes," *J. Phys. Chem. B*, vol. 106, no. 36, pp. 9274–9276, Sep. 2002.

[99] Y. C. Hong and H. S. Uhm, "Superhydrophobicity of a material made from multiwalled carbon nanotubes," *Applied Physics Letters*, vol. 88, no. 24, pp. 244101–244101–3, Jun. 2006.

[100] J. Wang, M. Musameh, and Y. Lin, "Solubilization of Carbon Nanotubes by Nafion toward the Preparation of Amperometric Biosensors," *Journal of the American Chemical Society*, vol. 125, no. 9, pp. 2408–2409, Mar. 2003.

[101] P. M. Ajayan and O. Z. Zhou, "Applications of Carbon Nanotubes," in *Carbon Nanotubes*, M. S. Dresselhaus, G. Dresselhaus, and P. Avouris, Eds. Springer Berlin Heidelberg, 2001, pp. 391–425.
[102] M. S. Dresselhaus, G. Dresselhaus, and P. C. Eklund, *Science of Fullerenes and Carbon Nanotubes: Their Properties and Applications*. Academic Press, 1996.
[103] P. G. Collins, K. Bradley, M. Ishigami, and A. Zettl, "Extreme Oxygen Sensitivity of Electronic Properties of Carbon Nanotubes," *Science*, vol. 287, no. 5459, pp. 1801–1804, Mar. 2000.
[104] O. Tw, H. Jl, K. P, and L. Cm, "Atomic structure and electronic properties of single-walled carbon nanotubes," *Nature*, vol. 391, no. 6662, pp. 62–64, 1998.
[105] R. S. Ruoff and D. C. Lorents, "Mechanical and thermal properties of carbon nanotubes," *Carbon*, vol. 33, no. 7, pp. 925–930, 1995.
[106] M. M. J. Treacy, T. W. Ebbesen, and J. M. Gibson, "Exceptionally high Young's modulus observed for individual carbon nanotubes," *Nature*, vol. 381, no. 6584, pp. 678–680.
[107] X. Wang, Q. Li, J. Xie, Z. Jin, J. Wang, Y. Li, K. Jiang, and S. Fan, "Fabrication of Ultralong and Electrically Uniform Single-Walled Carbon Nanotubes on Clean Substrates," *Nano Lett.*, vol. 9, no. 9, pp. 3137–3141, Sep. 2009.
[108] M. Meo and M. Rossi, "Prediction of Young's modulus of single wall carbon nanotubes by molecular-mechanics based finite element modelling," *Composites Science and Technology*, vol. 66, no. 11–12, pp. 1597–1605, Sep. 2006.
[109] S. Bellucci, "Carbon nanotubes: physics and applications," *physica status solidi (c)*, vol. 2, no. 1, pp. 34–47, 2005.
[110] H. G. Chae and S. Kumar, "Rigid-rod polymeric fibers," *Journal of Applied Polymer Science*, vol. 100, no. 1, pp. 791–802, 2006.
[111] S. Iijima and T. Ichihashi, "Single-shell carbon nanotubes of 1-nm diameter," *Nature*, vol. 363, no. 6430, pp. 603–605, Jun. 1993.
[112] "Electronic Structure of Single-Wall Nanotubes," in *Physical Properties Of Carbon Nanotubes*, PUBLISHED BY IMPERIAL COLLEGE PRESS AND DISTRIBUTED BY WORLD SCIENTIFIC PUBLISHING CO., 1998, pp. 59–72.
[113] "Structure of a Single-Wall Carbon Nanotube," in *Physical Properties Of Carbon Nanotubes*, PUBLISHED BY IMPERIAL COLLEGE PRESS AND DISTRIBUTED BY WORLD SCIENTIFIC PUBLISHING CO., 1998, pp. 35–58.
[114] "Synthesis of Carbon Nanotubes," in *Physical Properties Of Carbon Nanotubes*, PUBLISHED BY IMPERIAL COLLEGE PRESS AND DISTRIBUTED BY WORLD SCIENTIFIC PUBLISHING CO., 1998, pp. 73–93.
[115] S. Bandow, S. Asaka, Y. Saito, A. M. Rao, L. Grigorian, E. Richter, and P. C. Eklund, "Effect of the Growth Temperature on the Diameter Distribution and Chirality of Single-Wall Carbon Nanotubes," *Phys. Rev. Lett.*, vol. 80, no. 17, pp. 3779–3782, Apr. 1998.
[116] S. M. Bachilo, M. S. Strano, C. Kittrell, R. H. Hauge, R. E. Smalley, and R. B. Weisman, "Structure-Assigned Optical Spectra of Single-Walled Carbon Nanotubes," *Science*, vol. 298, no. 5602, pp. 2361–2366, Dec. 2002.

[117] P. M. Ajayan, L. S. Schadler, and P. V. Braun, *Nanocomposite Science and Technology*. John Wiley & Sons, 2006.
[118] X. Li and J. Chang, "Preparation of bone-like apatite-collagen nanocomposites by a biomimetic process with phosphorylated collagen," *J Biomed Mater Res A*, vol. 85, no. 2, pp. 293–300, May 2008.
[119] H.-W. Kim, H.-J. Gu, and H.-H. Lee, "Microspheres of collagen-apatite nanocomposites with osteogenic potential for tissue engineering," *Tissue Eng.*, vol. 13, no. 5, pp. 965–973, May 2007.
[120] Z. Spitalsky, D. Tasis, K. Papagelis, and C. Galiotis, "Carbon nanotube–polymer composites: Chemistry, processing, mechanical and electrical properties," *Progress in Polymer Science*, vol. 35, no. 3, pp. 357–401, Mar. 2010.
[121] C. Wang, Z.-X. Guo, S. Fu, W. Wu, and D. Zhu, "Polymers containing fullerene or carbon nanotube structures," *Progress in Polymer Science*, vol. 29, no. 11, pp. 1079–1141, Nov. 2004.
[122] D. E. Hill, Y. Lin, A. M. Rao, L. F. Allard, and Y.-P. Sun, "Functionalization of Carbon Nanotubes with Polystyrene," *Macromolecules*, vol. 35, no. 25, pp. 9466–9471, Dec. 2002.
[123] J. Chen, M. A. Hamon, H. Hu, Y. Chen, A. M. Rao, P. C. Eklund, and R. C. Haddon, "Solution Properties of Single-Walled Carbon Nanotubes," *Science*, vol. 282, no. 5386, pp. 95–98, Oct. 1998.
[124] F. Pompeo and D. E. Resasco, "Water Solubilization of Single-Walled Carbon Nanotubes by Functionalization with Glucosamine," *Nano Lett.*, vol. 2, no. 4, pp. 369–373, Apr. 2002.
[125] M. Pinault, M. Mayne-L'Hermite, C. Reynaud, V. Pichot, P. Launois, and D. Ballutaud, "Growth of multiwalled carbon nanotubes during the initial stages of aerosol-assisted CCVD," *Carbon*, vol. 43, no. 14, pp. 2968–2976, Nov. 2005.
[126] L. M. Ericson, H. Fan, H. Peng, V. A. Davis, W. Zhou, J. Sulpizio, Y. Wang, R. Booker, J. Vavro, C. Guthy, A. N. G. Parra-Vasquez, M. J. Kim, S. Ramesh, R. K. Saini, C. Kittrell, G. Lavin, H. Schmidt, W. W. Adams, W. E. Billups, M. Pasquali, W.-F. Hwang, R. H. Hauge, J. E. Fischer, and R. E. Smalley, "Macroscopic, Neat, Single-Walled Carbon Nanotube Fibers," *Science*, vol. 305, no. 5689, pp. 1447–1450, Sep. 2004.
[127] R. Inai, M. Kotaki, and S. Ramakrishna, "Structure and properties of electrospun PLLA single nanofibres," *Nanotechnology*, vol. 16, no. 2, pp. 208–213, Feb. 2005.
[128] E. Burkarter, C. K. Saul, F. Thomazi, N. C. Cruz, L. S. Roman, and W. H. Schreiner, "Superhydrophobic electrosprayed PTFE," *Surface and Coatings Technology*, vol. 202, no. 1, pp. 194–198, Nov. 2007.
[129] J. Zhang, J. Li, and Y. Han, "Superhydrophobic PTFE Surfaces by Extension," *Macromolecular Rapid Communications*, vol. 25, no. 11, pp. 1105–1108, 2004.
[130] W. Hou and Q. Wang, "Stable polytetrafluoroethylene superhydrophobic surface with lotus-leaf structure," *Journal of Colloid and Interface Science*, vol. 333, no. 1, pp. 400–403, May 2009.

[131] M. A. Nilsson, R. J. Daniello, and J. P. Rothstein, "A novel and inexpensive technique for creating superhydrophobic surfaces using Teflon and sandpaper," *J. Phys. D: Appl. Phys.*, vol. 43, no. 4, p. 045301, Feb. 2010.
[132] E. L. Cussler, *Diffusion: Mass Transfer in Fluid Systems*. Cambridge University Press, 1997.
[133] M. H. Ali and M. Goretti Gomes, "A Simple and Efficient Heterogeneous Procedure for Thioacetalization of Aldehydes and Ketones," *Synthesis*, no. 8, pp. 1326–1332, 2005.